Electron transport in $SrTiO_3$ accumulation layers and semiconductor nanocrystal films

A THESIS
SUBMITTED TO THE FACULTY OF THE GRADUATE SCHOOL
OF THE UNIVERSITY OF MINNESOTA
BY

Han Fu

IN PARTIAL FULFILLMENT OF THE REQUIREMENTS
FOR THE DEGREE OF
Doctor of Philosophy

Boris Shklovskii

July, 2017

Acknowledgements

I have been so lucky to have Boris Shklovskii as my PhD advisor, to whom I owe a debt of gratitude. I have benefited a lot from his wisdom, patience and great kindness. Without his invaluable guidance in physics and strong support in life, my research work would not have been made possible. It is always great fun to discuss with and learn from him about physics.

I want to thank Brian Skinner, who has helped me start my research and taught me a lot ever since my very first work. He has given me so much precious advice on both physics and my career. I also want to thank Kostya Reich a lot, who has been a close collaborator and supportive friend throughout my PhD work. I have learned a lot from him about science. All the works explained in this thesis were done in collaboration with him.

Dedication

To my beloved family and all dear friends

Abstract

In this thesis, we study two subjects: $SrTiO_3$ (STO) accumulation layers and films made of semiconductor nanocrystals (NCs), which are important for technological applications. We start from the low temperature conductivity of electron accumulation layers induced by the very strong electric field at the surface of STO sample. Due to the strongly nonlinear lattice dielectric response, the three-dimensional density of electrons $n(z)$ in such a layer decays with the distance from the surface z very slowly as $n(z) \propto 1/z^{12/7}$. We show that when the mobility is limited by the surface scattering the contribution of such a tail to the conductivity diverges at large z because of growing time electrons need to reach the surface. We explore truncation of this divergence by the finite sample width, by the bulk scattering rate, by the back gate voltage, or by the crossover to the bulk linear dielectric response with the dielectric constant κ. As a result we arrive at the anomalously large mobility, which depends not only on the rate of the surface scattering, but also on the physics of truncation. Similar anomalous behavior is found for the Hall factor, the magnetoresistance, and the thermopower.

For the second part, we extend to the cases of spherical and cylindrical geometries, and more complicated planar structures. For the planar case, we study overlapping accumulation layers in $GdTiO_3$/STO/$GdTiO_3$ quantum wells and electron gases created by spill-out from NSTO (heavily n-type doped STO) layers into STO. Generalization of our approach to a spherical donor cluster creating a big Thomas-Fermi atom with electrons in STO brings us to the problem of supercharged nuclei. It is known that for an atom with nuclear charge Ze, where $Z > 170$, electrons collapse onto the nucleus resulting in a net charge $Z_n < Z$. Here, instead of relativistic physics, the collapse is caused by the nonlinear dielectric response. Electrons collapse into the charged spherical donor cluster with radius R when its total charge number Z exceeds the critical value $Z_c \simeq R/a$, where a is the lattice constant. The net charge eZ_n grows with Z until Z exceeds $Z^* \simeq (R/a)^{9/7}$. After this point, the charge number of the compact core Z_n remains $\simeq Z^*$, with the rest Z^* electrons forming a sparse Thomas-Fermi atom with it. We also study the case of long cylindrical clusters.

In the third part, we look at the details of the surface scattering by roughness of accumulation layers. To connect with previous works on surface roughness scattering, we focus on conventional semiconductors with the linear dielectric response where accumulation layers with very large concentrations of electrons and many subbands filled became recently available due to ionic liquid and other new methods of gating. The low temperature mobility in such layers is limited by the surface roughness scattering. However theories of roughness scattering so far dealt only with the small-density single subband two-dimensional (2D) electron gas. Here we develop a theory of roughness scattering limited mobility for the multisubband large concentration case. We show that with growing 2D electron concentration N the surface dimensionless conductivity $\sigma/(2e^2/h)$ first decreases as $\propto N^{-6/5}$ and then saturates as $\sim (\Lambda a_B/\Delta^2) \gg 1$, where Λ and Δ are the characteristic length and height of the surface roughness, a_B is the effective Bohr radius. This means that in spite of the shrinkage of the 2D electron gas width and the related increase of the scattering rate, the 2D electron gas remains a good metal. Thus, there is no re-entrant metal-insulator transition at high concentrations conjectured by Das Sarma and Hwang [PRB 89, 121413 (2014)]. The expression of surface relaxation time can be generalized to the STO case where the dielectric response is nonlinear. We find that there is no reentrant metal-insulator transition, either, in STO accumulation layers at experimentally available large N.

Finally, we switch to the study of NC films. We focus on the variable-range hopping of electrons in semiconductor NC films below the critical doping concentration n_c at which films become metallic. The hopping conductivity is then described by the Efros-Shklovskii law which depends on the localization length of electrons. We study how the localization length grows with the doping concentration n in the film of touching NCs. For that we calculate the electron transfer matrix element $t(n)$ between neighboring NCs for two models when NCs touch by small facets or just one point. We study two sources of disorder: variations of NC diameters and random Coulomb potentials originating from random numbers of donors in NCs. We use the ratio of $t(n)$ to the disorder-induced NC level dispersion to find the localization length of electrons due to the multi-step elastic co-tunneling process. We find three different phases at $n < n_c$ depending on the strength of disorder, the material, sizes of NCs and their facets: 1) "insulator" where the localization length of electrons increases monotonically with n and

2) “oscillating insulator” when the localization length (and the conductivity) oscillates with n from the insulator base and 3) “blinking metal” where the localization length periodically diverges. The first two phases were seen experimentally and we discuss how one can see the more exotic third one. In all three the localization length diverges at $n = n_c$. This allows us to find n_c.

Contents

List of Tables

List of Figures

Chapter 1

Introduction

1.1 Transport properties of $SrTiO_3$ accumulation layers

Recently, studies of ABO_3 perovskites have been a subject of interest due to their intriguing properties [1] and subsequent significant technological applications. Among them, $SrTiO_3$ (STO) has attracted special attention [2, 3]. STO is a semiconductor with a band gap of $\simeq 3.2$ eV and a large dielectric constant κ ranging from $2 \cdot 10^4$ at liquid helium temperatures to 350 at room temperature. It can be used as a building block for different types of devices, with reasonably large mobility [4, 5] and abundant exotic phenomena. For example, one can put STO together with other oxides like $GdTiO_3$ (GTO), $LaAlO_3$ (LAO), etc., to make heterostructures. These structures exhibit ferromagnetism, superconductivity, and multiferroics. The physics behind them, however, is not completely clear yet. For understanding of the complicated phenomena and future promising applications, it is important to first make clear of the basic electron transport properties of the system.

In such heterostructures, e.g., GTO/STO heterojunctions, an electron accumulation layer emerges spontaneously on the STO side (see the cyan region in Fig. 1.1) caused by the "polar catastrophe" (or "polar discontinuity") of GTO [6], inside which there are alternating positively and negatively charged layers creating an internal electric field and thus leading to surface excessive charges of a fixed two-dimensional (2D) concentration ($\sim 0.5\ e/a^2$ in the case of GTO where e is the electron charge, $a \approx 3.9\mathring{A}$ [7] is the lattice constant of STO). On the GTO/STO interface, the surface charges on the GTO side

are positive and induce the compensating electron gas inside STO. The role of GTO can also be played by LAO [4, 5, 2], $SmTiO_3$ (SmTO) [8]. $NdAlO_3$, $LaVO_3$ [9], $PrAlO_3$, $NdGaO_3$ [10], $LaGaO_3$ [11], $LaTiO_3$ [12] and others producing the polar catastrophe [6]. One can also accumulate up to 10^{14} cm^{-2} electrons on the surface of STO using ionic liquid gating [13, 14]. In all these devices, the electron gas inside STO is induced by an interfacial electric field resulting from positive charges on the other side of the interface. So it is natural to think that the depth profiles of the potential and electron density in STO have a universal origin in these cases.

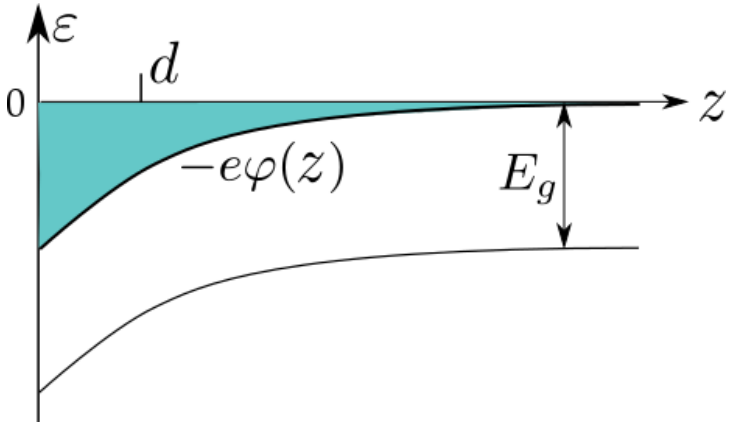

Figure 1.1: (Color online) Schematic electron potential energy $-e\varphi(z)$ diagram of an accumulation layer in a moderately n-doped STO where z is the distance from the interface. The band gap is E_g. Electrons (cyan region) are attracted by an external induction $\mathscr{D}_0$ applied at $z = 0$. The characteristic width of the electron gas is d. In the bulk of STO the Fermi level ε_F is near the bottom of the conduction band (denoted as the zero energy point).

Such depth profiles have already attracted attention from the experimental [15, 16, 17, 18] and theoretical points of view [19, 13, 20, 21, 22, 23]. For example, there are experimental data showing that electrons are distributed in a layer of width $\simeq 5 - 10$ nm near the $LaAlO_3/SrTiO_3$ interface, while theoretical works that attempt to explain such behavior are mostly based on microscopic numerical calculations. This thesis, however, adopts a simple, mostly phenomenological, analytic approach for describing the depth profiles. In this approach, the Landau-Ginzburg free energy expansion [24,

25] is used to account for the nonlinear dielectric response in STO, and electrons are almost everywhere described in the Thomas-Fermi approximation [26]. For an accumulation layer in STO created by an external interfacial induction $\mathscr{D}_0$, this gives a three-dimensional (3D) electron concentration $n(z)$ that depends on the distance from the surface z as

$$n(z) \propto (z+d)^{-12/7} \tag{1.1}$$

represented by the cyan region in Fig. 1.1, where the width d decreases with $\mathscr{D}_0$ as $d \propto \mathscr{D}_0^{-7/5}$. It is shown in the previous work [27] that these relations seem to agree reasonably well with experimental data [17, 16]. Although here it mostly concentrates on accumulation layers in STO, the developed approach is applicable to $KTaO_3$ [28] and $CaTiO_3$ [29] (which also have nonlinear dielectric response at considerable electric fields) serving as the host media for accumulation layers as well.

To obtain such results, we have made several reasonable assumptions. At the experimentally relevant 2D concentrations of donors $N > 10^{17}$ cm^{-3}, STO is moderately doped and the Fermi energy lies in the conduction band close to the bottom. Therefore, we can regard the Fermi level as at the conduction band bottom, defined as the zero point. Though STO changes symmetry from cubic to tetragonal at $T \simeq 110K$, the distortion is small [7] and can be neglected. The dielectric response is then approximately isotropic and its geometry is determined by the external field. So when an external induction $\mathscr{D}_0$ is directed along the z axis perpendicular to the interface which has a one-dimensional (1D) structure, the problem is effectively 1D and easy to deal with. Also, STO is assumed to have a single isotropic band with the effective mass $m^* \simeq 1.5\ m_e$, [27] where m_e is the free electron mass. This is justified by that in the Thomas-Fermi approximation, what matters is the density of states instead of the detailed band structure, which is well captured by the effective mass already. Based on these assumptions, the detailed derivations can be found in Sec. 2.1 of Chapter 2.

One should note that $n(z)$ here has an unusually long tail with a weak 12/7 power law decay due to the nonlinear dielectric response. As will be explained below, this tail is extremely mobile and thus called the "run-away tail" (RAT). Experimentally, it is found that the mobility of accumulation layers is much smaller than that of electrons in bulk STO, indicating clearly the dominance of surface scattering in the transport of accumulation layers. Therefore, in order to get relaxed, electrons at the distance

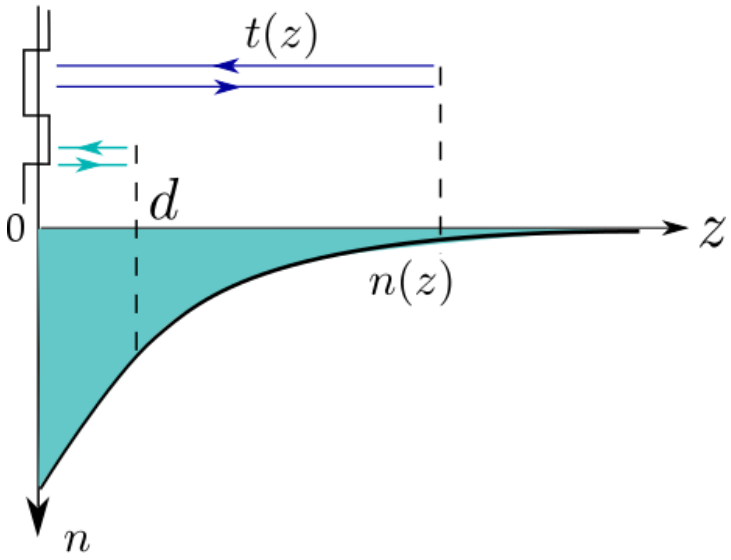

Figure 1.2: (Color online) Schematic plot of electron relaxation by surface roughness scattering. The ups and downs on the surface (at $z = 0$) represent the roughness. The electron gas (cyan region) has a 3D density depth profile $n(z) \propto z^{-12/7}$ where z is the distance from the surface. Electrons in the tail have a much larger travel time $t(z)$ to the surface and thus a much larger relaxation time $\tau(z)$ than electrons in the main body of the distribution located within the distance d from the surface. At large distances, the relaxation time grows with z as $\tau(z) \propto z^{11/7}$.

z need to first reach the surface and then get scattered. Their relaxation time $\tau(z)$ is mainly determined by the travel time $t(z) \sim z/v(z) \propto z/[n(z)]^{1/3}$. In the tail, $n(z) \propto z^{-12/7}$ therefore gives the relaxation time $\tau(z) \propto z^{11/7}$. The scattering rate of tail electrons is much smaller than that of electrons in the main body of the distribution $n(z)$ (within the distance d from the surface), which are closer to and thus more frequently scattered by the surface (see Fig. 1.2). This extremely mobile long tail results in the anomalously large mobility, Hall factor, magnetoresistance, and thermopower. These kinetic coefficients, because of the truncation of the tail at some distance by certain mechanisms, get large but still finite values in the end. For example, when the STO sample is relatively thin such that the tail is cut by the finite width $W \gg d$ of STO, the thermopower S grows with the truncation length W as $S \propto W^{8/7}$, which goes to infinity if W is infinite (corresponding to no truncation). This prediction agrees nicely

with experimental data [8] as shown in Fig. 1.3. Similar anomalies were also predicted for silicon MOSFETs but at high temperatures [30]. It should be pointed out that the interplay here between contributions from tail and body electrons to kinetic coefficients can also be interpreted as the existence of effectively two types of carriers. This option has been widely investigated for the data on the linear and nonlinear Hall effect [31], on the inconsistency between electron concentrations measured by the Hall effect and the Shubnikov-de Haas effect [32], and on the difference between ac and dc transport results [33]. More detailed discussion of the RAT-caused anomalous transport properties is included in Sec. 2.2 of Chapter 2.

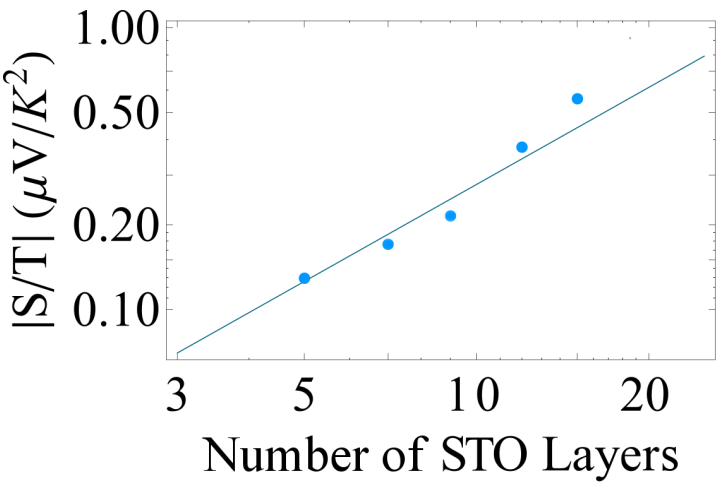

Figure 1.3: Comparison of experimental data and RAT prediction for the absolute value of the thermopower S divided by the temperature T as a function of the STO sample width in the GTO/STO/GTO quantum wells represented by the number of STO layers. The solid circles represent the experimental data taken from Reference [8] (from which we take only the peak values of $|S/T|$ in the measured range of T for relatively wide samples where the width W truncating the tail is large enough compared to d so that two accumulation layers formed near each GTO/STO interface weakly overlap and can be regarded independent). The solid line denotes the fitting of the data with the scaling behavior $S/T \propto W^{8/7}$.

1.2 Electron gas in more complicated STO-based structures and geometries

On top of the simple solution for a single accumulation layer one can study more complicated problems based on STO where there are two accumulation layers overlapping, e.g., in GTO/STO/GTO multi-heterojunctions [34, 35, 36] as shown in Fig. 1.4. When the STO layer is thick, one can expect that the two accumulation layers overlap weakly by the vanishing tails and the final electron distribution can be described as an approximate addition of two accumulation layers given by Eq. (1.1). However, as the STO layer gets thinner, the overlap becomes stronger. Due to the nonlinear physics here, the electron density profile changes substantially. In Sec. 3.1 of Chapter 3, how electron density profiles evolve as a function of the the distance W between two heterointerfaces is calculated.

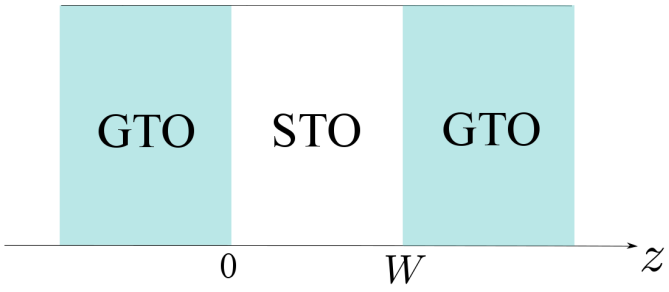

Figure 1.4: The GTO/STO/GTO quantum well with wide enough GTO layers and an STO layer of width W. Here, one GTO/STO interface is defined as $z = 0$ while the other is $z = W$. The GTO layers generate $\mathscr{D}_0 = 2\pi e/a^2$ on each interface.

Unlike the case for a single accumulation layer in a relatively thick STO sample, there is no longer a simple analytic solution for the GTO/STO/GTO structure due to the absence of a simple boundary condition. A numerical method is given. The idea is that for given boundary conditions (which numerically give the whole electron density profile inside STO), one can get the corresponding W from integrating the differential equation. As a result, one actually obtains W as a function of different $n(z)$ shapes. Inversely, one then gets the density profiles at different W as illustrated in Fig. 1.5. It can be seen that

an almost constant $n(z)$ at $W = 4a$, around which the quantum criticality is observed [36], evolves to the one reminiscent of two weakly overlapping tails of accumulation layers described by Eq. (1.1) at $W = 16a$, as expected. Besides in the case of overlapping accumulation layers, the planar problem can also become complicated even with a single accumulation layer when it is created in a modulation-doped structure of NSTO/STO [37, 38, 39, 40, 41]. In this case electrons spill out from the heavily n-type doped STO layer (NSTO) and the interfacial induction $\mathscr{D}_0$ is self-consistently provided by the depletion layer in NSTO instead of having a fixed value like in GTO/STO interfaces. The accumulation layer in STO has the same structure as in Eq. (1.1) with the thickness d now dependent on the doping concentration in NSTO. Based on all this knowledge, NSTO/STO multi-heterojunctions and the case of a heterointerface combining both the polar discontinuity and the electron spill-out are also discussed in Chapter 3.

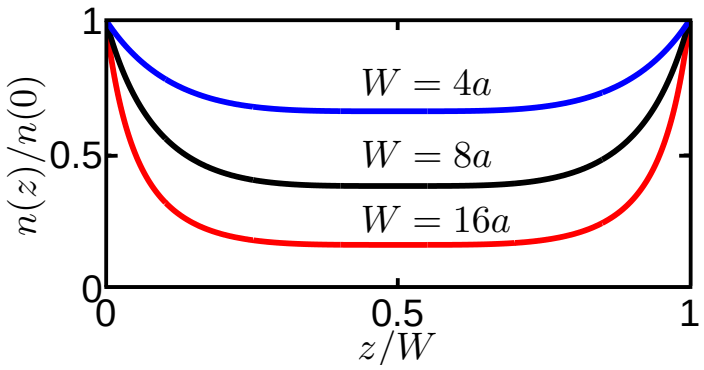

Figure 1.5: (Color online) Electron distribution in STO of GTO/STO/GTO quantum wells at different values of W which is the width of the STO layer (a is the lattice constant). The thick solid lines are the electron concentration $n(z)$ in the unit of $n(0)$ where $n(0)$ is the electron concentration at $z = 0$ (red: $W = 16a$; black: $W = 8a$; blue: $W = 4a$). Here, one GTO/STO interface is defined as $z = 0$ while the other is $z = W$. When W is not very large, the electron density profile is substantially different from the simple addition of two single accumulation layers.

Sometimes, the electron gas in STO is created by external charges with a spherical or cylindrical symmetry. The system thus has a 3D or 2D geometry, making it difficult to study. For example, one can dope the bulk STO by generating oxygen vacancies at high temperatures. The vacancies either assemble together to lower the system's energy

[42, 43] or form along a network of extended defects [44], producing large positively charged spherical or cylindrical donor clusters. Another way to more controllably create such a cluster is to "draw" a disc or line of charge by the atomic force microscope (AFM) tip on the surface of LAO/STO structure with the subcritical thickness for LAO [45, 46]. The potential in STO caused by such a positive disc or line is similar to that of a charged sphere or cylinder completely inside the bulk STO.

Let us now consider a spherical donor cluster with radius R and charge Ze. At relatively small Z, there are Z electrons located at distances from a_B/Z to a_B from it, which form a Thomas-Fermi "atom" [47] with the cluster. Here $a_B = \kappa\hbar^2/m^*e^2$ is the Bohr radius and $\hbar$ is the Planck constant. Since κ is large, the electrons are far away from the cluster and the whole "atom" is very big. As Z increases, the electron gas swells inward to hold more electrons. However, as shown in Sec. 3.2, we find that when Z goes beyond a certain value Z_c (a_B/Z is still much larger than R at this moment), the physical picture is qualitatively altered. Surrounding electrons start to collapse into the cluster renormalizing the net cluster charge from Ze to Z_ne and at very large Z one gets $Z_n \ll Z$. This is again a result of the nonlinear dielectric response which is induced near the cluster.

The phenomenon of charge renormalization is not new [48, 49]. For a highly charged atomic nucleus with charge Ze, the vacuum is predicted to be unstable against creation of electron-positron pairs, resulting in a collapse of electrons onto the nucleus with positrons emitted [48]. This instability happens when $Z > Z_c$ with $Z_c \simeq 170 \gtrsim 1/\alpha$, where $\alpha = e^2/\hbar c \simeq 1/137$ is the fine structure constant and c is the light speed. When Z exceeds $Z^* \simeq 1/\alpha^{3/2} \simeq 137^{3/2}$, the net charge saturates at Z^* as in previous work [49]. In the condensed matter setting, there are similar phenomena in narrow-band gap semiconductors and Weyl semimetals [49] as well as graphene [50]. In all these cases, the collapse happens because the energy dispersion of electrons is relativistic in the strong Coulomb field of a compact donor cluster playing the role of a nucleus. In our case, however, the collapse originates from the strong nonlinearity of the dielectric response in STO at small distances from the cluster. In the case of a spherical donor cluster, this nonlinearity leads to the change of the attractive potential near the cluster from being $\propto 1/r$ to $\propto 1/r^5$, resulting in the collapse of non-relativistic electrons to the cluster. The first electron collapses at $Z \simeq Z_c \simeq R/a$, and at $Z \gg Z^* \simeq (R/a)^{9/7}$, the net

charge of nucleus $Z_n e$ saturates as $Z_n \simeq Z^*$, as shown in Fig. 1.6.

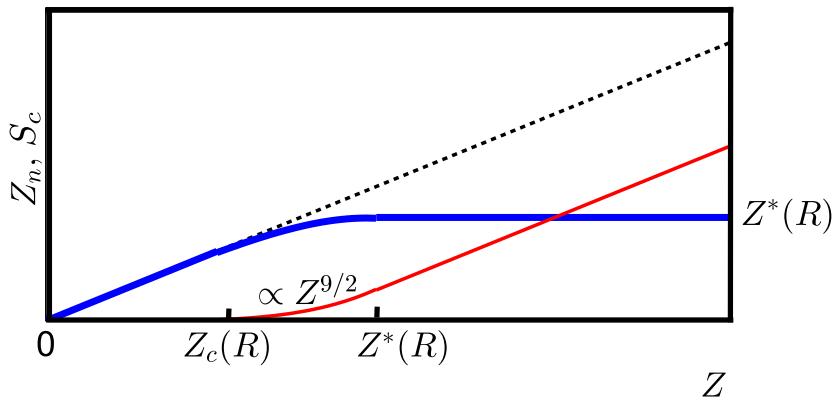

Figure 1.6: (Color online) The number of collapsed electrons S_c and the renormalized net charge $Z_n e$ as a function of the original charge Ze for spherical donor clusters in STO. S_c is shown by the thin solid line (red), Z_n is denoted by the thick solid line (blue), and the dashed line (black) is a guide-to-eye where $Z_n = Z$. Z_c denotes the critical value where electrons begin to collapse and Z^* is the saturation point where Z_n stops growing. Both Z_c and Z^* depend on the cluster radius R. $S_c \propto Z^{9/2}$ at $Z_c \ll Z \ll Z^*$.

For the donor clusters shaped like long cylinders, we describe them by the linear charge density ηe while their radius is still denoted as R. It is also shown in Sec. 3.2 of Chapter 3 that when the charge density ηe is larger than certain value $\eta_c e$, electrons begin to collapse into the cluster and the charge density is weakly renormalized. When η exceeds another value $\eta^* \gg \eta_c$, the renormalization becomes so strong that the net density η_n remains $\simeq \eta^*$ regardless of the original density η. This problem is similar to that of the charged vacuum condensate near superconducting cosmic strings [51], and is also reminiscent of the Onsager-Manning condensation [52] in salty water. (For example, in salty water, the negative linear charge density of DNA is renormalized from $\simeq -4e/l_B$ to the universal net value $-e/l_B$ due to the condensation of Na^+ ions onto the DNA surface. Here $l_B = e^2/\kappa_w k_B T \simeq 7\,\mathring{A}$ where $\kappa_w = 81$ is the dielectric constant of water, k_B is the Boltzmann constant, and T is the room temperature.)

1.3 Surface roughness scattering

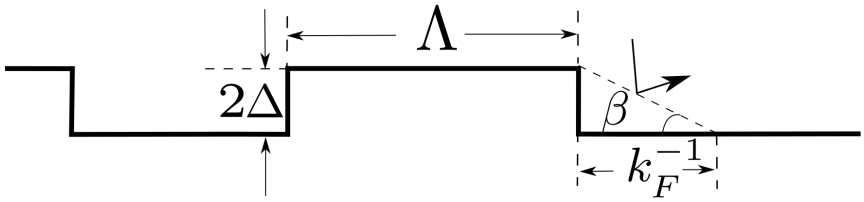

Figure 1.7: The exponential model of surface roughness. The size of the roughness is Λ and the height fluctuates as $\pm\Delta$ with respect to the average interface where $2\Delta \approx a$ and a is the semiconductor lattice constant. At very large concentrations, $\Delta \ll k_F^{-1} \ll \Lambda$, the incident electron hits only a single island. For the exponential model of roughness, the electron is scattered only by the island edge which effectively has a height $\sim \Delta$, a length $\sim k_F^{-1}$, and thus a slope angle $\beta \simeq \Delta k_F$.

As explained in Sec. 1.1 of Introduction, one prerequisite of RAT formation is the surface scattering dominance in the accumulation layer. However, we have not yet talked about the detailed mechanism of the surface scattering, which gives the surface relaxation time τ_s or the scaling prefactor of the relaxation time $\tau(z) \propto (z/d)^{11/7}$. One of the most important surface scattering mechanisms is by the roughness, which for relatively clean surfaces can be imagined as a collection of random atomic-size steps up or down of height $\Delta \sim a$ (a generally refers to the lattice constant of the semiconductor in discussion) and characteristic size $\Lambda \gg \Delta$ along the surface (see Fig. 1.7). This can be quantitatively described by the exponential model of roughness, which is experimentally confirmed [53]. The surface roughness scattering is actually well studied by previous works in conventional semiconductors with a linear dielectric response for inversion layers where the electron gas is 2D [54, 30, 55, 56, 57, 58]. The mobility μ limited by the surface roughness scattering behaves as $\mu \propto 1/\mathscr{E}^2$ where $\mathscr{E}$ is the surface electric field. For a large enough $\mathscr{E}$ the 2D concentration of electrons $N \propto \mathscr{E}$ so that $\mu \propto 1/N^2$ and the surface conductivity $\sigma = Ne\mu \propto 1/N$. This result holds for an inversion layer in a lightly doped p-type semiconductor when $\mathscr{E}$ is much larger than the electric field

of the depletion layer. The low temperature mobility was also extensively studied in quantum wells, where it is limited by the surface roughness of both interfaces. This mobility strongly depends on the width of the quantum well [59, 60, 61]. In all these works, because of the interest in higher mobilities, the surface roughness scattering was studied theoretically only for relatively small concentrations N, when only the first energy quantization subband is filled at low temperatures [30, 55, 56, 57, 58, 59, 60, 61]. Also, it was difficult to induce large electron concentrations N (higher than 10^{13} cm^{-2} in Si). So the roughness scattering at large N when many subbands are filled at low temperatures remains unexplored, either for conventional semiconductors with a linear dielectric response or for STO where the dielectric response is nonlinear.

The last decade, however, witnessed growing interest in accumulation layers with large 2D concentrations N which allow to achieve qualitatively new properties of the electron gas, such as superconductivity or magnetism. New methods to create large electron concentrations were developed including gating with help of an electrolyte or a room temperature ionic liquid, which does not need an insulator layer and, therefore, makes a double layer with a very large capacitance. We have introduced in Sec. 1.1 that accumulation layers in STO can be induced in this way. In fact, this method is also very useful for conventional semiconductors. For example, in Si, $N \sim 5 \cdot 10^{13}$ cm^{-2} were achieved using gating by an electrolyte [62] and by an ionic liquid [63]. Even larger concentrations $N \sim 10^{14}$ cm^{-2} were induced in ZnO [64] and MoS_2 [65]. Another important method is based on heterojunctions of polar and nonpolar semiconductors such as in GaN-based heterojunctions where concentrations up to 4.4×10^{13} cm^{-2} were achieved in the conventional semiconductors [66, 67, 68], similarly to GTO/STO heterostructures explained in Sec. 1.1. In order to fill many electron subbands, the concentration N should satisfy that the dimensionless parameter $Na_B^2 > 1$, where a_B is the Bohr radius of the host semiconductor. In the cases of ZnO and MoS_2 mentioned above Na_B^2 reaches 5. In semiconductors with relatively large a_B such as GaAs, InAs, InSb, and PbTe, it should be easy to reach $Na_B^2 \gg 1$. For such multisubband cases, as said above, the roughness scattering limited mobility has not been theoretically studied. In Chapter 4, this gap is filled and to make close connections with previous works, conventional semiconductors are investigated first with STO accumulation layers studied later.

For conventional semiconductors with linear dielectric response, the surface relaxation time τ_s is found for relatively small and large N, respectively. Since the tail electron concentration decays with the distance very fast as $n(z) \propto z^{-6}$ in this case [69], the kinetic coefficients converge to the surface values. The total conductivity is then completely determined by τ_s. The result for the dimensionless conductivity $\sigma(N)/(2e^2/h)$ at $\Lambda < a_B$ is shown on Fig. 1.8 as a function of the dimensionless concentration Na_B^2 for the exponential model of roughness by the thick solid line (black). The conductivity first decreases with N as $\propto N^{-6/5}$ and then saturates at the level

$$\frac{\sigma}{2e^2/h} \simeq \frac{\Lambda a_B}{\Delta^2}, \tag{1.2}$$

which is much larger than unity assuming that both $\Lambda \gg \Delta$ and $a_B \gg \Delta$. The thin solid line (red) schematically shows the $1/N$ dependence of the conductivity derived for a single subband by previous work [55].

Here, the saturation happens at the point when the electron wavelength k_F^{-1} at the surface is approximately equal to the size Λ of the roughness. Before this point or at smaller N, the roughness felt by electrons is averaged over all irregularities within the region of size $\sim k_F^{-1}$. As the concentration increases, k_F increases and fewer irregularities are averaged over making the surface "rougher" for electrons. When k_F^{-1} gets below Λ, the electron "hits" only a single irregularity and the level of "roughness" is fixed. For the electron density profile in the linear dielectric response case, this leads to the final constant conductivity. Our results here contradict to the conjecture [70] that the single subband result [55] can be extrapolated to the large-concentration multisubband case (see the thin dashed line (red) in Fig. 1.8). This conjecture led to the dramatic prediction [70] that the dimensionless conductivity could become smaller than unity implying the reentrant metal-insulator transition with growing N. The results here show that at large N the accumulation layer remains metallic. This agrees with decent mobilities observed experimentally [71, 64, 65, 62].

In the STO case, we get the same expression of τ_s in terms of the surface electron wavenumber k_F and the electron gas width d. Now using the new relationship between d, k_F, and N for the nonlinear dielectric response, the mobility of surface electrons $\mu_s = e\tau_s/m^*$ at very large N is

$$\mu_s \propto \frac{e}{h}\frac{1}{N}\frac{1}{(Na^2)^2} \tag{1.3}$$

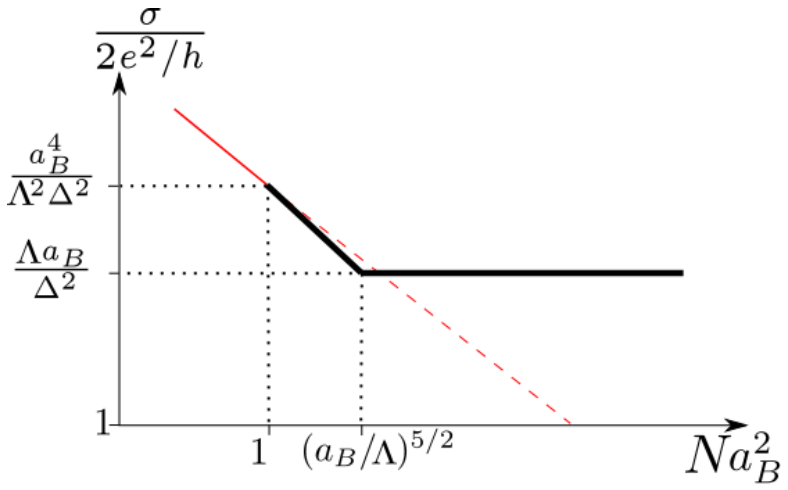

Figure 1.8: (Color online) Schematic log-log plot of the dimensionless total conductivity of an accumulation layer $\sigma/(2e^2/h)$ limited by the surface roughness scattering as a function of the dimensionless 2D electron concentration Na_B^2 at $\Lambda < a_B$ in conventional semiconductors with the linear dielectric response. The thick solid line (black) shows the conductivity for the multisubband accumulation layer. It first decreases as $\left(Na_B^2\right)^{-6/5}\left(a_B^4/\Lambda^2\Delta^2\right)$ approximately continuing the single subband dependence $1/N$ and then saturates at $Na_B^2 \sim (a_B/\Lambda)^{5/2}$, where the wavelength $k_F^{-1} \sim \Lambda$. The thin solid line (red) represents the $1/N$ dependence derived for a single subband [55]. Conjectured extrapolation [70] of this dependence to larger concentrations is shown by the thin dashed line (red).

with a prefactor much larger than unity. Due to the existence of RAT, the final mobility averaged over all electrons is much larger than the surface mobility μ_s and the total conductivity $\sigma \gg Ne\mu_s \gg (e^2/h)\left(Na^2\right)^{-2}$. For experimentally available concentrations N, $Na^2 < 1$, so the final conductivity is much larger than the critical value e^2/h per spin (which means $2e^2/h$ considering the two-fold spin degeneracy). The system therefore remains metallic for all experimentally available large 2D electron concentrations N and there is no reentrant metal-insulator transition in the STO accumulation layers, either.

1.4 Electrical conduction in films made of semiconductor nanocrystals

Besides STO, there are also other materials being intensively investigated due to their great potential for applications. Among them, films made of semiconductor nanocrystals (NCs) play a very important role for building optoelectronics such as solar cells [72], light emitting diodes [73] and field effect transistors [74, 75], because of their size-tunable optical and electrical properties [76], and low-cost solution-based processing techniques [77, 78]. These applications require conducting NC films and several ways of introducing carriers via doping are being explored [79, 80, 81, 82, 83, 84, 85, 74, 86]. At a given concentration of carriers the mobility can be improved by moving NCs closer to each other and reducing their contact resistance.

In many studies [79, 80, 86, 82] the low temperature conductivity of doped films was found to obey the Efros-Shklovskii (ES) variable range hopping law [87]:

$$\sigma(T) = \sigma_0 \exp\left[-\left(\frac{T_{ES}}{T}\right)^{1/2}\right]. \tag{1.4}$$

Here σ_0 is a conductivity prefactor, T is the temperature, and

$$T_{ES} = \frac{Ce^2}{\varepsilon_f k_B \xi} \tag{1.5}$$

in Gaussian units, where ξ is the electron localization length, ε_f is the effective dielectric constant of the film, e is the electron charge, k_B is the Boltzmann constant, $C \simeq 9.6$ [88]. Typically, ξ grows with the 3D concentration of electrons n in a NC and with the improvement of contacts between NCs, and consequently, T_{ES} becomes smaller and the film becomes more conducting [86].

In Chapter 5 we concentrate on doping of NC films by chemical donors or acceptors [89] which was recently achieved in InAs [83], CdSe [84], HgS [85] and Si [86] NCs. While many experimental studies have been directed towards increasing the conductivity of NC films with increased n, it was not clear when ξ diverges and T_{ES} vanishes so that the NC film becomes metallic [90, 91, 92]. In other words, it was unknown what is the critical concentration n_c of electrons (or holes) in a NC necessary for the insulator-metal transition (IMT). Recently [86] n_c was estimated for the case favorable for the IMT ,

where close-to-spherical NCs with diameter d touch each other by small facets of radius $\rho \ll d$ without any ligands that impede the conduction by creating a barrier between NCs (see Fig. 1.9a). The result is very simple

$$n_c \simeq 0.3\rho^{-3}. \tag{1.6}$$

The IMT is illustrated in Fig. 1.9 where we show how an electron wave packet of the minimum available size for a given n quasiclassically passes between two touching NCs at $n > n_c$, but has to tunnel at $n < n_c$ and, therefore, becomes more vulnerable to disorder. (One should note that in the NC part of this thesis, we assign new meanings to some of the symbols used in previous discussion due to the limited number of appropriate symbols to use. For example, d is the NC diameter now. Also, we will introduce later the number of doped electrons in each NC N, the energy quantization gap between consecutive energy shells in NCs Δ, the decay length of electron wavefunctions b inside the medium between NCs which is thus the characteristic tunneling distance of electrons between NCs, α which is the energy shift ratio to the energy quantization gap Δ for each level, ε which is the dielectric constant of the semiconductor constituting the NC here, etc.)

Contacts between NCs may have different origins. For example, a close-to-spherical NC has small facets due to the discreteness of the crystal lattice. Their radius can be estimated as $\rho_a \simeq \sqrt{da/2}$, where a is the lattice constant. For CdSe NCs with $a = 0.6$ nm and $d = 5$ nm, $\rho_a \sim 1.2$ nm and Eq. (1.6) gives $n_c = 2 \times 10^{20}\,\mathrm{cm}^{-3}$. For the case in which NCs shown in Fig. 1.9 touch each other away from these facets, a finite tunneling distance $b \sim 0.1$ nm in the medium between NCs should be taken into account. This leads to $\rho = \rho_b \simeq \sqrt{db/2} \ll \rho_a$ which is the radius of an effective "b-contact" and the critical concentration n_c is much larger. For epitaxially connected NCs, the removal of ligands induces oriented attachment between NCs through facets whose radius can be as large as $d/4$ [93, 94, 95, 96].

On the other hand, at very light doping when the average number of electrons per NC, $N = \pi n d^3/6$, is less than unity one should see the nearest-neighbor hopping between NCs with the activation energy equal to the charging energy of a NC [88, 97]. Thus, the ES hopping should be observed in a large range of the concentrations $6/\pi d^3 < n < n_c$. To calculate T_{ES} given by Eq. (1.5), we need to know how the localization length

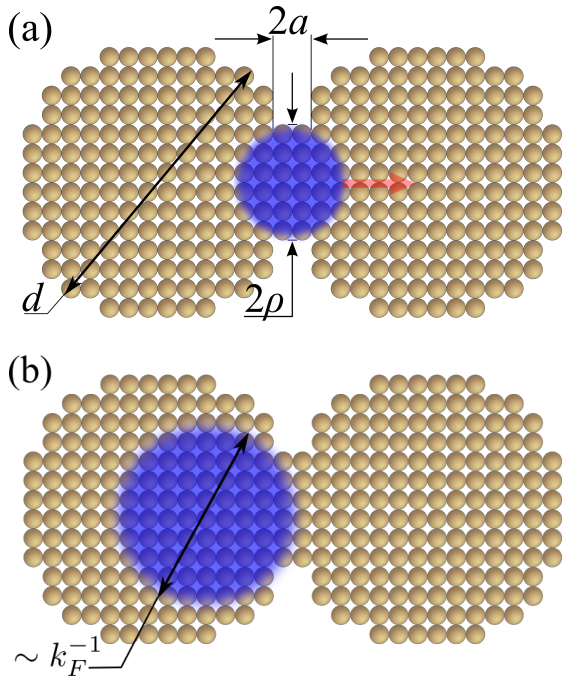

Figure 1.9: (Color online) The cross-section of two NCs in contact by their facets with radius $\rho \ll d$ each. Here a is the lattice constant, d is the NC diameter. The blue cloud depicts the smallest available electron wave packet with the size $k_F^{-1} \sim n^{-1/3}$, where k_F is the Fermi wavenumber and n is the 3D doping concentration of electrons in each NC. (a) Electron transport at $n > n_c$. The smallest electron packet fits in the touching facets and moves through the contact. (b) At $n < n_c$, the smallest wave packet gets stuck near the contact and the electron tunneling between NCs is depleted so much that it cannot overcome the disorder to delocalize electrons.

$\xi(n)$ grows in this range, before reaching the NC diameter d and diverging in a critical vicinity of n_c.

The localization length of electrons is determined by the competition of the energy variation δE induced by disorder and the tunneling matrix element t between neighboring NCs (see Fig. 1.10 where δE saturates at Δ). We study two main sources of disorder: the dispersion of NC diameters, which changes the quantization kinetic energy, and the variation of the number of donors in a NC, which leads to charging of NCs and random Coulomb potentials shifting electron levels. We also calculate $t(n, \rho)$ for the two models of small-ρ contacts mentioned above. We arrive at the conclusion that typically the

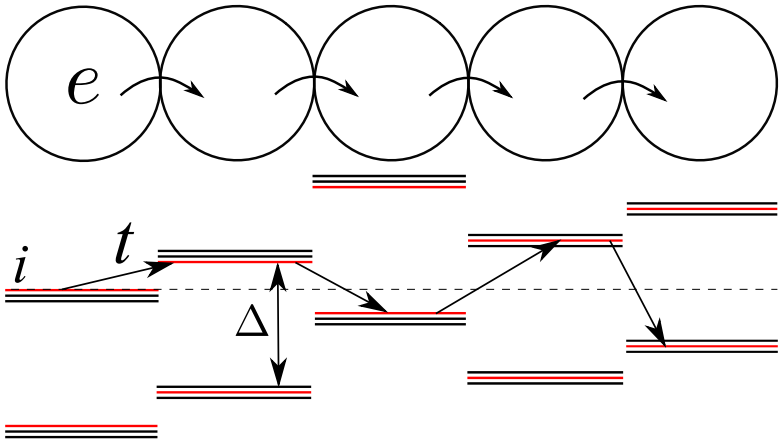

Figure 1.10: Electron hopping via the elastic multi-step co-tunneling through the chain of touching spherical NCs at small N with the electron energy in the vicinity of the Fermi level. The weakly split degenerate electron energy shells are shifted up or down by the disorder potential γ and the energy variation of the shells closest to the Fermi level between neighboring NCs δ_E saturates at the energy quantization gap Δ when the disorder potential is very large. The electron (denoted by the letter 'e') tunnels with the tunneling matrix element t from the initial NC i through the $m = 0$ levels (red) in the shells closest to the Fermi level in each intermediate NC. Virtually visited NCs (and their levels) are shown by arrows. The dashed line represents the Fermi level.

combination of both sources of disorder is so strong that one needs $N \gg 1$ electrons per NC to make large enough t in order to get appreciable ξ and approach the IMT.

In Chapter 5, the generic case for small semiconductor NCs is dealt with when electron energy shells of the spherical NCs are separated by the quantization gap Δ and each degenerate shell is weakly split. It is shown that when the disorder potential γ exceeds Δ so that the energy variation δE saturates at Δ, for NCs touching by contact facets of small radius ρ, the localization length ξ is

$$\xi(n) \approx \frac{d}{\ln(2/n\rho^3)}. \tag{1.7}$$

This result is obtained at low temperatures when electrons hop via the elastic multi-step co-tunneling process between distant NCs (see Fig. 1.10). The effective dielectric constant ε_f is not affected by the electron polarization in NCs far from the IMT point. Thus, Eq. (1.7) together with Eq. (1.5) can be used to predict the dependence $T_{ES}(n)$.

The localization length ξ becomes comparable to d when n gets close to the critical concentration n_c of the IMT. Using this criterion, we arrive from the insulating side at the estimate Eq. (1.6) which was obtained [86] from the metallic state before.

Both Eqs. (1.7) and (1.6) do not depend explicitly on the disorder strength. This happens because when the disorder potential γ exceeds the energy quantization gap Δ, due to the periodicity of the quantized spectrum, the energy difference between neighboring NCs δE saturates at the level of Δ and the electron density of states summed over the entire film is approximately uniform. Remarkably both Eqs. (1.7) and (1.6) continue to play an important role even when γ is smaller than Δ and well defined peaks of the electron density of states appear. With decreasing width of these peaks the localization length starts to oscillate at small N while keeping its minima close to the base line Eq. (1.7). At the critical concentration given by Eq. (1.6), the oscillation disappears with the localization length ξ going to infinity as the system enters the usual metallic state. Phase diagrams are used in Chapter 5 to address the different situations in several widely used semiconductor NCs, i.e., CdSe, InAs and ZnO, with $d = 5$ nm, $\rho = \rho_a = 1.2$ nm and 7% dispersion of NC diameters, where the systems fall into different regions of the parameter space and exhibit various conduction behaviors.

Chapter 2

Surface scattering limited transport of STO accumulation layers

2.1 Electron potential and density depth profiles of a single accumulation layer in STO

Bulk STO typically is an n-type semiconductor with a 3D concentration of donors $n_D > 10^{17}$ cm^{-3}. Let us discuss the position of the Fermi energy ε_F in such crystals. The electron spectrum near the bottom of the conduction band is complicated [98], and in order to make the problem of an accumulation layer tractable analytically we assume that it is isotropic and non-degenerate with the effective mass $m^* \simeq 1.5\ m_e$, [27] where m_e is free electron mass. Within the hydrogenic theory of shallow donors, the donor Bohr radius a_B is equal to $\kappa \cdot b$, where $b = \hbar^2/m^* e^2 \simeq 0.35$ Å, e is the electron charge, and κ is dielectric constant of the material. At room temperature when $\kappa = 350$, the Bohr radius $a_B = 123$ Å is so large that the Mott criterion for the metal-insulator transition in doped semiconductors $n_c a_B^3 = 0.02$ leads to a very small critical concentration of doped carriers $n_c = 1 \cdot 10^{16}$ cm^{-3}. At helium temperatures $\kappa = 2 \cdot 10^4$ and $n_c = 6 \cdot 10^{10}$ cm^{-3}. Thus, at the experimentally relevant concentration of donors $n_D > 10^{17}$ cm^{-3}, we are dealing with a moderately doped semiconductor

in which the Fermi energy lies in the conduction band of STO. On the other hand, due to the relatively high effective mass the bulk Fermi energy ε_F is smaller than the bending energy of the conduction band bottom near the interface. For example, for $n = 10^{18}\,\mathrm{cm}^{-3}$ where n is the 3D concentration of doped electrons, the low temperature Fermi energy calculated from the bottom of the conduction band is $\varepsilon_F \simeq 4$ meV, which can be up to 100 times smaller than the bending energy of the conduction band bottom in an accumulation layer for GTO/STO. Therefore, one can assume that the Fermi level coincides with the bottom of the conduction band (denoted as the zero energy point as shown in Fig. 1.1).

We are interested in the electron distribution near an interface of STO. We consider the case when the axis z is directed perpendicular to the interface (plane $z = 0$) and lies along the [100] axis of a cubic crystal of STO. As said in Introduction, in fact, STO changes symmetry from cubic to tetragonal at $T \simeq 110K$, but the distortion is small [7] and is neglected. An external induction $\mathscr{D}_0$ applied from the left is directed along the z axis making the problem effectively 1D. Following Ref. [27], we derive the electron potential and density depth profiles below.

If the 3D electron density is denoted by $n(z)$, then the potential depth profile $\varphi(z)$ in the system is determined by the equations:

$$\frac{d\mathscr{D}}{dz} = -4\pi e n(z),\ \mathscr{D} = \mathscr{E} + 4\pi\mathscr{P},\ \frac{d\varphi}{dz} = -\mathscr{E}, \tag{2.1}$$

where $\mathscr{D}(z)$, $\mathscr{E}(z)$, $\mathscr{P}(z)$ are the electric displacement field (the induction field), the electric field and the electric polarization in STO. Equations (2.1) should be solved with proper boundary conditions. For example, for a single accumulation layer the boundary conditions are $\mathscr{D}(0) = \mathscr{D}_0$ and $\varphi(\infty) = 0$.

STO is well known as a quantum paraelectric, where the onset of ferroelectric order is suppressed by quantum fluctuations [99]. For a continuous second-order phase transition the Landau-Ginzburg theory gives the free energy density $\mathscr{F}$ as a power series expansion with respect to the polarization $\mathscr{P}$:

$$\mathscr{F} = \mathscr{F}_0 + \frac{\tau}{2}\mathscr{P}^2 + \frac{1}{4}A\frac{1}{\mathscr{P}_0^2}\mathscr{P}^4 - \mathscr{E}\,\mathscr{P}, \tag{2.2}$$

where $\mathscr{F}_0$ stands for the free energy density at $\mathscr{P} = 0$ and τ is the inverse susceptibility $\tau = 4\pi/(\kappa - 1) \simeq 4\pi/\kappa$. In this work $0 < \tau \ll 1$, $\mathscr{P}_0 = e/a^2$ is the characteristic

polarization and $a \simeq 3.9$ Å [7] is the lattice constant. The coefficient A describes the nonlinear dielectric response. For all estimates below we use $A = 0.8$ following from Ref. [27]. The last term of Eq. (2.2) is responsible for the interaction between the polarization and the electric field $\mathscr{E}$. In general $\mathscr{F}$ depends on the components of the vector $\mathscr{P}$, but in the chosen geometry the problem is 1D, and all vectors are directed along the z axis. The crystal polarization $\mathscr{P}$ is determined by minimizing the free energy density $\mathscr{F}$ in the presence of the electric field $\mathscr{E}$, $\delta\mathscr{F}/\delta\mathscr{P} = 0$. This condition relates $\mathscr{E}$ and $\mathscr{P}$,

$$\mathscr{E} = \frac{4\pi}{\kappa}\mathscr{P} + \frac{A}{\mathscr{P}_0^2}\mathscr{P}^3. \tag{2.3}$$

Since κ at low temperature is so large, one can ignore the first term. We note that $\mathscr{E} \ll 4\pi\mathscr{P}$ as $\mathscr{P} \ll \mathscr{P}_0$ typically, so $\mathscr{D} \approx 4\pi\mathscr{P}$ and thus

$$\mathscr{E} \approx \frac{A}{(4\pi)^3\mathscr{P}_0^2}\mathscr{D}^3. \tag{2.4}$$

In the Thomas-Fermi approach [26, 47], the 3D electron concentration $n(z)$ and self-consistent potential profile $\varphi(z)$ are related as $-e\varphi(z) + \mu(z) = \varepsilon_F = 0$, where $\mu(z) \propto [n(z)]^{2/3}$ is the chemical potential of the electron gas. So $n(z)$ and $\varphi(z)$ are related as

$$\varphi(z) = \left(3\pi^2\right)^{2/3}\frac{\hbar^2}{2m^*e}\left[n(z)\right]^{2/3} \tag{2.5}$$

Thus, one can obtain the solution of Eqs. (2.1) by using relations (2.4) and (2.5), and arrive at the equation for the potential:

$$\frac{d}{dz}\left[\left(\frac{d}{dz}\frac{\varphi}{e/b}\right)^{1/3}\right] = \frac{2^{3/2}}{3\pi^2}\frac{1}{b^{4/3}}A^{1/3}\left(\frac{e/b^2}{\mathscr{P}_0}\right)^{2/3}\left(\frac{\varphi}{e/b}\right)^{3/2}. \tag{2.6}$$

With the boundary condition for a single accumulation layer $\mathscr{D}(0) = \mathscr{D}_0$ and $\varphi(\infty) = 0$, we then get the solution:

$$\varphi(z) = C_1\frac{e}{b}\left(\frac{b}{a}\right)^{8/7}\frac{1}{A^{2/7}}\left(\frac{b}{z+d}\right)^{8/7} \sim \frac{e}{a}\left(\frac{a}{z+d}\right)^{8/7}, \tag{2.7}$$

$$n(z) = C_2\frac{1}{b^3}\left(\frac{b}{a}\right)^{12/7}\frac{1}{A^{3/7}}\left(\frac{b}{z+d}\right)^{12/7} \sim \frac{1}{a^3}\left(\frac{a}{z+d}\right)^{12/7}, \tag{2.8}$$

where $C_1 = [5^6 3^6 \pi^{12}/(7^8 2^3)]^{1/7} \simeq 5.8$, $C_2 = [5^9 3^2 \pi^4 2^6/7^{12}]^{1/7} \simeq 1.3$. One can simply the expression by absorbing b/a and A into numerical coefficients using values of b, a, and A. The characteristic length d can be obtained using the neutrality condition where the number of accumulated electrons has to compensate the external field $\mathscr{D}_0$,

$$4\pi e \int_0^\infty n(z)dz = \mathscr{D}_0 = 4\pi eN. \tag{2.9}$$

Here N is the total 2D electron concentration. So

$$d = C_3 b \left(\frac{a}{b}\right)^{2/5} \left(\frac{e/a^2}{\mathscr{D}_0}\right)^{7/5} \frac{1}{A^{3/5}} \sim a\left(Na^2\right)^{-7/5}, \tag{2.10}$$

where $C_3 = (16/7)(5^2 3^2 \pi^{11})^{1/5} \simeq 84$. The above result of electron density depth profiles seems to be in good agreement with experimental data [27].

One should note that at very large distances the polarization becomes smaller and the linear dielectric response takes over. This happens when the first and second terms in Eq. (2.3) are comparable at the distance

$$z_0 = C_4 a A^{1/10} \left(\frac{b}{a}\right)^{3/5} \kappa^{7/10} \sim a\kappa^{7/10} \tag{2.11}$$

with the numerical coefficient C_4 of the order of unity [27]. z_0 is estimated to be on the order of 10^2 nm for helium temperature, which is so large that the crossover to linear dielectric response in STO accumulation layers can be ignored in most cases of our consideration.

2.2 Run-away tail in STO

In the previous section, we get the electron distribution in an accumulation layer induced in STO-based heterointerfaces which has a long tail $n(z) \propto z^{-12/7}$. If we ignore the scattering of electrons by bulk impurities, the low temperature mobility of the accumulation layer in STO is limited by the surface (interface) scattering. Therefore, the scattering rate of electrons in the body of the distribution $n(z)$ is much larger than that of electrons in the tail due to the large travel time to the surface of the tail electrons. As a result the tail contribution to different kinetic coefficients diverges. In

particular, this leads to the anomalously large mobility, Hall factor, magnetoresistance, and thermopower, which depend on the truncation mechanism of the divergences. The tail is thus named the 'run-way tail' (RAT).

2.2.1 Conductivity

Since the time an electron originally at the Fermi level of distance z spends on the journey to the surface is $\sim z/v_F(z)$ where $v_F(z) \sim \hbar n(z)^{1/3}/m^* \propto z^{-4/7}$ is the Fermi velocity and m^* is the effective electron mass, we get the corresponding relaxation time

$$\tau(z) = \tau_s \left(\frac{z}{d}\right)^{11/7}, \tag{2.12}$$

where $\tau_s \equiv \tau(d)$ is the surface scattering related relaxation time of electrons in the body of distribution (2.8). The spatially varying relaxation time $\tau(z)$ has to be averaged to calculate the surface conductivity. Usually, in bulk semiconductors when there are different kinds of carriers, e.g., electrons with the same effective mass m^* but different relaxation times, the 2D conductivity is $e^2 N\bar{\tau}/m^*$, where $N = N_1 + N_2$ is the total 2D concentration of different carriers, and the averaged relaxation time is [100]

$$\bar{\tau} = \frac{N_1\tau_1 + N_2\tau_2}{N_1 + N_2}. \tag{2.13}$$

Here the subscripts refer to the concentrations and relaxation times of the two different carriers. One can generalize Eq. (2.13) to our case where electrons at different z have different relaxation times and thus behave as if they are different carriers. The total 2D conductivity is then

$$\sigma = \frac{e^2 N \langle\tau\rangle}{m^*} \tag{2.14}$$

where similarly to Eq. (2.13), we have here

$$\langle\tau\rangle = \frac{\int_0^L dz\, n(z)\tau(z)}{\int_0^L dz\, n(z)} = \frac{\int_0^L dz\, n(z)\tau(z)}{N}. \tag{2.15}$$

Here N is the total 2D concentration of electrons. Below we always understand the averaging $\langle \dots \rangle$ in the way of Eq. (2.15). Using Eqs. (2.8) and (2.12), we then obtain

$$\sigma = \sigma_s \left(\frac{L}{d}\right)^{6/7} \tag{2.16}$$

where $\sigma_s = Ne\mu_s$, $\mu_s = e\tau_s/m^*$ is the electron mobility in the body of $n(z)$ distribution at $z \leq d$. We see that both $\langle\tau\rangle$ and σ diverge in the limit $L \to \infty$. This is why we had to introduce a finite truncation length L to the electron density tail. It can be specified for several possible truncation mechanisms: i) the finite width of the STO sample, ii) a finite bulk scattering rate, and iii) the nonlinear-linear dielectric response transition. The smallest of these values is to be substituted into Eq. (2.16).

Finite sample width W — For a sample with a relatively small width W, for example, GTO/STO/GTO structures with the STO layer of width W, the resulting conductivity is

$$\sigma = \sigma_s \left(\frac{W}{d}\right)^{6/7} \tag{2.17}$$

with L in Eq. (2.16) substituted by $W \gg d$. The expression of the relaxation time τ_s depends on the surface scattering mechanism.

Bulk scattering — Let us now consider the large W case and assume that the bulk relaxation time τ_b does not depend on the electron concentration. (A mobility independent of the electron concentration of course means that in the tail far enough from the surface where $n(z)$ becomes very small electrons should get localized. Indeed, it is known that in the bulk STO samples the localization happens at concentration $n_c \sim 3 \times 10^{16}$ cm^{-3} according to Ref. [101]. Here we deal with accumulation layers with much larger near-the-interface concentrations $n(0) \sim 10^{20}$ cm^{-3} so that other mechanisms are assumed to truncate the conductivity or the Hall factor before $n(z)$ reaches n_c. We justify this assumption in Subsec. 2.2.4.) Assuming that $\tau_b \gg \tau_s$ we can find such a distance $z = L_1$ that the relaxation time Eq. (2.12) due to surface scattering and τ_b are equal

$$\tau_s \left(\frac{L_1}{d}\right)^{11/7} = \tau_b. \tag{2.18}$$

This gives

$$L_1 = d\left[\frac{\tau_b}{\tau_s}\right]^{7/11} \gg d. \tag{2.19}$$

At $z \gg L_1$, the total relaxation time $\left[\tau^{-1}(z) + \tau_b^{-1}\right]^{-1} \approx \tau_b$ is constant and the conductivity converges. Thus, substituting L_1 for L in Eq. (2.16), we get

$$\sigma = Ne\mu_s \left[\frac{\tau_b}{\tau_s}\right]^{6/11} = Ne\mu_b^{6/11}\mu_s^{5/11} \tag{2.20}$$

where $\mu_b = e\tau_b/m^* \gg \mu_s$ is the electron mobility due to bulk impurity scattering. This gives the final value of σ only for relatively large samples when the width $W > L_1$ and σ obtained from Eq. (2.20) is smaller than Eq. (2.17). A remarkable feature of Eq. (2.20) is that the final mobility depends on both the surface and the bulk scattering and is close to the geometrical average $[\mu_b\mu_s]^{1/2}$.

Crossover to linear dielectric response — The electric field of the accumulation layer decays with z as $1/z^{15/7}$ and eventually becomes so small that the dielectric response of STO becomes linear with the large dielectric constant κ. According to previous section, this happens when z reaches

$$L_2 = z_0 \sim a\kappa^{7/10} \gg d, \tag{2.21}$$

where z_0 is given by Eq. (2.11). At $z \gg L_2$, the 3D electron concentration is [27]

$$n(z) \simeq C_5 \frac{a_B^3}{z^6} \tag{2.22}$$

where $C_5 = 1125\pi/8 \approx 442$ and the conductivity converges for this density profile. This means that at $L_2 \ll W$, L_1, we can get the conductivity substituting L_2 for L in Eq. (2.16). As a result,

$$\sigma = \sigma_s \left(\frac{L_2}{d}\right)^{6/7} \sim \sigma_s \left(Na^2\right)^{6/5} \kappa^{3/5}. \tag{2.23}$$

In this case, of course, in its range of validity Eq. (2.23) gives a smaller σ than both Eqs. (2.17) and (2.20).

2.2.2 Hall factor

In this subsection we discuss effects of a weak magnetic field B on the conductivity tensor: the Hall effect. It is known that the Hall constant is r_H/Nec, where the Hall factor according to Ref. [100] is

$$r_H = \frac{(N_1\tau_1^2 + N_2\tau_2^2)(N_1 + N_2)}{(N_1\tau_1 + N_2\tau_2)^2} \tag{2.24}$$

for two kinds of carriers with the same effective mass but different relaxation times labeled by subscripts 1, 2, and the total concentration $N = N_1 + N_2$. So again, we can

generalize this result to our case where electrons at different positions play the role of carriers with different τ. The Hall factor is then

$$r_H = \frac{\langle \tau^2 \rangle}{\langle \tau \rangle^2} \tag{2.25}$$

where the averaging is weighed by the electron 2D concentration ratio $dz\, n(z)/N$ following the form of Eq. (2.15). Using Eq. (2.12) one can see that when $\langle \tau \rangle$ diverges $\langle \tau^2 \rangle$ diverges even stronger. Therefore below we deal with the truncation of both divergences.

For relatively thin STO samples where $W \ll L_1$, L_2 and L_1, L_2 are given respectively by Eqs. (2.19) and (2.21), both divergences of $\langle \tau^2 \rangle$ and $\langle \tau \rangle$ are cut by W. According to Eq. (2.12), we get

$$\langle \tau^2 \rangle = \tau_s^2 \left(\frac{W}{d} \right)^{17/7}, \langle \tau \rangle = \tau_s \left(\frac{W}{d} \right)^{6/7} \tag{2.26}$$

so the Hall factor is

$$r_H = \left(\frac{W}{d} \right)^{5/7}. \tag{2.27}$$

When the STO sample width is larger, i.e., $W \gg L_1$, the bulk scattering becomes important before the electron density vanishes. From Sec. 2.2.1, we know that $\langle \tau \rangle$ stops diverging at this point. Meanwhile, due to the constant relaxation time τ_b at $z > L_1$, $\langle \tau^2 \rangle$ also stops diverging, so we arrive at

$$r_H = \left(\frac{L_1}{d} \right)^{5/7} \tag{2.28}$$

with L_1 here playing the role of W in Eq. (2.27). This result is valid only when the dielectric response is nonlinear at all $z < L_1$, i.e., $L_2 \gg L_1$. When $L_2 \ll L_1, W$, the divergence of $\langle \tau \rangle$ stops at $z = L_2$ but $\langle \tau^2 \rangle$ continues diverging even after this point where $n(z)$ crosses over to $\propto 1/z^6$. Indeed, in this case instead of Eq. (2.12) we get

$$\tau(z) \propto \frac{z}{v_F(z)} \propto z^3 \tag{2.29}$$

where $v_F(z) \propto n(x)^{1/3} \propto 1/z^2$. As a result $\langle \tau^2 \rangle \simeq \tau_s^2 (L_2/d)^{17/7} (L/L_2)$. To truncate this new divergence we should use the finite sample width W or the bulk scattering to obtain L. However, one should note that the position where the bulk scattering dominates changes from L_1 to L_1' now due to the new dependence of $\tau(z)$ Eq. (2.29).

Since at $z > L_2$, $\tau(z) = \tau(L_2)\,(z/L_2)^3$ where $\tau(L_2) = \tau_s\,(L_2/d)^{11/7}$ given by Eq. (2.12) at $z = L_2$, we now get $\tau(z) = \tau_b$ at $z = L_1'$ and

$$L_1' = d\left(\frac{\tau_b}{\tau_s}\right)^{1/3}\left(\frac{L_2}{d}\right)^{10/21}. \tag{2.30}$$

At $L_2 \ll L_1' \ll W$, we have

$$\begin{aligned}\left\langle\tau^2\right\rangle &= \tau_s^2\left(\frac{L_2}{d}\right)^{17/7}\left(\frac{L_1'}{L_2}\right),\\ \left\langle\tau\right\rangle &= \tau_s\left(\frac{L_2}{d}\right)^{6/7}\end{aligned} \tag{2.31}$$

and

$$r_H = \left(\frac{L_2}{d}\right)^{5/7}\left(\frac{L_1'}{L_2}\right). \tag{2.32}$$

At $L_2 \ll W \ll L_1'$, we get

$$r_H = \left(\frac{L_2}{d}\right)^{5/7}\left(\frac{W}{L_2}\right) \tag{2.33}$$

with W substituting for L_1 in Eq. (2.32). Obviously, Eqs. (2.27), (2.28), (2.32), and (2.33) are valid only for $r_H \gg 1$.

One should note that above results are valid only for the weak enough magnetic field. This means that for all relevant values of z, the inequality $\omega_c\tau(z) \ll 1$ is fulfilled, where $\omega_c = eB/m^*c$ is the cyclotron frequency. Let us now consider the large B case when $\omega_c\tau(z) = 1$ already at $z = L_3 < W$, $L_1\,(L_1')$, L_2. Using Eq. (2.12), we obtain

$$\omega_c\tau_s\left(\frac{L_3}{d}\right)^{11/7} = 1 \tag{2.34}$$

and

$$L_3 = \frac{d}{(\omega_c\tau_s)^{7/11}} \propto \frac{1}{B^{7/11}}. \tag{2.35}$$

This is the truncation length of the electron density tail by the magnetic field. The resulting Hall factor for $L_3 \gg d$ is

$$r_H = \left(\frac{L_3}{d}\right)^{5/7} \propto \frac{1}{B^{5/11}}. \tag{2.36}$$

For simplicity we skip analysis of intermediate magnetic fields where some of other truncation lengths are smaller than L_3. This brings the nonlinear Hall effect where the Hall resistance $R_{xy} \propto r_H B \propto B^{6/11}$ is approximately proportional to the square root of B. This is in reasonable agreement with experimental data as shown in Fig. 2.1.

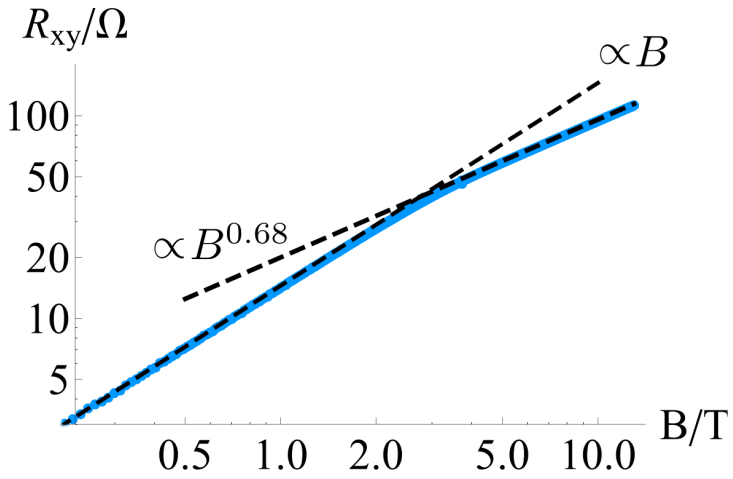

Figure 2.1: (Color online) Log-log plot of the Hall resistance R_{xy} as a function of the magnetic field B measured experimentally in STO accumulation layers. The nonlinear Hall effect is observed where R_{xy} is no longer linear in the magnetic field B at large B. The original data are given by the group doing the work of Ref. [102]. The solid line (blue) represents the experimental data taken at the largest N obtained. The dashed lines (black) are the asymptotes for the Hall resistance at small and large B, respectively. One can see that at small B when the tail is truncated by other mechanisms, the Hall effect is linear. At large B when the magnetic field truncates the tail, the Hall resistance grows approximately as $B^{0.68}$, where the power is reasonably close to our prediction $6/11 \approx 0.55$. Here the discrepancy is due to the relatively small window of L/d where L is the truncation length due to other mechanisms at small B.

2.2.3 Magnetoresistance and thermopower

Magnetoresistance — When a weak magnetic field B is applied normal to the interface, the resistivity ρ of the accumulation layer changes by $\Delta\rho = \rho(B) - \rho(0)$ where $\rho(B)$ is the magnetoresistance. According to Ref. [100] the magnetoresistance ratio at small B is

$$\frac{\Delta\rho}{\rho} = \frac{\left(\left\langle\tau^3\right\rangle\left\langle\tau\right\rangle - \left\langle\tau^2\right\rangle^2\right)\omega_c^2}{\left\langle\tau\right\rangle^2}. \tag{2.37}$$

We can repeat previous analysis for the magnetoresistance and summarize the final results in Table. 2.1.

Thermopower — Another important property of the system is its thermopower S

Table 2.1: Magnetoresistance ratio $\Delta\rho/\rho$ in units of $\tau_s^2\omega_c^2$ and thermopower S in units of $k_B^2T/e^2\varphi(d)$ in different truncation situations where τ_s is the electron relaxation time due to surface scattering in the body of $n(z)$, $\omega_c = eB/m^*c$ is the cyclotron frequency, $\varphi(d) \simeq \left(Na^2\right)^{8/5} e/a$ is the electric potential in the body of $n(z)$ according to Eq. (2.7). Here W is the width of the STO sample, d, L_1, L_2, L_1' are given by Eqs. (2.10), (2.19), (2.21), and (2.30), respectively.

	$\Delta\rho/\rho$	S
$W \ll L_1,\, L_2$	$(W/d)^{22/7}$	$(W/d)^{8/7}$
$L_1 \ll L_2 \ll W$	$(L_1/d)^{22/7}$	$(L_1/d)^{8/7}(L_2/L_1)^{3/7}$
$L_1 \ll W \ll L_2$	$(L_1/d)^{22/7}$	$(L_1/d)^{8/7}(W/L_1)^{3/7}$
$L_2 \ll L_1' \ll W$	$(L_2/d)^{22/7}(L_1'/L_2)^4$	$(L_2/d)^{8/7}(L_1'/L_2)^2$
$L_2 \ll W \ll L_1'$	$(L_2/d)^{22/7}(W/L_2)^4$	$(L_2/d)^{8/7}(W/L_2)^2$

which is the ratio of the induced electric field to the temperature gradient [100]

$$S \simeq \frac{k_B^2 T}{e} \frac{\langle \tau/\varepsilon \rangle}{\langle \tau \rangle} \propto \frac{\left\langle \tau/n^{2/3} \right\rangle}{\langle \tau \rangle} \tag{2.38}$$

where k_B is the Boltzmann constant, T is the temperature. Here $\left\langle \tau/n^{2/3} \right\rangle$ is strongly divergent and only at $z > L_1\,(L_1')$, L_2 or $z > W$ can it stops diverging. The results are shown in Table. 2.1. We find that when the sample width W truncates the tail, S grows as $\propto W^{8/7}$. This is in reasonably good agreement with experimental data as shown in Figs. 1.3 and 2.2.

2.2.4 Brief discussion of RAT assumptions and results

Relaxation time approximation — Although all the scaling derivations of transport properties of the accumulation layer in STO in previous sections were based on the relaxation time approximation, they can be justified by solving the Bolzmann kinetic equation. As we demonstrated above, these transport properties are dominated by a small fraction of the tail electrons. In this case, the collision term in the Boltzmann equation is dominated by the relaxation of this particular small fraction of electrons and therefore can be reduced to the relaxation time approximation.

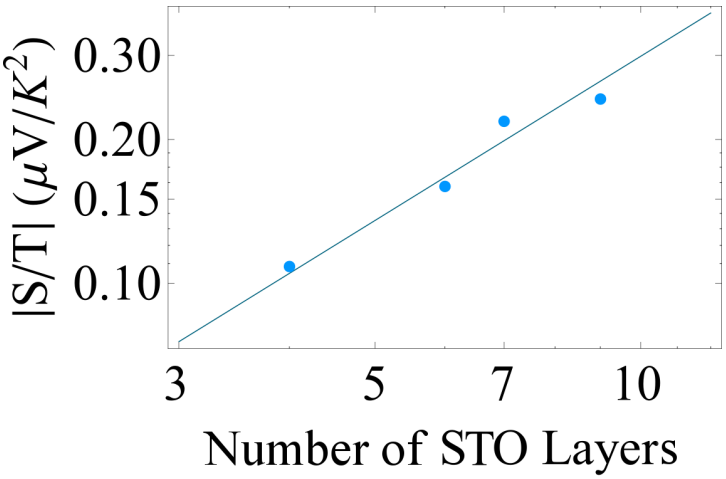

Figure 2.2: Comparison of experimental data and RAT prediction for the absolute value of the thermopower S divided by the temperature T as a function of the STO sample width in the SmTO/STO/SmTO quantum wells represented by the number of STO layers. The solid circles represent the experimental data taken from Reference [8] (from which we take only the peak values of $|S/T|$ in the measured range of T for relatively wide samples where the width W truncating the tail is large enough compared to d so that two accumulation layers formed near each SmTO/STO interface weakly overlap and can be regarded independent). The solid line denotes the fitting of the data with the scaling behavior $S/T \propto W^{8/7}$.

Fermi level in the bulk of STO — For simplicity we assumed that the bulk of STO is only lightly doped by donors so that the Fermi level in the bulk STO coincides with the conduction band bottom and the electron concentration tends to zero at large z according to Eq. (2.8). In this case, at $T = 0$ the bulk of STO is insulating and does not contribute to the surface conductivity. Actually STO crystals as grown are believed to be strongly compensated [101] so that the Fermi level is in the STO band gap. This does not affect the accumulation layer structure because the conduction band bottom acquires its bulk position only at the distance comparable with the screening radius of thermally activated electrons which is exponentially large at low temperatures. When the bulk of STO has excessive acceptors with small concentration n_A so that our accumulation layer becomes the inversion layer, even though the width of the hole depletion layer is very large, its total surface charge is much smaller than the electron surface charge N. In

this case, acceptors do not affect the electron distribution $n(z)$ and all our results above are valid. More caution is required if the bulk of STO is heavily doped by donors and, therefore, has a finite concentration of degenerate electron gas. This is easily achievable because the Bohr radius of a donor $a_B = \hbar^2\kappa/m^*e^2 \approx 700\text{nm} \gg a$. As a result the bulk is conducting and the surface conductivity of the accumulation layer should be defined as a difference between conductivity of the sample in strong applied electric field and without it. Also, the linear screening radius of the bulk electron gas truncates the accumulation layer, but because of the large dielectric constant this happens at a distance much larger than other truncation lengths. Thus, even in this case our theory remains valid.

Effect of back gate — If an STO sample with width W has a back gate, one can apply to it a voltage V. When $V < 0$ and $|V|$ is large enough, the back gate induced electric field $\mathscr{E} = -V/W$ can squeeze the electron gas truncating the tail at a new distance $Z_m(|V|) \ll W$. To find $Z_m(|V|)$, we match electric fields at this point, i.e., $\mathscr{E}(Z_m) = -d\varphi/dz = -V/W$. Using Eq. (2.7), we arrive at $Z_m \simeq a(|V|a^2/We)^{-7/15}$, which is valid if $W \gg Z_m(|V|) \gg d$. Substituting this Z_m for W into Eqs. (2.17) and (2.27), we arrive at

$$\sigma = \sigma_s \left(\frac{a}{d}\right)^{6/7} \left(\frac{|V|a^2}{We}\right)^{-2/5} \tag{2.39}$$

and

$$r_H = \left(\frac{a}{d}\right)^{5/7} \left(\frac{|V|a^2}{We}\right)^{-1/3}. \tag{2.40}$$

Applicability of Thomas-Fermi approach — All our results are based on Eq. (2.8) for the electron density distribution, which was derived in the Thomas-Fermi (TF) approximation. Here we discuss the applicability of such an approximation. The TF approximation works if the potential varies at distances much larger than the electron wave length, or more exactly, when the TF parameter $k_F z \gg 1$. We showed [27] that $k_F d \simeq 3$ even at the very large $N = 0.5\ a^{-2}$ achieved in the GTO/STO heterostructure. Generally speaking at $z \gg d$, where $k_F \sim n(z)^{1/3} \sim a^{-3/7} z^{-4/7}$ we get that the TF parameter $k_F z \sim (z/a)^{3/7} \gg 1$ and grows with z. It reaches its maximum value $\kappa^{3/10}$ at $z = L_2$, where the crossover to the linear dielectric response happens. At $z > L_2$ Eq. (2.22) gives $k_F \propto 1/z^2$ so that the TF parameter $k_F z$ decreases as $1/z$ and at $z = a_B$ becomes of the order of 1. The accumulation layer terminates at $z = a_B$ so that a_B is

another truncation length, which we have not considered in Subsecs. 2.2.1, 2.2.2, and 2.2.3 because in STO $a_B \approx 700$ nm is larger than all other truncation lengths. Thus, the use of the TF approach is well justified.

Bulk relaxation time — In compensated STO at low temperatures electrons are scattered by charged donors and acceptors with total concentration $n_i \sim 5 \times 10^{18}$ cm^{-3}. We assumed above that the resulting bulk relaxation time τ_b does not depend on the electron concentration n. We can justify this assumption by appealing to experimental data summarized in Refs. [101, 103]. It was shown there that in STO samples intentionally heavily doped by Nb donors at the level of $10^{18} < n < 4 \times 10^{20}$ cm^{-3} on the top of existing n_i donor and acceptors their 3D conductivity weakly depends on the 3D electron concentration of electrons n. This indicates that $\tau_b \propto n^{-1}$ when the scattering happens on donors of concentration n. This means that Σv_F does not depend on n. Here Σ is the scattering crosssection and v_F is the Fermi velocity. Returning to undoped STO samples with n_i donor and acceptors as scatterers we see that $\tau_b = (n_i \Sigma v_F)^{-1}$ does not depend on n.

Surface relaxation time — Above, we have not specified the relaxation time τ_s of electrons in the body of the electron distribution (2.8) due to the surface scattering and the corresponding mobility μ_s. They can be limited by scattering on ionized donors and surface roughness. First, let us imagine that the surface has ionized impurities with the 2D concentration N_s. The effective bulk concentration of the scattering centers is N_s/d. From the experimental data [101, 103], we know that Σv_F weakly depends on the electron concentration n, which leads to the mobility

$$\mu_s \simeq \frac{e}{\hbar N_s}\frac{d}{a} \simeq \frac{e}{\hbar N_s}\frac{1}{(Na^2)^{7/5}}.$$

There are many reasons for the existence of charged impurities near the surface. For example, it is believed, that the interface $LaAlO_3/SrTiO_3$ has a large number of charged impurities with the 2D concentration N_s and the electron surface concentration $N \neq N_s$ due to redistribution of ions near the interface [104]. Also, due to the discreteness of ions the gating of STO by ionic liquid is equivalent to the introduction of random Coulomb centers near the surface of STO as was shown in the case of Si [62, 63].

At even larger concentration the mobility is limited by the surface roughness. The case for the accumulation layer without nonlinear dielectric response is considered in

detail in Chapter 4. We assumed that the scattering occurs on the islands with typical diameter Λ and height Δ. We arrived at that the relaxation time is:

$$\tau_s \simeq \frac{m^*}{\hbar}\frac{d\Lambda}{k_F^2\Delta^2}\begin{cases}\Lambda^{-3}k_F^{-3} & \text{if } k_F^{-1} \gg \Lambda \\ 1 & \text{if } k_F^{-1} \ll \Lambda.\end{cases}$$

For the nonlinear dielectric response case, we get the same result in terms of $k_F \simeq [\, n(0)\,]^{1/3}$ and d since here we can also describe the surface electrons as located within a certain distance d from the interface and having a Fermi wavenumber k_F, which is the same as the model used in Chapter 4 and thus leads to the same expression in terms of these variables. The dielectric response will only affect the specific dependence of k_F and d on N. Now using the relationship between d, k_F, and N for the nonlinear dielectric response Eqs. (2.8) and (2.10) we arrive at the corresponding mobility:

$$\mu_s \simeq \frac{e}{\hbar}\frac{1}{N}\frac{a\Lambda}{\Delta^2}\begin{cases}\dfrac{a^3}{\Lambda^3}(Na^2)^{-22/5} & \text{if } Na^2 < (a/\Lambda)^{5/4} \\ \\ (Na^2)^{-2} & \text{if } Na^2 > (a/\Lambda)^{5/4}\end{cases}$$

(where for simplicity, b/a and A are absorbed into numerical coefficients which are typically on the order of unity and ignored here). At large N where $Na^2 > (a/\Lambda)^{5/4}$, putting $\Delta \sim a \ll \Lambda$, we then get Eq. (1.3) where the prefactor $a\Lambda/\Delta^2$ much larger than unity.

Beyond isotropic effective mass approximation — Here following Ref. [27] we assumed that the electron spectrum at the bottom of the conduction band of STO can be approximated by the single isotropic band with the effective mass m^*. Actually, near the conduction band bottom of STO are three degenerate bands formed by xy, xz and yz Ti d-orbitals, which are anisotropic with the heavy mass direction along the z, y, and x axes, respectively. The splitting of these bands by the spin-orbit interaction [98] can be ignored at relatively large electron concentrations $10^{19} < n < 10^{22}$ cm^{-3} which we are interested in for accumulation layers with very large surface concentration N. Indeed, at electron concentrations larger than 10^{19} cm^{-3}, all energy bands are almost equally occupied so that the effective mass measured by the specific heat $m^* \simeq 1.5\ m_e$ [105] does not change with n. One should note that m^* describes the total density of states of all three bands. Our TF theory of the accumulation layer uses only the density

of states. Thus, it is valid to use the effective mass m^* when the TF criterion $k_F z \gg 1$ is fulfilled for all bands at all $z \geq d$. In this case, our Eq. (2.8) is justified for both the body and the tail of the $n(z)$ distribution. When $N \ll 1/2a^2$ the electron distribution $n(z)$ is so wide ($d \gg a$) that the TF criterion is easily fulfilled for all bands. However, for the largest concentration $N = 1/2a^2$, where d becomes comparable with the lattice constant the two bands with the light mass along the z axis may only marginally satisfy the TF criterion. Near $z = 0$, this depletes their contribution to the density of states and reduces the maximum value of $n(z)$. However, in the tail the TF criterion is still valid. Thus, the tail of $n(z)$ which plays the major role here still follows Eq. (2.8). This conclusion agrees with numerical results for $n(z)$ obtained for $N = 1/2a^2$ in Refs. [27, 21, 22, 106].

Beyond STO – Above we dealt with accumulation layers in STO where the linear dielectric constant is very large and and dielectric response is strongly nonlinear. Our results are directly applicable to the very similar $KTaO_3$ and $CaTiO_3$ and to other materials with very large dielectric constant. The similar approach is also applicable to accumulation layers with large concentration of electrons in semiconductors with unremarkable dielectric properties such as Si [62, 63] or ZnO [64]. In such a crystal the dielectric response is linear and the electron concentration at low temperatures behaves as

$$n(z) = C_5 \frac{a_B^3}{(d_1 + z)^6}, \tag{2.41}$$

where [27]

$$d_1 \simeq a_B/(N a_B^2)^{1/5} \tag{2.42}$$

is the new decay length of the electron distribution from the surface (where the numerical coefficient is around 2 and can be found in Ref. [27]), N is the total 2D electron density, a_B is the Bohr radius of the semiconductor, $C_5 \approx 442$. In this case, using Eqs. (2.29) and Eq. (2.22) we arrive at the converging conductivity. However, the Hall factor, the magnetoresistance, and the thermopower diverge. For a weakly doped uncompensated bulk crystal with large width W where the bulk relaxation time τ_b provides a large truncation length, the divergence is cut by the failure of the TF approximation at $z = a_B$ similarly to the termination of the standard TF atom electron density. The

results for the Hall factor, the magnetoresistance, and the thermopower then are

$$\begin{aligned} r_H &\simeq \left(Na_B^2\right)^{1/5}, \\ \frac{\Delta\rho}{\rho} &\simeq (\omega_c\tau_s)^2 \left(Na_B^2\right)^{4/5}, \\ S &\simeq \frac{k_B}{e}\left[\frac{k_BT}{e\varphi(d)}\right]\left(Na_B^2\right)^{2/5}, \end{aligned} \tag{2.43}$$

where τ_s is the surface scattering relaxation time of electrons in the body of electron distribution, $e\varphi(d) = \left(e^2/\kappa_1 a_B\right)\left(Na_B^2\right)^{4/5}$ is the depth of the Fermi sea near the surface [27] and κ_1 is the dielectric constant of the semiconductor. In Si and ZnO one can achieve $Na_B^2 \sim 5$ so that one can see substantial anomalies.

Chapter 3

Electron distribution in complicated STO-based planar structures and around spherical and cylindrical donor clusters in bulk STO

In this chapter, we are dealing with the potential and electron density depth profiles due to the nonlinear dielectric response in various complicated planar STO structures and in bulk STO around donor clusters where the geometry is spherical or cylindrical. In particular, for the planar structures, using the basic solution for a separate accumulation layer explained in Chapter 2, we study more complicated problems where accumulation layers overlap, e.g., in GTO/STO/GTO multi-heterojunctions [34, 35, 36] with electron density profiles evolving as a function of the distance between two heterointerfaces or when the accumulation layer is created in STO which is a part of the modulation doped structure of NSTO/STO [37, 38, 39, 40, 41]. For bulk STO where electrons are given by donor clusters, we find the electron collapse and charge renormalization phenomena for spherical and cylindrical donor clusters, respectively. Such " fall-to-the-center" collapse originates from the very fast decrease of the electron potential energy near the cluster

which is $\propto (-1/r^5)$ in the spherical case and in turn is a result of the strongly nonlinear dielectric response of STO. This leads to a very unusual two-scale shape of the electron density around the cluster. We show how one can verify such a shape experimentally.

3.1 Complicated planar structures

3.1.1 Two overlapping accumulation layers

In Sec. 2.1 of Chapter 2, we have investigated a single accumulation layer induced in STO. In the GTO/STO/GTO structure [34, 35, 36], an accumulation layer forms near each interface and these two layers overlap with each other. When the STO layer is thick, one can expect that the two accumulation layers overlap weakly by the vanishing tails and the final electron distribution can be described as a simple addition of two accumulation layers given by Eq. (2.8). However, as the STO layer gets thinner, the overlap becomes stronger. Due to the nonlinear physics here, the electron density profile changes substantially. Below we study the density profile of the electron gas in the GTO/STO/GTO structure where the width of the STO layer is W (see Fig. 1.4).

To make the mathematics more compact, in Sec. 3.1, we employ the dimensionless notations, in which Eq. (2.6) is rewritten as

$$\frac{d}{d\zeta}\left(\frac{d\chi}{d\zeta}\right)^{1/3} = B\chi^{3/2}, \quad \zeta > 0. \tag{3.1}$$

Here $\zeta = z/b$ is the scaled distance from one interface, $\chi = \varphi/(e/b)$ is the potential in the units of e/b, and $B = 2^{3/2}(a/b)^{4/3}A^{1/3}/3\pi^2$. Also, from Eq. (2.5), we know

$$n(z) = \frac{C_6}{b^3}\left[\frac{\varphi(z)}{e/b}\right]^{3/2}, \tag{3.2}$$

where $C_6 = 2^{3/2}/3\pi^2 \approx 0.1$. The electron density $n(z)$ can be scaled as $\widetilde{n}(\zeta) = A^{1/3}(a/b)^{4/3}n(z)b^3$ and we then get

$$\widetilde{n}(\zeta) = B\chi^{3/2}, \tag{3.3}$$

which is the dimensionless form of the TF approximation. The width of the STO layer is scaled as $\widetilde{W} = W/b$.

According to Eq. (3.1), we can get

$$\frac{d\chi}{d\zeta} = -\left(\frac{8}{5}B\chi^{5/2} + g_1\right)^{3/4}, \tag{3.4}$$

where g_1 is a constant arising from the integration. By integrating Eq. (3.4), we get

$$\int_{\chi(\widetilde{W}/2)}^{\chi(0)} \frac{d\chi}{\left(8B\chi^{5/2}/5 + g_1\right)^{3/4}} = \int_0^{\widetilde{W}/2} d\zeta = \widetilde{W}/2. \tag{3.5}$$

In this structure, each GTO/STO interface provides a fixed number of electrons to the accumulation layer inside STO which is $e/2$ per unit cell with the interfacial induction $\mathscr{D}_0 = 4\pi e/2a^2$. Using Eq. (2.4), this gives the value of $d\chi/d\zeta$ on the $\zeta = 0$ and $\zeta = \widetilde{W}$ interfaces, which is $\propto \mathscr{E} \propto \mathscr{D}_0^3$. Due to the symmetry, the electric field is zero in the middle of the STO layer which means $d\chi/d\zeta = 0$ at $\zeta = \widetilde{W}/2$. We can choose a value for g_1 and calculate $\chi(\widetilde{W}/2)$ and $\chi(0)$ using Eq. (3.4). Then we can put boundary values of χ into Eq. (3.5) and get the corresponding value of $\widetilde{W}(g_1)$. Reversing $\widetilde{W}(g_1)$, we find the function $g_1(\widetilde{W})$. Therefore, at any given value of $\widetilde{W}$ we can pin down g_1 and use Eq. (3.4) to numerically get the whole electron profile inside STO.

To realize this, we need to try various values of g_1 and tune accordingly until we find the $\widetilde{W}$ we want. In this process, it is necessary to know what values of g_1 are physically possible. It is obvious that the extreme values of g_1 appear at $\widetilde{W} \to 0$ and $\widetilde{W} \to \infty$. For the former case, electrons are almost uniformly distributed over the thin STO layer with $d\chi/d\zeta \simeq 0$ and the electron density is approximately $1/a^2W$ everywhere which gives the value of χ inside STO by Eq. (3.3) (see Fig. 1.5). From Eq. (3.4), we know at $d\chi/d\zeta = 0$, a bigger value of χ corresponds to a smaller value of g_1. Thus, in this case we get the minimum value of g_1 as

$${g_1}^{min} = -\frac{8\left[A^{1/3}(b/a)^{2/3}/\widetilde{W}\right]^{5/3}}{5B^{2/3}}. \tag{3.6}$$

Since $\widetilde{W}$ can be arbitrarily small (the lattice constant a is regarded as infinitesimal), we get in fact ${g_1}^{min} = -\infty$.

In the latter case where the STO layer is very thick, the two interfaces are quite independent and tails of accumulation layers barely overlap. So, near the center of the STO layer where $d\chi/d\zeta = 0$, the electron density vanishes. This gives the maximum

value of g_1 as ${g_1}^{max} = 0$. In this case, the electron distribution is close to the simple addition of two accumulations layers described by Eq. (2.8) (see Fig. 1.5).

So we get the domain of g_1 as $(-\infty, 0]$. This means we can choose whatever value for g_1 and get physically meaningful results. By trying different values of g_1, we can find the electron density profiles at certain $\widetilde{W}$ that we are interested in. In Fig. 1.5, we show our results for electron density profiles at 3 different values of W. We see the evolution from an almost constant $n(z)$ at $W = 4a$ around which the quantum criticality is observed [36] to the one reminiscent of two weakly overlapping tails of accumulation layers described by Eq. (2.8) at $W = 16a$.

It is easy to see that $n(z)$ is quite flat near the middle. This is actually an effect of the nonlinear dielectric response as we show below. Indeed, due to the symmetry of the structure, for the potential $\chi(\zeta)$, derivatives of odd order including $d\chi/d\zeta$ are all vanishing in the middle. Using Eq. (3.1), the second-order derivative $d^2\chi/d\zeta^2$ is found to be proportional to $d\chi/d\zeta$ and is then also zero at $\zeta = \widetilde{W}/2$ while the fourth-order is nonzero.

This explains why the density changes so slowly near the middle of the STO layer. We emphasize again that this "flattening" effect originates from the nonlinear dielectric response. When the response is linear, the differential equation is different [27] and the second-order derivative $d^2\chi/d\zeta^2$ is nonzero even at $d\chi/d\zeta = 0$. The density change near the middle is then faster.

3.1.2 Spill-out of electrons from heavily doped n-type STO (NSTO) into STO

In the NSTO/STO junctions [37, 38], the interface is formed between a moderately n-type doped STO with the Fermi level close to the conduction band bottom (below we simply denote it as STO) and a heavily n-type doped STO (NSTO), which has a much higher Fermi level. We start from considering a single junction between thick layers of NSTO and STO. In this case as a result of the original difference between Fermi levels electrons spill out into STO to create a common Fermi level and the total number of spilled electrons depends only on the doping level inside NSTO. Below, we study the electron distribution for this scenario (see Fig. 3.1) assuming that the donor concentration in NSTO is so large that dielectric response is nonlinear. (The linear case

of such spill-out problems was first addressed by Frenkel [69].)

Inside NSTO, the charge concentration is $[n_0 - n(z)]e$ where n_0 is the density of the positive background charge inside the doping layer and $n(z)$ is the electron density at distance z from the interface. According to the Thomas-Fermi approximation, we have

$$\frac{d}{d\zeta}\left(\frac{d\chi}{d\zeta}\right)^{1/3} = B\chi^{3/2} - \widetilde{n}_0, \quad \zeta \leq 0. \tag{3.7}$$

Here $\widetilde{n}_0 = A^{1/3}(a/b)^{4/3} n_0 b^3$ is the scaled background charge concentration. From Eq. (3.7), it can be derived that

$$\frac{d\chi}{d\zeta} = -\left(\frac{8}{5}B\chi^{5/2} - 4\widetilde{n}_0\chi + g_2\right)^{3/4}, \quad \zeta \leq 0 \tag{3.8}$$

where g_2 is a constant that we determine from the boundary conditions. Since at $\zeta \to -\infty$, $\widetilde{n}(\zeta) = \widetilde{n}_0$, we have $d\chi/d\zeta = 0$ and $\chi = (\widetilde{n}_0/B)^{2/3}$. Therefore,

$$g_2 = \frac{12}{5}\frac{\widetilde{n}_0^{5/3}}{B^{2/3}}. \tag{3.9}$$

Now let us switch to the STO side. By rewriting Eq. (2.7) in the dimensionless form, we have in STO

$$\chi = \frac{\chi_c}{(\zeta + \widetilde{d})^{8/7}}, \quad \zeta > 0 \tag{3.10}$$

which gives

$$\frac{d\chi}{d\zeta} = -\left(\frac{8}{5}B\chi^{5/2}\right)^{3/4}. \tag{3.11}$$

Here $\widetilde{d} = d/b$ is the scaled decay length and $\chi_c = \left(2^3 5^3/7^4 B^3\right)^{2/7}$. Since the interfacial field $\mathscr{D}_0$ is now no longer a fixed value, we cannot use Eq. (2.10) to get the decay length. Instead, using the boundary condition that χ and $d\chi/d\zeta$ are continuous at $\zeta = 0$ which satisfy both Eqs. (3.8) and (3.11), we then have

$$g_2 = 4\widetilde{n}_0\chi(0) = \frac{4\widetilde{n}_0\chi_c}{\widetilde{d}^{\,8/7}}. \tag{3.12}$$

Together with Eq. (3.9), we then have

$$\widetilde{d} = \left(\frac{5\chi_c}{3}\right)^{7/8}\left(\frac{B}{\widetilde{n}_0}\right)^{7/12}, \tag{3.13}$$

which gives the expression for the decay length.

Now we get the electron distribution inside STO. Using the differential equation (3.8) and the boundary values of χ and $d\chi/d\zeta$ at $\zeta = 0$, the electron density profile inside NSTO can also be obtained numerically. A schematic plot of the electron distribution is presented in Fig. 3.1. This is the universal curve independent of the value of n_0.

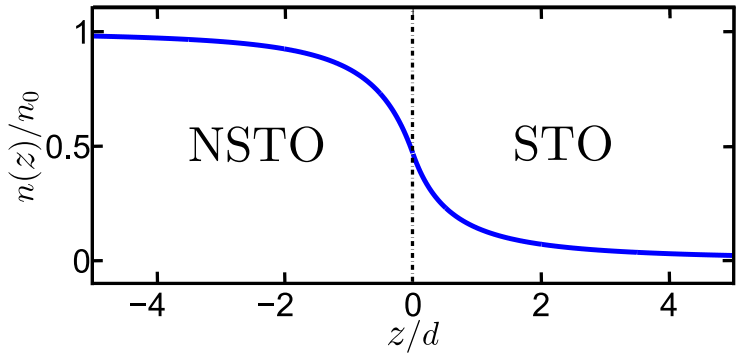

Figure 3.1: The electron distribution in a single NSTO/STO junction. The distance z is in units of the decay length $d = b\widetilde{d}$. The electron density $n(z)$ is in units of the donor concentration n_0. This figure is universal for all values of n_0.

Let us now dwell on the case of a heavily doped NSTO layer with the width W' embedded in STO (STO/NSTO/STO structure). Experimentally used δ layers have sharp boundaries [107] with well defined volume concentration n_0. One can imagine two limiting cases. When NSTO layer is so wide that its width W' is much larger than the width of the electron gas in STO, one can use the above single-junction theory for the two separate STO/NSTO and NSTO/STO junctions.

In the opposite case when W' is much smaller than the width d of the electron gas on each side, most of electrons are located outside of such δ-layer. As a result the effective two-dimensional charge density $W'n_0$ creates two accumulation electron gases on both sides from the δ-layer. The external electric field for each gas is $\mathscr{D}_0 = 2\pi e n_0 W'$. The width of the gas is determined by Eq. (2.10).

Let us now address more complicated periodic structures formed by NSTO and STO [39, 40, 41] (see Fig. 3.2). Inside each NSTO layer, the potential should satisfy Eq. (3.8)

while in STO, it obeys Eq. (3.4). Similar to Eq. (3.5), we get

$$\int_{\chi(0)}^{\chi(-\widetilde{W}'/2)} \frac{d\chi}{\left(8B\chi^{5/2}/5 - 4\widetilde{n}_0\chi + g_2\right)^{3/4}} = \int_{-\widetilde{W}'/2}^{0} d\zeta = \widetilde{W}'/2. \tag{3.14}$$

where $\widetilde{W}' = W'/b$ and $\widetilde{W}'$ is the dimensionless width of the NSTO layer. Similarly to what we have done above, we can choose certain values for g_2 and $\chi(0) = \chi_0$ where $\chi(0)$ is the scaled potential on the interface. Then we can calculate corresponding $\widetilde{W}'$ and $\widetilde{W}$ and the electron density profile. Thus, in reverse, at any given $\widetilde{W}'$ and $\widetilde{W}$ we can find the electron distribution.

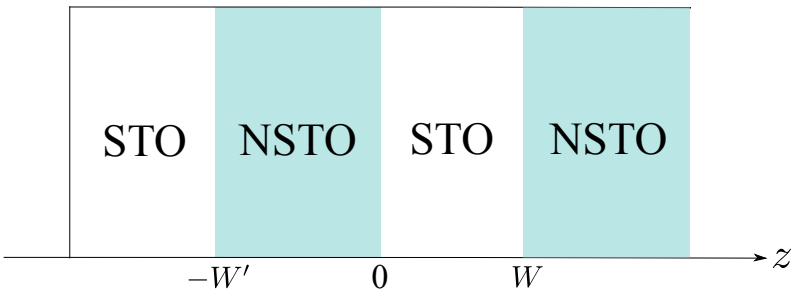

Figure 3.2: Periodic NSTO/STO structure. The width of the NSTO layer is W' and the width of the STO layer is W.

Again, we need to find the physical range of g_2 and χ_0, which can be done similarly to what we did in Subsec. 3.1.1. Given values of $\widetilde{W}'$ and $\widetilde{W}$, we try different g_2 and χ_0 from their domains until we find the $\widetilde{W}'$ and $\widetilde{W}$ we want. In this way, we get the electron distribution for 3 different values of $\widetilde{W}$ in Fig. 3.3 (for simplicity, we choose $\widetilde{W}' = \widetilde{W}$ here). We see that as $W = b\widetilde{W}$ increases, the periodic electron density profile $n(z)$ evolves from being relatively constant to strongly oscillating. Again, one can see a "flattening" effect near the middle of each layer, either STO or NSTO. Like what we did in Subsec. 3.1.1, one can verify that all derivatives of χ vanish in the middle of both layers until the fourth-order one.

Let us also dwell on a recently discovered new type of STO-based heterojunction formed by STO and $NdTiO_3$ (NTO). In this structure, the ceiling of the valence band created by the Mott gap in NTO is above the bottom of the conduction band of STO

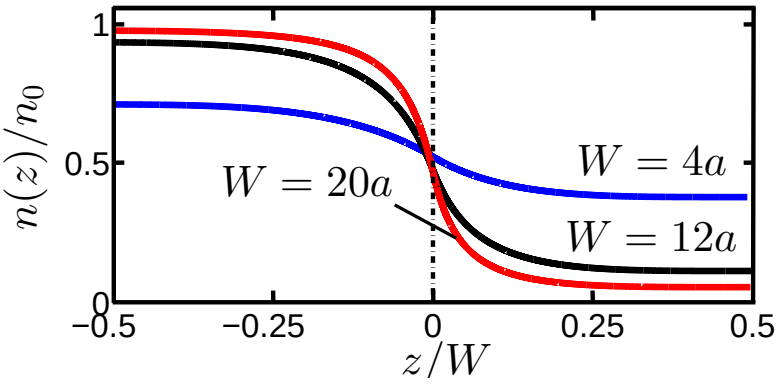

Figure 3.3: (Color online) Electron distribution from $-W'/2$ to $W/2$ plotted at $W' = W$ for different values of W. The thick solid lines are the electron density $n(z)$ in the unit of n_0 where n_0 is the donor concentration in NSTO (red: $W = 20a$; black: $W = 12a$; blue: $W = 4a$). This graph is plotted at $n_0 = 0.5/a^3$ where a is the lattice constant. As the layers get thinner, the electron distribution gets more uniform, deviating from the one shown in Fig. 3.1.

[108, 109]. So in addition to the "polar discontinuity" [4, 110, 111], the broken-gap band alignment further brings electrons into STO by the electron "spill-out" and the electron distribution becomes more complicated. One can basically use the methods we employed in this section to solve the problem. The difference due to the presence of the "polar discontinuity" is the abrupt jump of the induction field on the interface which gains an additional value of $4\pi e/2a^2$ when going from NTO to STO. One should note that the dielectric response inside NTO is linear. Therefore one gets an expression of the potential derivative $d\chi/d\zeta$ different from Eq. (3.8). Also one should know the density of states below the Mott gap in NTO in order to solve for the electron distribution. The rest of the procedure is quite similar and one can then obtain the electron density profile in this structure.

3.2 Electron collapse and charge renormalization in 3D and 2D geometries

3.2.1 Spherical Donor Clusters

So far, we have considered only the planar structures based on STO. In this section, we extend our studies to other non-planar geometries (spherical and cylindrical). To make the physics clearer, we return to the dimensional expressions for physical quantities from now on.

Renormalization of Charge

Consider a large spherical donor cluster of the radius R and the total positive charge Ze such that $a \ll R < \kappa b/Z$ (for example, R can be 3 nm and $Z \simeq 60$). If the dielectric response is linear, the electrons are mainly located at distances between $r_1 = \kappa b/Z$ and $r_A = \kappa b$ from the cluster [47]. For a very large κ, these radii are huge ($r_A = 700$ nm in STO at liquid helium temperature) and the electrons are far away from the cluster. However, at small distances, the dielectric response is nonlinear and changes the potential form. If the potential energy outweighs the kinetic energy, electrons are attracted to the cluster and renormalize the net charge. To see when this happens, we look at the specific form of electric potential in this situation. We can calculate the potential from the differential equations (3.15a) and (3.15b) applicable to the spherical structure:

$$\left(\frac{d}{dr}+\frac{2}{r}\right)\left(\frac{d\varphi}{dr}\right)^{1/3} = \frac{A^{1/3}e}{\mathscr{P}_0^{2/3}}\left[n(r)-n_0\right],\ r<R \tag{3.15a}$$

$$\left(\frac{d}{dr}+\frac{2}{r}\right)\left(\frac{d\varphi}{dr}\right)^{1/3} = \frac{A^{1/3}e}{\mathscr{P}_0^{2/3}}n(r), \qquad r>R \tag{3.15b}$$

where r is the radius from the cluster center, $n(r)$ is the electron density at radius r and n_0 is the donor concentration inside the cluster. However, due to the simple charge distribution here, we can get the potential in an easier way. At $r > R$, the sphere looks like a point charge and $\mathscr{D}(r) = Ze/r^2$. Using this together with Eqs. (2.1) and (2.3), one can calculate the electric field and get the electric potential $\varphi(r)$ as:

$$\varphi(r) = \frac{A}{\mathscr{P}_0^2}\left(\frac{Ze}{4\pi}\right)^3\frac{1}{5r^5}, \qquad R<r\ll r_1 \tag{3.16}$$

with $\varphi(r=\infty)$ defined as zero. Inside the cluster at $r < R$, since the charge is uniformly distributed over the sphere, the total positive charge enclosed in the sphere of radius r is equal to Zer^3/R^3, so $\mathscr{D}(r) = Zer/R^3$. One then gets the corresponding potential $\varphi(r)$:

$$\varphi(r) = \frac{A}{\mathscr{P}_0^2}\left(\frac{Ze}{4\pi}\right)^3\left(\frac{9}{20}\frac{1}{R^5} - \frac{1}{4}\frac{r^4}{R^9}\right), 0 < r < R \tag{3.17}$$

using the boundary condition $\varphi(r = R^-) = \varphi(r = R^+)$. A schematic graph of the potential energy $U(r) = -e\varphi(r)$ is shown in Fig. 3.4 by the thick solid line (blue).

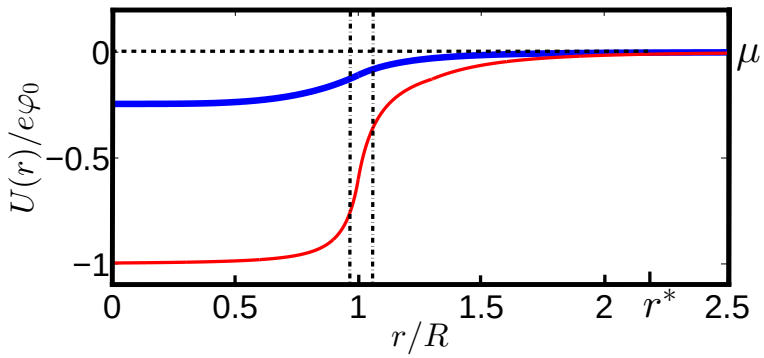

Figure 3.4: (Color online) Potential energy of electrons $U(r) = -e\varphi(r)$ caused by the spherical donor cluster of radius R as a function of distance r from the cluster center. φ_0 is defined as $n(\varphi_0) = n_0$, where $n_0 = 3Z/4\pi R^3$, $n(r)$ is a function of $\varphi(r)$ given by Eq. (3.2). The thick solid line (blue) represents the potential profile of a cluster of charge $Z \lesssim Z^*$ which is in the regime of weak charge renormalization. The thin solid line (red) represents the potential of a cluster at $Z \gg Z^*$ in the strong renormalization regime, where the two vertical dotted lines show edges of the "double-layer" structure of width $\sim d \ll R$. The horizontal dashed line (black) indicates the position of the chemical potential $\mu = 0$. r^* is the external radius of the collapsed electron gas where Thomas-Fermi approach fails.

The Hamiltonian for a single electron is $H = p^2/2m^* - e\varphi(r)$, where p is the momentum of the electron and m^* is the effective electron mass in STO [27]. If we approximately set $p \simeq \hbar/2r$, we get a positive total energy of the electron everywhere when Z is very small. This means there are no bound states of electron in the cluster. However, when Z is big enough so that $Z > Z_c$, the electron can have negative total

energy at $r < R$ and will collapse into the cluster. Using Eqs. (3.16) and (3.17), we find

$$Z_c \approx \frac{4\pi(b/Aa)^{1/3}R}{a} \sim \frac{R}{a} \gg 1. \tag{3.18}$$

As Z continues increasing, more and more electrons get inside the cluster filling it from the center where the potential energy is lowest (see Fig. 3.4). The single-electron picture no longer applies. Instead, we use the Thomas-Fermi approximation [47] with the electrochemical potential $\mu = \varepsilon_F = 0$ (please note that in this section we use μ to denote ε_F, which is different from other places), which gives Eq. (3.2). (We continue to assume here that the bulk STO is a moderately doped semiconductor.)

When the number of collapsed electrons S_c is small, their influence on the electric potential is weak. One can still use Eqs. (3.16) and (3.17) for $\varphi(r)$ and get the corresponding expression of $n(r)$. At $r > R$, since $\varphi(r)$ is $\propto 1/r^5$, we get $n(r) \propto 1/r^{15/2}$. In this way, we calculate S_c as

$$S_c = \int_0^\infty n(r) 4\pi r^2 dr = 0.5Z \left(\frac{Z}{Z^*}\right)^{7/2} \propto Z^{9/2}, \tag{3.19}$$

where

$$Z^* = \left[\frac{4\pi(b/Aa)^{1/3}R}{a}\right]^{9/7}, \tag{3.20}$$

The net charge number of the cluster is

$$Z_n = Z - S_c = Z\left[1 - 0.5\left(\frac{Z}{Z^*}\right)^{7/2}\right]. \tag{3.21}$$

One can see, when $Z_c \ll Z \ll Z^*$, one gets $S_c \ll Z$ and $Z_n \lesssim Z$, meaning the charge renormalization is weak. However, at $Z \sim Z^*$, according to Eqs. (3.19) and (3.21), we get $Z_n \sim S_c \sim Z^*$. The potential contributed by electrons is no longer perturbative. This brings us to the new regime of strong renormalization of charge.

We show that at $Z \gg Z^*$ the net charge $Z_n e$ saturates at the level of $Z^* e$. Indeed, when Z grows beyond Z^*, Z_n can not go down and therefore can't be much smaller than Z^*. At the same time it can not continue going up, otherwise as follows from Eqs. (3.16) and (3.19) with Z replaced by $Z_n \gg Z^*$, the total electron charge surrounding the charge $Z_n e$ at $r > R$ would become $S_c e \simeq Z_n e(Z_n/Z^*)^{7/2} \gg Z_n e$ leading to a

negative charge seen from infinity. Thus, at $Z \gg Z^*$, the net charge Z_n saturates at the universal value of the order of Z^*, which is shown in Fig. 1.6. This result is qualitatively similar to the one obtained for heavy nuclei and donor clusters in Weyl semimetals and narrow-band gap semiconductors in Ref. [49] ash shown in Fig. 3.5.

In the following subsection, we show how the renormalization of charge at $Z \gg Z^*$ is realized through certain distribution of electrons, in which a structure of "double layer" (see Fig. 3.4) plays an important role.

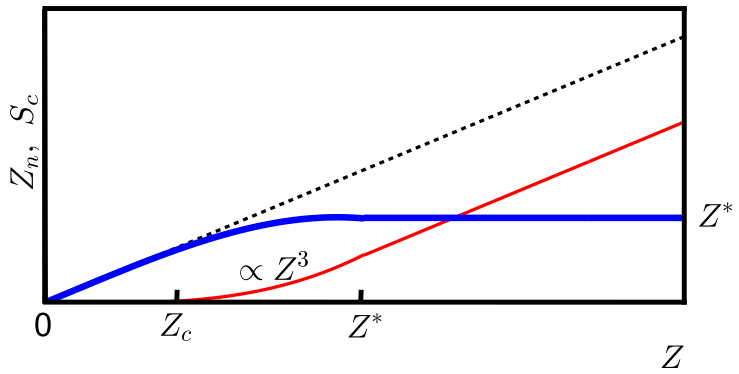

Figure 3.5: (Color online) The number of collapsed electrons S_c and the renormalized net charge $Z_n e$ as a function of the original charge Ze for highly charged nuclei. S_c is shown by the thin solid line (red), Z_n is denoted by the thick solid line (blue), and the dashed line (black) is a guide-to-eye where $Z_n = Z$. Z_c denotes the critical value where electrons begin to collapse and Z^* is the saturation point where Z_n stops growing. $S_c \propto Z^3$ at $Z_c \ll Z \ll Z^*$ (see Ref. [112]).

Radial Distribution of Electrons

At $Z \gg Z^*$, the charge renormalization is strong and the most of the sphere of radius R is completely neutralized by electrons. In the neutral center of the sphere, the electron density $n(r) = n_0$, where $n_0 = 3Z/4\pi R^3$ is the density of the positive charge inside the cluster. The corresponding "internal" electric potential $\varphi_{in}(r) = \varphi_0$ where φ_0 is given by $n(\varphi_0) = n_0$ using Eq. (3.2). $\varphi_{in}(r)$ is then $\propto (n_0 a^3)^{2/3} \propto [Z/(R/a)^3]^{2/3}$. Outside the cluster, when the charge is renormalized to Z_n, one gets a potential $\varphi_{out}(r)$ similar to Eq. (3.16) with Z replaced by Z_n. Since Z_n is $\sim Z^*$ where Z^* is given by Eq.

(3.20), we get $\varphi_{out}(r) \propto (R/a)^{-8/7}$ at a distance r of the order R. Thus, close to the cluster surface, the ratio of the outside potential $\varphi_{out}(r)$ to the inside potential $\varphi_{in}(r)$ is $\simeq (R/a)^{6/7}/Z^{2/3} \ll 1$ since $Z \gg Z^* \simeq (R/a)^{9/7}$. This indicates a sharp potential drop across the sphere surface.

At $0 < R - r \ll R$, there's a thin layer of uncompensated positive charges. At $0 < r - R \ll R$, a higher potential than farther away means a larger electron concentration that forms a negative layer close to the surface. This "double-layer" structure resembles a capacitor which quickly brings the potential down across the surface as shown in Fig. 3.4. An analogous structure also exists in heavy nuclei [48, 112] with charge $Z \gg 1/\alpha^{3/2}$.

To make the analysis more quantitative, one needs to know the specific potential profile in this region. Near the cluster surface, we can approximately use a plane solution of $\varphi(r)$, i.e., ignore the $2/r$ term on the left side of Eqs. (3.15a) and (3.15b). This kind of solution for $r \gtrsim R$ is given by Eq. (2.7) with $x = r - R \ll R$ which is the distance to the surface and the characteristic decay length $d \ll R$ is given by Eq. (3.13) which in the dimensional form is

$$d = \frac{C_7}{A^{1/4}} \left(\frac{b}{a}\right)^{1/4} \frac{a}{(n_0 a^3)^{7/12}}, \tag{3.22}$$

where $C_7 \approx 2$. By expressing n_0 in terms of Z and R, we get $d/R \propto (Z^*/Z)^{7/12} \ll 1$ at $Z \gg Z^*$.

Correspondingly, the radial electron concentration at $x \gtrsim R$ is given by

$$\begin{aligned} n(r)r^2 &= \frac{C_8}{A^{3/7}} \frac{1}{b^3} \left(\frac{b}{a}\right)^{24/7} \left(\frac{a}{x+d}\right)^{12/7} r^2 \\ &\approx \frac{C_8}{A^{3/7}} \frac{1}{b^3} \left(\frac{b}{a}\right)^{24/7} \left(\frac{a}{x+d}\right)^{12/7} R^2, \end{aligned} \tag{3.23}$$

where $r \approx R$, $C_8 \approx 1$.

Since the "double-layer" structure resembles a plane capacitor, near the surface, the potential drops practically linearly with the radius. Using Eq. (2.7), one can get $\varphi(r) \approx [1 - 8x/7d]\varphi(R)$ at $0 < x = r - R \ll d$, which gives the electric field $8\varphi(R)/7d$ inside the "double layer". At $r < R$, this electric field persists and gives $\varphi(r) \approx [1 + 8(-x)/7d]\varphi(R)$ at $0 < -x = R - r \ll d$. As r further decreases, the positive layer ends and the potential crosses over to the constant value φ_0 given by $n(\varphi_0) = n_0$ using Eq. (3.2).

According to Eq. (2.7), when $x = r - R$ is comparable to R and the plane approximation is about to lose its validity, $\varphi(r)$ is $\propto (R/a)^{-8/7}$. It is weak enough to match the low electric potential $\varphi_{out}(r) \propto (R/a)^{-8/7}$ caused by the renormalized charge $Z_n \sim Z^*$ at $r \sim R$. The plane solution then crosses over to the potential $\varphi_{out}(r) \propto Z^{*3}/r^5$ which is the asymptotic form at large distances.

A schematic plot of the potential energy $U(r) = -e\varphi(r)$ as a function of radius r is shown in Fig. 3.4 by the thin solid line (red). The corresponding radial distribution of electrons is shown in Fig. 3.6 by the thick solid line (red).

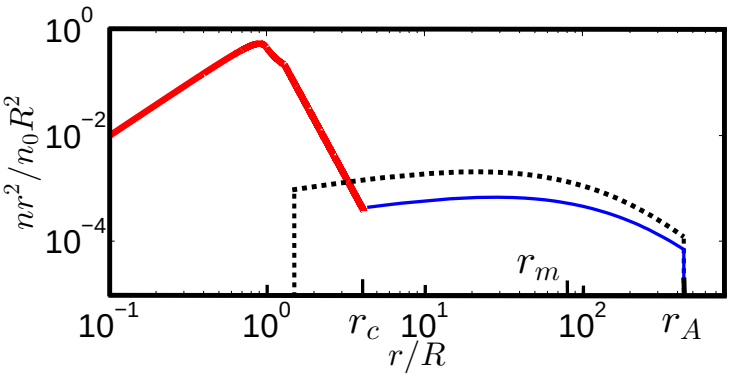

Figure 3.6: (Color online) Radial electron concentration $n(r)r^2$ as a function of radius r for the two-scale Thomas-Fermi atom formed by the super-critical cluster of donors (solid lines). The thick solid line (red) represents the inner collapsed electrons at $r < r_c$ where the dielectric response is nonlinear. The thin solid line (blue) shows the electrons belonging to the outer shell which form the standard Thomas-Fermi atom with the renormalized nucleus of charge Z^* at $r > r_c$, where the dielectric response is linear. This electron gas ends at the Bohr radius $r_A = \kappa b$ while most of them are at the radius $r_m = \kappa b/Z^{*1/3}$. For contrast, the dashed line (black) denotes the electrons forming a conventional Thomas-Fermi atom [26, 47] with a nucleus of charge Z when P_0 is infinity and there's no range with nonlinear dielectric response. The reduction of electron density in the outer shell of electrons due to the collapse is substantial. The reason this is not immediately seen from the difference of height between the dashed line (black) and the thin solid line (blue) is that we use a logarithmic scale here. n_0 is defined as $3Z/4\pi R^3$. This graph is plotted at $b = 0.35\,\mathring{A}$, $a = 3.9\,\mathring{A}$, $A = 0.9$, $R = 4.4a$, $\kappa = 20000$, $n_0 = 0.8/a^3$.

So far, we have got a $1/r^5$ potential $\varphi(r)$ and $1/r^{11/2}$ radial electron concentration $n(r)r^2$ at $r \gg R$ in both weak and strong charge renormalization cases. However, as the electron density decreases to certain extent so that the Fermi wavelength λ is comparable to the radius r, the gas is no longer degenerate and the Thomas-Fermi approach fails. Since $\lambda \simeq n(r)^{-1/3}$, we get this radius $r^* \simeq Z^* a$ at $Z \gg Z^*$. One should then return to the Schrodinger equation used for a single electron. Since the uncertainty principle estimates that the kinetic energy decays as $1/r^2$ while the potential energy is $\propto -Z^{*3}/r^5$, the potential energy is smaller than the kinetic energy in magnitude at $r > r^*$, which means electrons can not stay at radii larger than r^*. One can also find that using the Thomas-Fermi solution $\varphi_{out}(r)$, the total electron number calculated at $r > r^*$ is ~ 1, which again indicates there is no electron at $r > r^*$ considering the discreteness of electron charge. As a result, the $1/r^{11/2}$ tail of radial electron concentration will not continue to infinity but stop at radius r^*. This is a semi-classical result. Quantum mechanical analysis shows that the electron density does not go to zero right at r^* but decays exponentially after this point. Since this decay is fast and brings very small corrections to the edge of the inner electron gas, we do not consider it here.

At $\kappa = \infty$, the rest of the electrons are at the infinity so that we are dealing with a positive ion with charge Z^*. At finite but very large κ, at certain distance from the cluster, the field is so small that $\mathscr{P} > \sqrt{4\pi/\kappa A}\mathscr{P}_0$ is no longer satisfied and the linear dielectric response is recovered. Things then become quite familiar. Electrons are mainly located between $r_1 = \kappa b/Z^*$ and $r_A = \kappa b$ with the majority at radius $r_m = \kappa b/Z^{*1/3}$ as given by the Thomas-Fermi model [47]. Although quantum mechanics gives a nonzero electron density at $r < r_1$, the number of total electrons within this radius is only ~ 1 and can be ignored. So approximately, when $r_1 \gg r^*$, i.e., $\kappa \gg (Z^*)^2 \simeq (R/a)^{18/7}$, there's a spatial separation between inner collapsed electrons and outer ones that form the usual Thomas-Fermi atom with the renormalized nucleus. When κ is not so big, such separation is absent, which actually happens more often in real situations. The inner tail then connects to the outer electrons with the Thomas-Fermi approach valid all the way and the dielectric response becomes linear at $r = r_c \propto a\kappa^{1/4}Z^{*1/2}$. One should note, as long as κ is large enough to satisfy $r_m \gg R$ which gives $\kappa \gg (R/a)^{10/7}$, the majority of the outer electrons located at r_m do not intrude into the cluster or the highly screening double-layer structure near the cluster surface. The charge renormalization

process remains undisturbed and the total net charge seen by outer electrons is still Z^*. The corresponding radial electron concentration $n(r)r^2$ is shown in Fig. 3.6. At $\kappa \ll (R/a)^{10/7}$, in most of the space the dielectric response is linear. In that case, almost all electrons reside in the cluster with only some spill-out near the surface. The positive and negative charges are uniformly distributed inside the cluster as described by the Thompson "jelly" model.

3.2.2 Cylindrical Donor Clusters

In some cases, the donor clusters are more like long cylinders than spheres. Then, a cluster is described by the linear charge density ηe while its radius is still denoted as R. We use a cylindrical coordinate system with the z axis along the axis of the cylinder cluster and r as the distance from the axis. We show that when the charge density ηe is larger than certain value $\eta_c e$, electrons begin to collapse into the cluster and the charge density is weakly renormalized. When η exceeds another value $\eta^* \gg \eta_c$, the renormalization becomes so strong that the net density η_n remains $\simeq \eta^*$ regardless of the original density η. Our problem is similar to that of the charged vacuum condensate near superconducting cosmic strings [51], and is also reminiscent of the Onsager-Manning condensation in salty water [52]. For example, in salty water, the negative linear charge density of DNA is renormalized from $\simeq -4e/l_B$ to the universal net value $-e/l_B$ due to the condensation of Na^+ ions onto the DNA surface. Here $l_B = e^2/\kappa_w k_B T \simeq 7\,\mathring{A}$ where $\kappa_w = 81$ is the dielectric constant of water and T is the room temperature.

Renormalization of Linear Charge Density.— For a uniformly charged cylindrical cluster with a linear charge density ηe, similar to what we did in Sec. 3.2.1, we get $\mathscr{D}(r) = 2\eta(r)e/r$, where $\eta(r)$ is the total linear charge density enclosed in the cylinder of radius r and $\eta(r) = \eta r^2/R^2$ at $r < R$ and $\eta(r) = \eta$ at $r > R$. We then can calculate the electric field using Eqs. (2.1) and (2.3) and get the electric potential $\varphi(r)$ as:

$$\varphi(r) = \frac{A}{P_0^2}\left(\frac{\eta e}{2\pi}\right)^3 \left(\frac{3}{4}\frac{1}{R^2} - \frac{1}{4}\frac{r^4}{R^6}\right), 0 < r < R \tag{3.24a}$$

$$\varphi(r) = \frac{A}{P_0^2}\left(\frac{\eta e}{2\pi}\right)^3 \frac{1}{2r^2}, \qquad R < r \tag{3.24b}$$

with $\varphi(r = \infty)$ chosen to be 0. The corresponding potential energy $U(r) = -e\varphi(r)$ is shown in Fig. 3.8 by the thick solid line (blue). Using the Schrodinger equation and

setting the momentum $p \simeq \hbar/2r$, we find that the tightly bound states of electrons, in which electrons are strongly confined within the cluster (at $r < R$), exist only when $\eta > \eta_c$ where

$$\eta_c \approx 2\pi \left(\frac{b}{Aa}\right)^{1/3} \frac{1}{a}, \tag{3.25}$$

which, contrary to Z_c obtained in the spherical case, does not depend on R. Electrons begin to collapse into the cluster at $\eta > \eta_c$ and in the beginning they are located near the axis where the potential energy is lowest (see Fig. 3.8). With increasing η, the electron density grows and one can adopt the Thomas-Fermi description. Using Eq. (3.2) and (3.24b), one gets the electron density $n(r) \propto 1/r^3$ at $r > R$ and the total number of collapsed electron per unit length is

$$\theta = \int_0^\infty n(r) 2\pi r dr = 0.5\eta \left(\frac{\eta}{\eta^*}\right)^{7/2} \propto \eta^{9/2}, \tag{3.26}$$

where

$$\eta^* = \frac{1}{a}\left[2\pi \left(\frac{b}{Aa}\right)^{1/3}\right]^{9/7} \left(\frac{R}{a}\right)^{2/7}. \tag{3.27}$$

The net charge density $\eta_n e$ is then renormalized to

$$\eta_n = \eta - \theta = \eta\left[1 - 0.5\left(\frac{\eta}{\eta^*}\right)^{7/2}\right]. \tag{3.28}$$

At $\eta \ll \eta^*$, the renormalization of charge density is weak and η_n grows with η. At $\eta > \eta^*$, the renormalization effect becomes strong. Most of the cluster is then neutralized by electrons and the final net density η_n is much smaller than η. Following the logics similar to that in the spherical case, and by using Eq. (3.26), one can show that η_n reaches a saturation value of η^* at $\eta \gg \eta^*$. The dependence of η_n on η is shown in Fig. 3.7.

Radial Distribution of Electrons.— At $\eta \gg \eta^*$, there are lots of collapsed electrons inside the cluster where $n(r) = n_0 = \eta/\pi R^2$ and the potential energy is low. Again, there's a "double-layer" structure on the surface that provides steep growth of potential energy with r at $r = R$. Close to the cylinder surface at $0 < x = r - R \ll R$, as for the sphere, we can approximately use a plane solution of $\varphi(r)$ as given by Eq. (2.7). The expression of the characteristic decay length d is also the same as in Eq. (3.22). When $x = r - R$ is comparable to R, the plane solution crosses over to the fast decaying

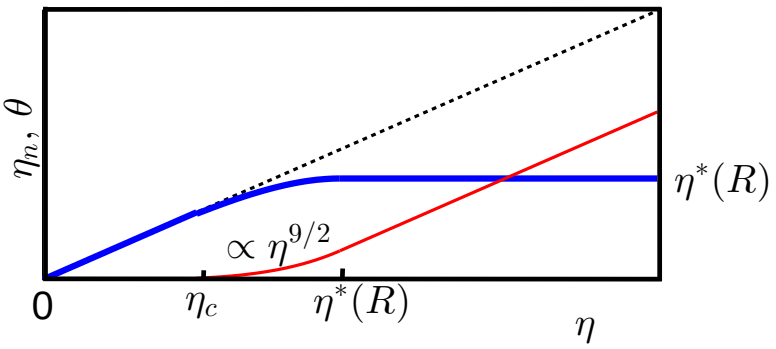

Figure 3.7: (Color online) Number of collapsed electrons per unit length θ and renormalized net linear charge density η_n as a function of the cluster linear charge density η. The thick solid line (blue) shows $\eta_n(\eta)$. The thin solid line (red) represents $\theta(\eta)$. The dashed line (black) is a guide-to-eye with $\eta_n = \eta$. $\theta(\eta) \propto \eta^{9/2}$ at $\eta_c \ll \eta \ll \eta^*$.

potential $\propto 1/r^2$ as given by Eq. (3.24b) with η replaced by $\eta_n \simeq \eta^*$. A schematic plot of the potential energy $U(r) = -e\varphi(r)$ is shown in Fig. 3.8.

This potential produces a universal tail of electron density $n(r) \sim 1/r^3$. The corresponding radial electron concentration $n(r)r$ is $\sim 1/r^2$. Since the Fermi wavelength $\lambda \simeq n(r)^{-1/3}$, we get $\lambda \sim r$, i.e., the Thomas-Fermi approach is only marginally valid. The collapsed electrons extend until the linear dielectric response is recovered and then connect to the outer electrons.

3.2.3 Finite-temperature effect in spherical donor clusters and the corresponding experimental implications

So far, we dealt with zero temperature. At a finite temperature T, the neutral cluster atom can get ionized due to the entropy gain of ionized electrons. The donor cluster atom becomes a positive ion with charge $Z_i(T)e$. Recall that the TF approach is valid at all distances until $r_A = \kappa b$. The first ionization energy of the cluster atom is then negligible ($= e^2/\kappa^2 b \simeq 10^{-7}$ eV). So the cluster atoms are always partially ionized. Our goal below is to find this ionization charge for the spherical donor clusters. Similar analyses for the cylindrical clusters can be found in Ref. [113] and are not repeated here.

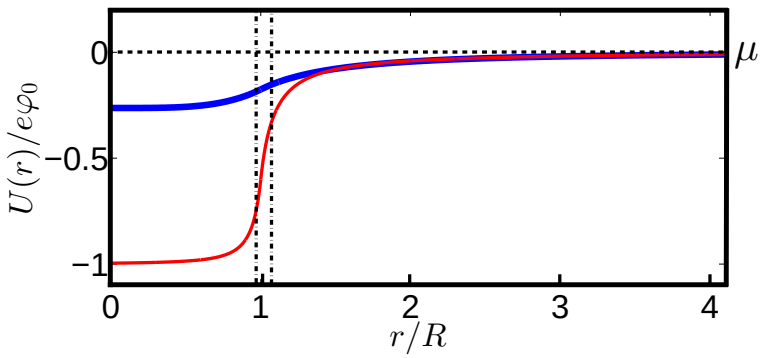

Figure 3.8: (Color online) Potential energy of electrons $U(r) = -e\varphi(r)$ caused by a cylindrical donor cluster of radius R as a function of the distance r from the cluster center. φ_0 is defined as $n(\varphi_0) = n_0$, where $n_0 = \eta/\pi R^2$, $n(r)$ is a function of $\varphi(r)$ given by Eq. (3.2). The thick solid line (blue) represents the potential profile of a cluster of charge density $\eta \lesssim \eta^*$ which is in the regime of weak renormalization of charge. The thin solid line (red) represents the potential of a cluster with $\eta \gg \eta^*$ which is in the strong renormalization regime. The two vertical dotted lines show edges of the "double-layer" structure of width $\sim d \ll R$. The horizontal dashed line (black) indicates the position of the chemical potential $\mu = 0$.

We assume that we have a small but finite three-dimensional concentration n_{cl} of spherical clusters and the charge $Z_i(T) < Z^*$, i. e., the outer electron shell is still incompletely ionized. Such a cluster can bind electrons with an ionization energy $Z_i(T)^2 e^2/\kappa^2 b$. We can find $Z_i(T)$ by equating this energy with the decrease in the free energy per electron $k_B T \ln(n_0/n)$ due to the entropy increase (the entropy increase can be derived according to § 104 of Ref. [25]), where k_B is the Boltzmann constant, $n = Z_i(T) n_{cl}$ is the concentration of ionized electrons and $n_0 = 2/\lambda^3$ with $\lambda = \sqrt{2\pi\hbar^2/m^* k_B T}$ as the DeBroglie wavelength of free electrons at temperature T. At $\kappa = 20000$, $b = 0.29\,\mathring{A}$, $m^* = 1.8 m_e$ where m_e is the electron mass and $n_{cl} = 10^{15}$ cm^{-3} (estimated from that the concentration of total donor electrons is around 10^{18} cm^{-3} and each cluster contributes ~ 300 donor electrons), we get $Z_i(T) \gtrsim Z^*$ at $T \gtrsim 8$ K with $Z^* = 100$ which is a reasonable estimate. This shows that the outer electrons are completely ionized at temperatures that are not too low. For the inner core electrons, the dielectric response is nonlinear and the attractive potential is stronger. So the

ionization energy is higher $\simeq A(Z^*e/4\pi)^3/5\mathscr{P}_0^2R^5$ for electrons at $r \simeq R$. At $R = 4a$, it is found that only at $T > 450$ K can the inner electrons be ionized by a considerable quantity (the $1/r^{15/2}$ tail is completely stripped then). So the inner electrons are robust against the thermal ionization.

Experimentally, charged clusters can be created controllably on the LAO/STO surface when the LAO layer is of subcritical thickness $\lesssim 3$ unit cell [45, 46]. A conducting atomic force microscope (AFM) tip is placed in contact with the top LAO surface and biased at certain voltage with respect to the interface, which is held at electric ground. When the voltage is positive, a locally metallic interface is produced between LAO and STO where some positive charges are accumulated in the shape of a disc. The same writing process can also create a periodic array of charged discs.

Let us first concentrate on a disc of positive charge created in this manner on the STO surface. Close to the surface and in the bulk STO, one should apply the plane solution given by Eq. (2.8). When the distance r from the disc center is large, i.e., $r \gg R$, the disc behaves like a charged sphere. Our results for a sphere are still qualitatively correct in this case.

In a periodic array of highly charged discs with period $2L$ (see Fig. 3a in Ref. [45]), the linear concentration of free electrons responsible for the conductance at a very low temperature is of the order of $n(L)L^2$, where $n(r)$ is the electron density around a spherical donor cluster given by Subsec. 3.2.1. When the overlapping parts between neighboring discs belong to the outer electron shells, the corresponding density at $r = L$ is that of a Thomas-Fermi atom with charge Z^*. In this situation, the overlapping external atmosphere forms conductive "bridges" between discs at low temperature. When T increases, however, the outer electrons are ionized and the bridges are gone. These free electrons spread out over the bulk STO. At $T \lesssim 30$ K, electrons are scattered mainly by the Coulomb potential of donors and the corresponding mobility decreases with a decreased electron velocity. For the electrons ionized into the vast region of the bulk STO, they are no longer degenerate, so their velocity becomes much smaller at relatively low temperature. This results in a much smaller mobility of the ionized electrons than those bound along the chain. Their contribution to the conductivity is thus negligible. The system becomes more resistive due to the ionization and one can observe a sharp decrease of the conductivity along the chain.

Chapter 4

Surface roughness scattering

In Chapter 2, we have discussed the importance of surface scattering where roughness is one of most important scattering mechanisms. In this chapter, we want to get the surface relaxation time of electrons close to the interface caused by surface roughness scattering. We use the approximate model where all the surface electrons are confined within a distance d from the surface and have the 3D wavenumber k_F. This is always a good description of the main body electrons of the distribution, which captures well the scaling behavior of surface mobilities. Also, in this chapter, we focus on the accumulation layers in conventional semiconductors with the linear dielectric response to connect to previous work on the surface roughness scattering. For the STO case where the dielectric response is nonlinear, the expression for the surface relaxation time is the same in terms of k_F and d. Using the new relationship between k_F, d and the total 2D electron concentration N we obtain the corresponding mobility which has already been explained in Introduction and the end of Chapter 2.

4.1 Models of surface roughness

The surface roughness is a random shift of the interface $\Delta(\vec{r})$ from $z = 0$ so that $< \Delta(\vec{r}) >= 0$, where $\vec{r} = (x, y)$ is the coordinate in $z = 0$ interface plane (see Fig. 4.1). The roughness is described by the height correlator and its Fourier transform

$$\begin{aligned} < \Delta(\vec{r})\Delta(\vec{r'}) >&=W(\vec{r} - \vec{r'}), \\ < |\Delta(q)|^2 >&=W(q). \end{aligned} \tag{4.1}$$

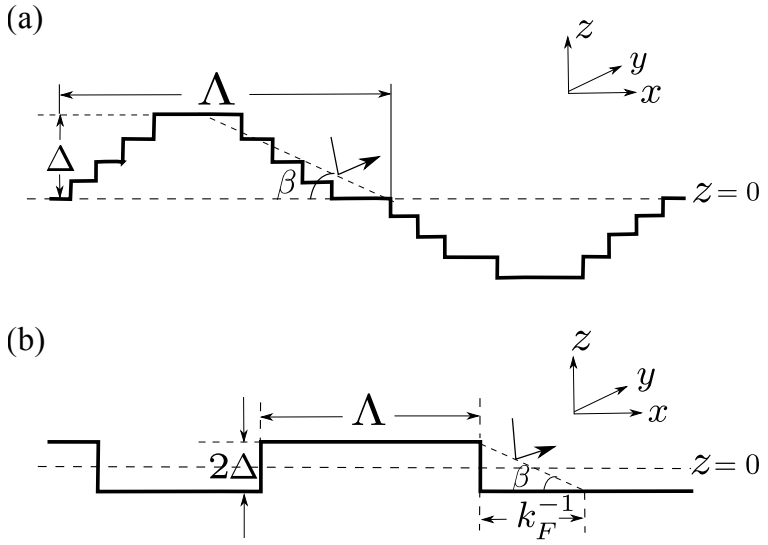

Figure 4.1: Two types of surface roughness. (a) The Gaussian type of roughness. Here the lattice discreteness can be ignored where $\Delta \gg a$ and a is the lattice constant. (b) The exponential kind of roughness. The size of the roughness is Λ and the height fluctuates as $\pm\Delta$ with respect to the average interface ($z = 0$) where $2\Delta = a$. When the electron wavelength $k_F^{-1} \gg \Lambda$, the felt height of roughness is averaged result $\Delta/\sqrt{1/k_F^2\Lambda^2} = \Delta k_F \Lambda$ on a length scale of k_F^{-1} for both types of surface roughness. At $k_F^{-1} \ll \Lambda$, the incident electron feels only a single hill/valley or island. For Gaussian roughness, the electron scatters on the slope determined by the angle $\beta \sim \Delta/\Lambda$ shown in (a). For the exponential roughness, however, the electron is scattered by the island edge which has a height Δ and an effective length k_F^{-1}, and thus the effective angle is $\beta \simeq \Delta k_F$ as shown in (b).

Two main models of roughness are used in literature. One is Gaussian

$$\begin{aligned} W(\vec{r} - \vec{r'}) =& \Delta^2 e^{-(\vec{r}-\vec{r'})^2/\Lambda^2}, \\ W(q) =& \pi\Delta^2\Lambda^2 e^{-q^2\Lambda^2/4}, \end{aligned} \tag{4.2}$$

where Λ, Δ are the characteristic size and height of the roughness, $\Delta \ll \Lambda$, d, where d is the typical width of the electron accumulation layer. This is the model widely used in earlier studies such as for the single subband mobility [30, 55, 56, 57, 58, 59, 60].

However, later experimental observations found that the spacial correlations are

more likely to follow an exponential behavior [53, 114]

$$\begin{aligned} W(\vec{r}-\vec{r'}) =& \Delta^2 e^{-\sqrt{2}|\vec{r}-\vec{r'}|/\Lambda}, \\ W(q) =& \pi\Delta^2\Lambda^2(1+q^2\Lambda^2/2)^{-3/2}. \end{aligned} \tag{4.3}$$

The important difference from the Gaussian case is that here $W(q)$ decays much slower as q^{-3} at large q. This leads to a stronger scattering at large 2D electron concentration N. One way to envision this kind of roughness is to think about randomly distributed flat islands of an additional lattice layer with typical size Λ on the top of the last complete layer of the crystal. These islands may, for example occupy half of the surface area, so that $\Delta(\vec{r}) = \pm\Delta$ appear with equal probability where $2\Delta = a$ is the lattice constant. Whenever two survey points $\vec{r}$ and $\vec{r'}$ fall within the same island, $\Delta(\vec{r})\Delta(\vec{r'})$ is Δ^2. This typically happens when points are close, i.e., $|\vec{r}-\vec{r'}| \ll \Lambda$. When one of the points misses this island $\Delta(\vec{r})\Delta(\vec{r'})$ is $-\Delta^2$. The probability of falling into different islands at $|\vec{r}-\vec{r'}| \ll \Lambda$ is $\propto |\vec{r}-\vec{r'}|/\Lambda$. So $W(\vec{r}-\vec{r'}) \sim \Delta^2(1-|\vec{r}-\vec{r'}|/\Lambda)$. Such a behavior at small distances determines the large q asymptote of the Fourier transform $W(q)$ as $\sim 1/q^3$, which is the result obtained at large q from Eq. (4.3). Our calculations of the roughness-limited mobility for accumulation layers are focused on this type of surface roughness. However, to make a connection with earlier studies[30, 55, 56, 57, 58, 59, 60], we will also calculate the mobility for the Gaussian model and compare the results of these two models.

4.2 Quasi-classical picture

Inspired by Ref. [58], in this section we start from an intuitive quasi-classical picture of the electron scattering by the surface roughness and get the scaling result shown in Fig. 1.8.

Electrons are scattered when they hit the rough "hard wall" surface. The time between two consecutive collisions of electrons with the surface is $\sim d/v_F \sim m^*d/\hbar k_F$. For each bounce, the reflection is specular with respect to the tangential plane of the hitting point and therefore adds a random angle β to the direction of the reflected momentum. Due to this angular diffusion, the total relaxation of the momentum

direction requires β^{-2} times collisions. Thus the relaxation time is

$$\tau = \frac{m^* d}{\hbar k_F \beta^2}. \tag{4.4}$$

Below we are going to investigate the deviation angle β at different values of k_F and thus find τ.

For the exponential surface roughness, one can imagine the irregularities as islands going up or down. Each island is flat on a scale Λ and drops or rises abruptly by a height Δ on the edges. An electron can be regarded as a particle only on length scales larger than the wavelength k_F^{-1}. At $\Lambda \ll k_F^{-1}$ or $1/\Lambda \gg k_F$, electrons can only feel an averaged roughness of all islands within the region of size k_F^{-1} whose number is $(k_F^{-1})^2/\Lambda^2 = 1/k_F^2\Lambda^2$. Due to the randomness of the distribution of these islands, the resulting height or depth has a magnitude $\sim \Delta/\sqrt{1/k_F^2\Lambda^2} = \Delta k_F \Lambda$. Such a height/depth on a length scale k_F^{-1} effectively results in $\beta = \Delta k_F \Lambda / k_F^{-1} = \Delta \Lambda k_F^2$. Using Eq. (4.4), we get for $k_F\Lambda \ll 1$

$$\tau \sim \frac{1/(\Delta\Lambda k_F^2)^2}{\hbar k_F/m^* d} = \frac{m^* d}{\hbar \Delta^2 \Lambda^2 k_F^5}. \tag{4.5}$$

In the opposite case at e$k_F^{-1} \ll \Lambda$, the electron hits a single island each time it bounces off the surface. However, when electrons hit the flat middle plane of the island, there is no momentum relaxation. Only when electrons happen to hit the sharp edges can they get a "scattering" reflection. Since only on a scale k_F^{-1} can electrons be seen as quasi-classical particles, the scattering edge is then estimated to be of height Δ and size k_F^{-1} which gives rise to $\beta = \Delta k_F$ (see Fig. 4.1b). The probability to hit one such edge is proportional to its area fraction $k_F^{-1}\Lambda/\Lambda^2 = 1/k_F\Lambda$. This gives

$$\tau \sim \frac{1/(\Delta k_F)^2}{1/k_F\Lambda} \frac{m^* d}{\hbar k_F} = \frac{m^* d \Lambda}{\hbar \Delta^2 k_F^2}. \tag{4.6}$$

Since in conventional semiconductors with the linear dielectric response $d = d_1 \sim a_B/(Na_B^2)^{1/5}$ as shown in Eq. (2.42) where N is the total 2D electron concentration, we then can get the corresponding expression of k_F in terms of N for the main body electrons of the accumulation layer as $k_F \sim (N/d)^{1/3} \sim (Na_B^2)^{2/5}/a_B$. Therefore, the

(surface) mobility is

$$\mu \sim \frac{e}{h}\frac{1}{\Delta^2} \times \begin{cases} \dfrac{a_B^{8/5}}{\Lambda^2 N^{11/5}}, & N a_B^2 \ll (a_B/\Lambda)^{5/2}, \\ \dfrac{a_B \Lambda}{N}\ , & N a_B^2 \gg (a_B/\Lambda)^{5/2}, \end{cases} \tag{4.7}$$

and the 2D conductivity $\sigma = Ne\mu$ as shown in Fig. 1.8, where $k_F\Lambda \sim 1$ at $Na_B^2 \sim (a_B/\Lambda)^{5/2}$ (here the conductivity converges to the surface value and thus is determined by the surface mobility μ). When $\Lambda > a_B$, in the 3D regime where $Na_B^2 > 1$ there is no range of $k_F\Lambda \ll 1$ and the mobility always decreases as $\propto 1/N$. One should note that the 2D conductivity saturation $\sigma/(2e^2/h) \sim \Lambda a_B/\Delta^2$ at large concentration N is usually much larger than unity as Λ, $a_B \gg \Delta$ and implies that the accumulation layer remains metallic at large concentrations.

4.3 Single subband case

In previous section, we have employed a quasi-classical perspective to understand the electron scattering off the surface roughness. Now we turn to the more formal quantum mechanical approach. Let us start from the single subband case where the scattering occurs within the same subband. The scattering rate $1/\tau$ of an electron at the Fermi level with the wave vector $\vec{k'}$ can be found according to Fermi's golden rule:

$$\frac{1}{\tau} = \frac{2\pi}{\hbar}\int \frac{d^2\vec{k}}{(2\pi)^2}\frac{|U(q)|^2}{\epsilon(q)^2}\delta(\varepsilon - \varepsilon_F)(1-\cos\theta') \tag{4.8}$$

where $\varepsilon = \hbar^2k^2/2m^*$, $\varepsilon_F = \hbar^2k'^2/2m^* = \hbar^2k_F^2/2m^*$ are the final and initial (Fermi level) energies of an electron, $\vec{k}$ is the final electron momentum, k_F is the Fermi wavenumber, θ' is the angle between initial and final electron momenta and $q = 2k_F\sin(\theta'/2)$ is the magnitude of the transferred momentum $\vec{q} = \vec{k} - \vec{k'}$. All the momenta here are in the x-y plane. Due to the electronic screening inside a single subband, the Fourier transform of the scattering potential $U(q)$ is reduced by the dielectric function $\epsilon(q)$ [57]

$$\epsilon(q) \simeq 1 + 2/a_B q. \tag{4.9}$$

Let us first derive the scattering potential resulting from the surface roughness. We know that electrons are confined near the interface and thus have a quantization kinetic energy

$E_z = \hbar^2 k_z^2/2m^*$ where k_z is approximately a multiple of π/d (for the first subband, $k_z \simeq \pi/d$). Due to the surface roughness, the confinement width d fluctuates by $\Delta(\vec{r})$ at position r. The kinetic energy then varies by $(\partial E_z/\partial d)\Delta(\vec{r}) \sim E_z\Delta(\vec{r})/d$. These fluctuations of the quantization kinetic energy act as a fluctuating potential $U(\vec{r})$ for the 2-dimensional motion of confined electrons. Its scattering matrix element for 2D Bloch states $U(q)$ within a given subband then satisfies

$$|U(q)|^2 = \left(\frac{E_z}{d}\right)^2 W(q). \tag{4.10}$$

As a result we get:

$$\frac{1}{\tau} \sim \frac{\hbar}{m^*}\frac{k_z^4}{d^2}\int d\theta' \frac{W(q)}{\epsilon(q)^2}(1-\cos\theta'). \tag{4.11}$$

At $k_F\Lambda \ll 1$, according to Eqs. (4.2) and (4.3), two models of roughness give the same $W(q) \sim \Delta^2\Lambda^2$. For the one subband case, $k_F a_B \simeq 1$ and $\epsilon(q) \simeq 1$. This gives the scattering rate as

$$\frac{1}{\tau} \sim \frac{\hbar}{m^*}\frac{k_z^4\Delta^2\Lambda^2}{d^2}. \tag{4.12}$$

As $k_z \sim 1/d$, the mobility is then

$$\mu \sim \frac{e}{\hbar}\frac{d^6}{\Delta^2\Lambda^2}. \tag{4.13}$$

Since in the single subband case $Na_B^2 \leq 1$, the condition of validity of Eq. (4.13) $k_F\Lambda \ll 1$ is fulfilled for the roughness with $\Lambda < a_B$. The case $\Lambda < a_B$ was studied for silicon inversion layers in Ref. [55] and discussed in Introduction above. For the 2D inversion layers, the width d is determined by the applied electric field as $d \propto \mathscr{E}^{-1/3}$ and one gets [55, 30, 58] $\mu \propto 1/\mathscr{E}^2$. As the electron concentration increases, the interfacial electric field $\mathscr{E} \propto N$ and mobility $\mu \propto 1/N^2$. Such a dependence was obtained in Ref. [55] and used in Ref. [70] for extrapolation to the multisubband case as shown in Fig. 1.8. Note that for the 2D quantum wells, the width d of the electron gas is the same as the well width so that Eq. (4.13) agrees with the well known result of Ref. [59].

However, if $\Lambda > a_B$, for the single subband case, there is also a range of concentrations that satisfies $k_F\Lambda \gg 1$. The results of two roughness models are different. For the Gaussian case, the typical q is $\sim 1/\Lambda$ and the typical θ' is $\sim q/k_F \sim 1/k_F\Lambda$, $W(q) \sim \Delta^2\Lambda^2$, $\epsilon(q) \sim 1 + \Lambda/a_B \sim \Lambda/a_B$. The scattering rate is then

$$\frac{1}{\tau} \sim \frac{\hbar}{m^*}\frac{k_z^4\Delta^2 a_B^2}{d^2 k_F^3\Lambda^3}. \tag{4.14}$$

Putting $k_z \sim 1/d$ for the single subband case, we get the mobility as

$$\mu \sim \frac{e}{\hbar}\frac{d^6\Lambda^3 k_F^3}{\Delta^2 a_B^2}, \tag{4.15}$$

which can also be obtained from results in Refs. [60, 58].

For the exponential case, $W(q)$ decays in a much milder way as $\propto 1/q^3$ at large q. This leads to the large angle scattering. Indeed, let us consider the contribution to the integral in Eq. (4.11) from the small angles $\theta' \sim (k_F\Lambda)^{-1}$ and large angles $\theta' \sim 1$. In the first case, $W(q \sim 1/\Lambda) \sim \Delta^2\Lambda^2$, $\epsilon(q) \sim \Lambda/a_B$ and

$$\int_0^{(k_F\Lambda)^{-1}} d\theta'(1-\cos\theta') \simeq \theta'^3 \simeq \frac{1}{(k_F\Lambda)^3}.$$

As a result the contribution from the small angles to the scattering rate is the same as Eq. (4.14). For the large angles $W(q \sim k_F) \simeq \Delta^2\Lambda^2\,(k_F\Lambda)^{-3}$ is $(k_F\Lambda)^3$ times smaller than that of the small-angle scattering, $\epsilon(q) \simeq 1$ and the integral over the angle is

$$\int\limits_{(k_F\Lambda)^{-1}}^{\pi} d\theta'(1-\cos\theta') \sim 1.$$

The angle integral is $(k_F\Lambda)^3$ times larger than that from the small angles, and the scattering rate is then

$$\frac{1}{\tau} \sim \frac{\hbar}{m^*}\frac{k_z^4\Delta^2}{d^2 k_F^3\Lambda}, \tag{4.16}$$

which due to the absence of screening is $(\Lambda/a_B)^2$ times larger than that from the small-angle scattering. In this sense, the large-angle scattering is more effective and always gives the mobility as

$$\mu \sim \frac{e}{\hbar}\frac{d^6\Lambda k_F^3}{\Delta^2}. \tag{4.17}$$

The dominance of the large-angle scattering is a unique feature of the exponential roughness.

4.4 Intersubband scattering in multisubband accumulation layers

In Sec. 4.3 we have calculated the mobility limited by the surface roughness scattering of a single subband. We not only have recovered the results for the Gaussian type of

roughness obtained by previous studies but also have got the results for the relatively unexplored exponential roughness. For multisubband accumulation layers, the situation is different from the single subband case. First, k_z is not $\sim 1/d$ but typically is $\sim k_F$, where $k_F = (N/d)^{1/3}$ is the 3D Fermi wavenumber of the electron gas. Second, though the screening now is still two-dimensional (One could worry about the use of 2D screening for the 3D accumulation layer with width d. Indeed, it is known that in a metallic film with width d at the distance $q^{-1} \gg d$ the screening is two-dimensional, while at $q^{-1} \ll d$ it becomes three-dimensional. In our case, the 3D screening radius inside the layer is $r_D = a_B/(na_B^3)^{1/6} \sim a_B/(Na_B^2)^{1/5} \sim d$ where $n = N/d$ is the 3D electron concentration. Thus, for $q^{-1} < d$ the 3D dielectric function is ~ 1. Therefore, the 3D screening may be ignored.), the screening radius is d instead of a_B so that $\epsilon(q) \simeq 1+1/dq$ due to collective screening of multiple subbands (The 2D screening radius r_2 here is not a_B but d because when deriving $r_2 \propto d(e\varphi)/dN$ where $e\varphi$ characterizes the electron chemical potential for each subband, the total 2D concentration N is the electron concentration within each subband times the number of subbands $k_F d$. Therefore, the 2D screening radius is reduced from a_B to $a_B/k_F d \simeq a_B/(Na_B^2)^{1/5} \sim d$.). Last, in addition to the intrasubband scattering, there is also intersubband scattering.

Typically, the intersubband scattering rate is of the same order of the intrasubband scattering as will be shown in Sec. 4.5. Therefore, approximately, the final scattering rate is the product of the typical intrasubband scattering rate and the total number of subbands which the initial electron can be scattered into. It is easy to check that the typical transferred momentum in the z-direction is of the same order as the typical transferred momentum q in the x-y plane. At $1/\Lambda \gg k_F$ where $q \sim k_F$, all subbands "communicate" with each other and the total number is $k_F d$. Multiplying by $k_F d$ the intrasubband result Eq. (4.12) with $k_z \sim k_F$, we arrive at the final scattering rate given by Eq. (4.5). This is a universal result for both Gaussian and exponential models. At $1/\Lambda \ll k_F$, for the exponential roughness, the typical transferred momentum is $q \sim 1/\Lambda$ for the small-angle scattering and $q \sim k_F$ for the large-angle one. So for the former, the number of subbands involved in the scattering process is $\sim d/\Lambda$, much smaller than the number $k_F d$ for the latter. Considering also its immunity to screening as $k_F d \gg 1$, the large-angle scattering mechanism absolutely dominates. Using the intrasubband scattering rate as given by Eq. (4.16) and $k_z \sim k_F$, we arrive at the total scattering

rate at $k_F\Lambda \gg 1$ for the exponential roughness given by Eq. (4.6). Thereby, we get the same expressions for the mobility as in Eq. (4.7). The corresponding 2D conductivity at large N saturates as $\sigma/(2e^2/h) \sim \Lambda a_B/\Delta^2$ (see Fig. 1.8), which means that there is no re-entrant metal-insulator transition. In Sec. 4.5, we do more careful estimation of the numerical coefficient in front of $\Lambda a_B/\Delta^2$ and get that it is close to 1.

Compared to the simple result in the exponential case, the mobility for the Gaussian roughness is more complicated. At $k_F^{-1} \ll \Lambda < d$, the intrasubband scattering is unscreened for the Gaussian case and the rate is the same as Eq. (4.16). The typical momentum transfer is $q \sim 1/\Lambda$, so only a few subbands the number of which is $\sim q/d^{-1} = d/\Lambda$ can participate in the intersubband scattering. The total scattering rate is then the result in Eq. (4.16) times d/Λ. At even larger $\Lambda \gg d \gg k_F^{-1}$, the typical momentum transferred $1/\Lambda$ is smaller than the z-direction momentum quantization $1/d$. Therefore no intersubband scattering is possible. This situation resembles the single subband case and is natural since when $d \ll \Lambda$ we actually are dealing with a 2D system. At $\Lambda \gg d$, the screening of the potential adds the factor $(d/a_B)^2$ to the total scattering rate given by Eq. (4.14) as the screening radius now is d instead of a_B. The result is summarized as follows

$$\frac{1}{\tau} \sim \begin{cases} \dfrac{\hbar k_F \Delta^2}{m^* d \Lambda^2}, & k_F^{-1} \ll \Lambda \ll d\,, \qquad (4.18) \\ \dfrac{\hbar k_F \Delta^2}{m^* \Lambda^3}, & d \ll \Lambda\,. \qquad (4.19) \end{cases}$$

$k_F^{-1} = \Lambda$ is reached at $N a_B^2 \sim (a_B/\Lambda)^{5/2}$ and $d = \Lambda$ is achieved at $N a_B^2 \sim (a_B/\Lambda)^5$. By expressing k_F and d in terms of N, one can then get the mobility as a function of the 2D electron concentration. The corresponding results together with that for the exponential case are listed in Table. 4.1.

The obtained $\mu(N)$ dependence is presented in Fig. 4.2. For the exponential roughness, the corresponding 2D conductivity σ is shown in Fig. 1.8. The smallest conductivity for the exponential case is larger than $2e^2/h$ as mentioned above. For the Gaussian model, the smallest $\sigma/(2e^2/h)$ is also $\sim \Lambda a_B/\Delta^2$. Since in reality, $\Lambda > \Delta$, we get $\sigma/(2e^2/h) \gg 1$. So, the smallest conductivity for the Gaussian roughness is also always above the critical value and no re-entrant metal-insulator transition will happen in realistic situations.

Table 4.1: Mobility μ in units of $(e/\hbar)\left(\Lambda^4/\Delta^2\right)$ as a function of the 2D electron concentration N at different values of Λ for two types of surface roughness, the Gaussian model (G) and the exponential one (E). Since the Fermi wavenumber $k_F \simeq (N/d)^{1/3}$, and the width of the 2D electron gas $d = d_1 \sim a_B/(Na_B^2)^{1/5}$ is the decay length for the linear dielectric response case, we get $k_F^{-1} = \Lambda$ at $Na_B^2 \sim (a_B/\Lambda)^{5/2}$ and $\Lambda = d$ at $Na_B^2 \sim (a_B/\Lambda)^5$.

	$\Lambda < k_F^{-1}$	$k_F^{-1} < \Lambda < d$	$d < \Lambda$
G	$(a_B/\Lambda)^6/(Na_B^2)^{11/5}$	$(a_B/\Lambda)^2/(Na_B^2)^{3/5}$	$(a_B/\Lambda)/(Na_B^2)^{2/5}$
E	$(a_B/\Lambda)^6/(Na_B^2)^{11/5}$	$(a_B/\Lambda)^3/(Na_B^2)$	$(a_B/\Lambda)^3/(Na_B^2)$

In Sec. 4.2, we gave a quasi-classical explanation of the mobility limited by the exponential surface roughness. Inspired by Ref. [58], we can interpret the Gaussian roughness results quasi-classically as well. Below we again start from Eq. (4.4) and find β for the Gaussian roughness in different situations. At $k_F\Lambda \ll 1$, the roughness relief is averaged over the electron wavelength and the resulting relaxation time is the same as in the exponential case given by Eq. (4.5). At $k_F^{-1} \ll \Lambda \ll d$, the wavelength k_F^{-1} is smaller than the size of the roughness hill. The electron then collides with a single hill (valley) each time it hits the surface and the deviation angle β is the slope of each single hill (valley) $\sim \Delta/\Lambda$ (see Fig. 4.1a). The relaxation time is given by Eq. (4.18). At $d \ll \Lambda$, the electronic screening changes the scattering potential by a factor d/Λ, which can effectively be regarded as reducing the roughness height from Δ to $\Delta d/\Lambda$. The size of each single hill is so large that the electron can hit the same hill consecutively for several times during which it has traveled back and forth for $\sim \Lambda/d$ times within the accumulation layer. Since these consecutive hits are on the same slope, the scattered angle is the same and β accumulates, in contrast with uncorrelated random collisions on different hills (valleys). After the electron finishes colliding with the same slope, the accumulated angle is $(\Delta d/\Lambda^2)(\Lambda/d) = (\Delta/\Lambda) \ll 1$ and the time of such a series of collisions is $\sim (d/k_F)(\Lambda/d) = \Lambda/k_F$. The resulting relaxation time is then given by Eq. (4.19). Thus we obtained quasi-classically the same scaling behavior of the mobility limited by the Gaussian roughness as by the quantum-mechanical approach.

In this chapter, we have studied the surface-roughness limited mobility in inversion

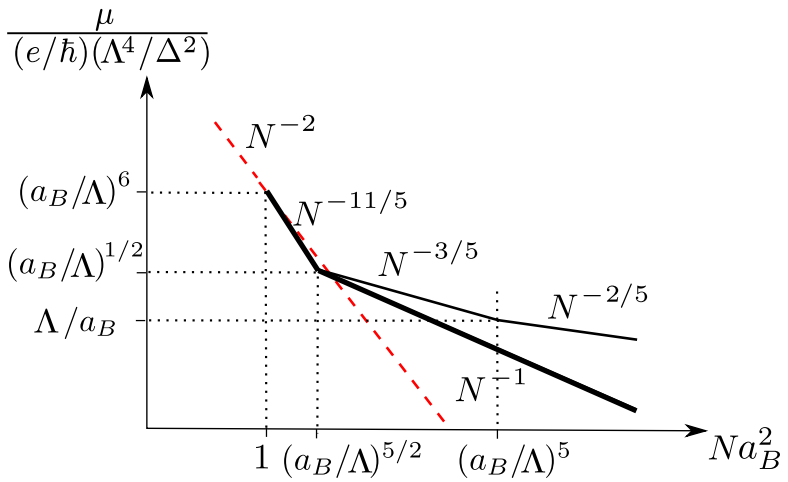

Figure 4.2: (Color online) The scaling behavior of the mobility μ in units of $(e/\hbar)\left(\Lambda^4/\Delta^2\right)$ as a function of the scaled electron concentration Na_B^2 plotted at $\Lambda < a_B$ in a double logarithmic scale. The thick solid line (black) denotes the mobility of the accumulation layer for the exponential roughness. The thin solid line (black) represents the mobility for the Gaussian roughness which also decreases. Here only powers of the N dependence are shown while the complete scaling formulae are presented in Table. 4.1. The thin dashed line (red) represents the $1/N^2$ dependence derived for a single subband [55] and its conjectured extrapolation [70] to larger concentrations.

and multisubband accumulation layers as a function of the 2D electron concentration N for two models of the surface roughness both quantum-mechanically and quasi-classically. For the more realistic exponential roughness, the mobility decreases as $\propto 1/N$ at large N and results in a 2D conductivity saturation as $\sigma/(2e^2/h) \simeq \Lambda a_B/\Delta^2 \gg 1$ since the characteristic roughness size Λ and the effective Bohr radius a_B are larger than the characteristic roughness height $\Delta \simeq a/2$ where a is the lattice constant. For the Gaussian roughness which was widely used in earlier studies, the minimum conductivity is found to be larger than the critical value as well. One should note that the considerations here have not included the contribution from the tail electrons, which makes σ larger in reality even for the linear dielectric response case due to their larger distances from the surface and thus larger relaxation times [115]. So there is no reason to expect the re-entrant metal-insulator transition [70] at large concentrations. Indeed, decent conductivities were observed in large concentration accumulation layers in Refs.

[71, 64, 65, 62]. As explained in Introduction, there is no reentrant metal-insulator transition in STO accumulation layers, either, where the dielectric response is nonlinear, for experimentally achievable large 2D electron concentrations N.

4.5 Numerical coefficients in conductivity dependence of concentration for the exponential model

Eq. (2.41) shows that about 90% of electrons are located within a distance $d_1/2 = d/2$ from the interface. So it is a good approximation to assume that electrons inside the accumulation layer are confined within a width $d' = d/2$. Then, the electron wave function of each subband is

$$\xi(r, z) \simeq \sqrt{\frac{2}{d'}} \exp(i\vec{k_r} \cdot \vec{r}) \sin(k_z z) \tag{4.20}$$

where $\vec{k_r}$, $k_z = m\pi/d'$ with m being a positive integer are respectively the x-y plane and z-direction momenta of electrons in this subband and different subbands correspond to different values of k_z. Therefore, similar to that in Ref. [55], the matrix element $U(q)$ satisfies

$$< |U|^2 >= \frac{8}{d'} \varepsilon_F^2 \left(\frac{k_z' k_z}{k_F^2} \right)^2 W(q) \tag{4.21}$$

where an isotropic mass spectrum is assumed, k_z', k_z are the initial and final z-components of the electron wavevector, $q = |\vec{q}|$ and $\vec{q}$ is the momentum transferred in the x-y plane.

Since $|U|^2$ is isotropic only with respect to the 2D momentum $\vec{q}$ in the x-y plane instead of the total 3D transferred momentum, we use the more general expression for the scattering rate as can be obtained from Ref. [116]

$$\frac{1}{\tau} = \frac{2\pi}{\hbar} \int \frac{d^3\vec{k}}{(2\pi)^3} \frac{|U|^2}{\epsilon(q)^2} \delta(\varepsilon - \varepsilon_F) \left(1 - \frac{k_r \cos\phi}{k_r'} \right), \tag{4.22}$$

where $k_r = |\vec{k_r}|$, $k_r' = |\vec{k_r'}|$, and $\vec{k_r}$, $\vec{k_r'}$ are the x-y components of the final and initial momenta $\vec{k}$ and $\vec{k'}$, ϕ is the angle between $\vec{k_r}$ and $\vec{k_r'}$. (Here we assume a constant relaxation time for different subbands, which is a good approximation for electrons located within the distance d'.)

At $k_F\Lambda \ll 1$, for both models of roughness, $W(q) = \pi\Delta^2\Lambda^2$, $\epsilon(q) \simeq 1$. So

$$\begin{aligned}\frac{1}{\tau} &= \frac{2}{\pi\hbar}\frac{\varepsilon_F^2\Delta^2\Lambda^2}{d'}\int k_r dk_r d\phi dk_z \left(\frac{k_z' k_z}{k_F^2}\right)^2 \\ &\quad \left(1-\frac{k_r\cos\phi}{k_r'}\right)\delta\left[\frac{\hbar^2 k_F^2}{2m^*} - \frac{\hbar^2(k_z^2+k_r^2)}{2m^*}\right] \\ &= \frac{2\varepsilon_F\Delta^2\Lambda^2 k_F^3}{\hbar d'}\int d(\cos\theta)\,(\cos\theta\cos\theta_0)^2\end{aligned} \tag{4.23}$$

where $\cos\theta = k_z/k_F$, $\cos\theta_0 = k_z'/k_F$. One should note that this scattering rate is for one specific direction of k'. To get the averaged result, one should average over all θ_0 and arrive at

$$\frac{1}{\tau} \simeq \frac{0.2\varepsilon_F\Delta^2\Lambda^2 k_F^3}{\hbar d'}. \tag{4.24}$$

At $k_F\Lambda \gg 1$, for the exponential case, again we have $\epsilon(q) \simeq 1$. By using Eq. (4.3), we get

$$\begin{aligned}\frac{1}{\tau} =& \frac{2}{\pi\hbar}\frac{\varepsilon_F^2\Delta^2\Lambda^2}{d'}\int k_r dk_r d\phi dk_z d(k_z'/k_F)\left(\frac{k_z' k_z}{k_F^2}\right)^2 \\ & \left\{1+\left[k_r^2+(k_r')^2-2k_r k_r'\cos\phi\right]\Lambda^2/2\right\}^{-3/2} \\ & \left(1-\frac{k_r\cos\phi}{k_r'}\right)\delta\left[\frac{\hbar^2 k_F^2}{2m^*} - \frac{\hbar^2(k_z^2+k_r^2)}{2m^*}\right] \\ \simeq& \frac{1.5\varepsilon_F\Delta^2}{\hbar d'\Lambda},\end{aligned} \tag{4.25}$$

which matches Eq. (4.24) at $k_F\Lambda \simeq 2$. Substituting $k_F = (3\pi^2 N/d')^{1/3}$ into Eqs. (4.24) and (4.25), where $d' = d/2$ and d is given by Eq. (2.42), we obtain numerical coefficients for $\sigma(N)$ and get the corresponding saturation value $\sigma/(2e^2/h) \simeq 0.6\Lambda a_B/\Delta^2$ at the point $Na_B^2 \simeq 0.4(a_B/\Lambda)^{5/2}$.

Chapter 5

Electron transport in nanocrystal films

This chapter is organized as follows. In Sec. 5.1, we dwell upon the main energies of a single NC, i.e., the quantization energy gap Δ separating consecutive degenerate shells of the electron spectrum and the charging energy E_c of a NC. In Sec. 5.2 we start from very large ratios of Δ/E_c where the dispersion of NC diameters dominates over the Coulomb disorder. We use values of $t(n,\rho)$ calculated later in Sec. 5.5 to find $\xi(n)$ and n_c. For the case of relatively large diameter dispersion and very small ρ at large n, the localization length $\xi(n)$ follows Eq. (1.7) and n_c is given by Eq. (1.6). We also study the case of a very weak diameter dispersion and arrive at the blinking metal (BM) phase. In Sec. 5.3 we study the charging of NCs and the resulting Coulomb disorder and get $\xi(n)$ for any Δ/E_c. We show that at $\Delta/E_c < 5$ the Coulomb disorder eliminates the BM phase and extends the range of validity of Eq. (1.7). In Sec. 5.4 we discuss examples of widely used semiconductor CdSe, InAs and ZnO NCs. In Sec. 5.5 we calculate the tunneling matrix element $t(n,\rho)$ for NCs touching by contact facets (see Fig. 1.9b). In Sec. 5.6, we study the case when NCs touch each other away from prominent facets or are separated by short ligands and derive the corresponding expressions for ξ. In Sec. 5.7 we deal with large NCs where the random electric field of donors split and mix degenerate shell levels so that semiconductor NCs acquire random spectra similar to that of metallic granules.

5.1 NC electronic spectrum and charging energy

We assume that close-to-spherical NCs have diameter d and touch each other by facets with radius ρ. At small enough ρ electrons are localized inside NCs. We suppose that the electron wave function is close to zero at the NC surface, due to the large confining potential barrier created by the insulator matrix surrounding the NC. Under these conditions, electrons occupy states with different radial and angular momentum quantum numbers, i.e., (n, l)-shells, each being degenerate with respect to the azimuthal quantum number $m = -l, \ldots, l$ where the polar axis (z axis) is defined in the direction of electron tunneling connecting centers of two neighboring NCs (we talk more about this in Sec. 5.5). As we explained in Introduction we are interested in NCs with the average electron number $N \gg 1$. Therefore several (n, l)-shells are occupied. The quantum energy gap between two consecutive (n, l)-shells typically is

$$\Delta \simeq \frac{20\hbar^2}{m^* d^2} \tag{5.1}$$

where m^* is the effective electron mass inside NCs.

Also, when the quantum numbers are large, Bohr's correspondence principle allows us to consider quasiclassically the average density of states of electrons and introduce the Fermi wave number k_F

$$k_F = \left(3\pi^2\right)^{1/3} n^{1/3}. \tag{5.2}$$

Here $n = 6N/\pi d^3$ is the density of electrons in a NC. Below, k_F serves as a measure of the concentration n.

The kinetic energy of electrons is only a part of the total energy of the NC. One should add to it the total Coulomb interaction energy of all electrons and donors. In general, calculating the total Coulomb energy (self-energy) of the system is a difficult problem because of the random position of donors. For our case, however, a significant simplification is available because the semiconductor dielectric constant ε is typically much larger than the dielectric constant ε_m of the medium in which the NC is embedded. This allows us to ignore in the first approximation the energy dependence on positions of donors and electrons and instead concentrate on only the dependence on the total charge Qe of the NC.

The energy of a NC with charge Qe surrounded by neutral NCs (the self-energy) is equal to Q^2E_c, where the charging energy is

$$E_c = \frac{e^2}{\varepsilon_f d} \, . \tag{5.3}$$

For non-touching NCs where the volume fraction of semiconductor NCs is $f \leq 0.52$, one can use the Maxwell-Garnet formula [117]

$$\varepsilon_f = \varepsilon_m \frac{\varepsilon + 2\varepsilon_m + 2f(\varepsilon - \varepsilon_m)}{\varepsilon + 2\varepsilon_m - f(\varepsilon - \varepsilon_m)} \tag{5.4}$$

to calculate the effective dielectric constant ε_f. This gives $\varepsilon_f \simeq 3$ at $f = 0.52$ corresponding to the very moment of NC touching (we take $\varepsilon_m = 1$, $\varepsilon = 10$ as in the case of CdSe NCs). For these ε_m and ε, the effective dielectric constant ε_f was calculated numerically for all range of f [118] including $f > 0.52$ obtained for faceted NCs touching by facets. One can check [119] that Eq. (5.4) works well even for f as large as 0.7. This means that for NCs touching by small facets or separated by short ligands, $\varepsilon/\varepsilon_f \simeq 3$ is a good estimate for CdSe and other semiconductors with $\varepsilon \lesssim 15$ that we are dealing with. For semiconductors with much larger ε one may use results of Ref. [119].

The ratio Δ/E_c is an important parameter of our theory. In n-type semiconductors we address here, for NCs with $d = 5$ nm, Δ/E_c =2, 3, 5, 27 for Si, ZnO, CdSe, and InAs, respectively.

5.2 Localization length and IMT determined by dispersion of NC diameters

There are two important sources of disorder for electrons in a NC film. The first one is the variation of NC diameters. Since the energy gap $\Delta \propto 1/d^2$, each energy level gets a shift $\alpha\Delta$, where $\alpha = 2\delta d/d$ and δd is the variation of the diameter d (experimentally, $\delta d/d$ is as large as $5 - 15\%$ [120, 86] so $\alpha = 0.1 - 0.3$). The second source of disorder is the fluctuations of the donor number in a NC, which result in the charging of NCs and subsequent random potentials. We study this phenomenon in Sec. 5.3. In this section we deal with the case of large enough Δ/E_c when charging can be ignored.

The dispersion of NC diameters creates the energy shift of the electron levels close to the Fermi level

$$\gamma_1 = N^{2/3}\alpha\Delta, \tag{5.5}$$

where $N^{2/3}$ gives the number of filled shells. When N is small, $\gamma_1 \ll \Delta$. The energy levels of NCs are then quite aligned and the density of states has periodically alternating maxima and minima (see Fig. 5.1). In this case, the transport mechanism depends on the position of the Fermi level E_F or in other words on the average electron number N [82, 88, 121]. When the Fermi level is in the middle of each degenerate shell, i.e., the local density of states is very large, Coulomb correlations "dig" the Coulomb gap in this density of states [87], which in turn leads to low-temperature ES conductivity law Eq. (1.4). When the Fermi level is close to the middle of the gap Δ where a small density of states may be present due to overlapping tails of neighboring shells, the Coulomb effects are not important since the density of states is already very small. Such a constant density of states leads to the Mott variable range hopping [82, 121].

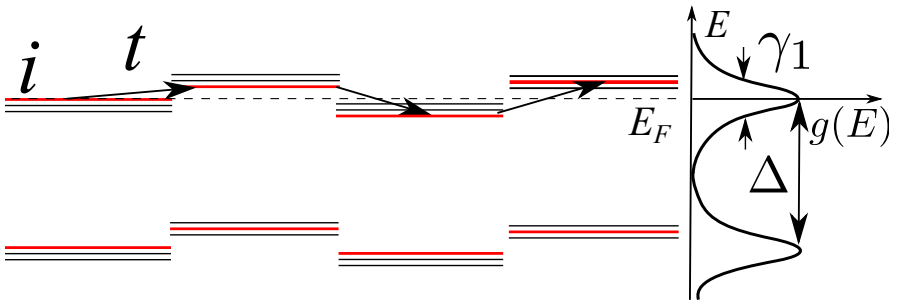

Figure 5.1: Energy spectrum of the linear chain of touching spherical NCs at small N in the vicinity of the Fermi level E_F. The degenerate electron levels are aligned with small energy shifts created by the NC diameter variations. The density of states $g(E)$ as a function of the energy E has periodic maxima separated by the energy gap Δ. Peaks of the density of states have width γ_1. The electron tunnels with the tunneling matrix element t from the initial NC i through the $m = 0$ levels (red) in the shell closest to the Fermi level in each intermediate NC. Virtually visited levels are shown by arrows. The dashed line represents the Fermi level.

However, for both ES and Mott variable range hopping, one should use the concept

of the localization length which determines the exponential decay of the electron wave function with the distance x from the NC where the localized electron resides in. The localization length ξ is determined by the co-tunneling between two distant NCs with energies close to the Fermi level [122, 123, 121, 124]. In the co-tunneling process, an electron tunnels between neighboring NCs of the chain of M intermediate NCs connecting the initial and final NCs. If after the tunneling all intermediate NCs remain in the ground state, the co-tunneling process is called elastic. An intermediate NC can also alternatively acquire an electron-hole excitation. Such a process is called inelastic. At low temperatures the elastic process dominates.

We show in Sec. 5.5 that in the chain of NCs extended along the z direction, inside each intermediate NC only the $m = 0$ state in the highly degenerate (n, l)-shell contributes to the tunneling process with a dominant matrix element t. Thus, along the chain of co-tunneling, there is only one possible series of intermediate energy states closest to the energy of the tunneling electron and no summation over different states of a given shell is needed for calculating the total amplitude. We can say that we deal with non-degenerate levels (red as shown in Figs. 1.10, 5.1 and 5.3) with the energy spacing Δ. This allows us to write estimates for the tunneling amplitude as $\propto (t/\delta E)^M \simeq e^{-x/\xi}$ where $M = x/d$ is the number of intermediate NCs in the tunneling path and ξ is the localization length

$$\xi \approx \frac{d}{\ln(\delta E/t)}. \tag{5.6}$$

Here δE is the energy difference between the tunneling electron and the state in the intermediate NC. Eq. (5.6) is valid when $\ln(\delta E/t) > 1$ or $\xi < d$ and the film is far from the critical vicinity of the IMT.

So once the matrix element t is known, we can get the localization length. For different types of contacts between NCs, the value of t is different. The largest ξ is obtained in the case when NCs touch by facets of finite radius ρ. The corresponding tunneling matrix is derived in Sec. 5.5 as

$$t \simeq \frac{9\hbar^2 n\rho^3}{m^* d^2}. \tag{5.7}$$

The energy difference δE oscillates with the density of states, which is followed by the oscillation of the localization length (see Fig. 5.2). At small N and when the Fermi level is inside a degenerate shell where the density of states is large, one arrives at the

ES law (1.4) and gets $\delta E = \gamma_1 \ll \Delta$. The localization length reaches a maximum at such N

$$\xi \simeq \frac{d}{\ln(\alpha d^2/n^{1/3}\rho^3)}. \tag{5.8}$$

When the Fermi level resides in the middle of the gap Δ between shells where the Mott variable range hopping takes over, the energy difference $\delta E \simeq \Delta$. Therefore, the localization length reaches its periodic minima which are given by Eq. (1.7). The local period is $\sim N^{1/3}$ and slowly changes with N. Eqs. (5.8) and (1.7) together give the envelope of the oscillating localization length as shown in Fig. 5.2 by the dotted line and the dashed line, respectively. We denote this phase as "oscillating insulator" (OI). Periodic oscillations of the hopping conductivity with N were observed in CdSe [82].

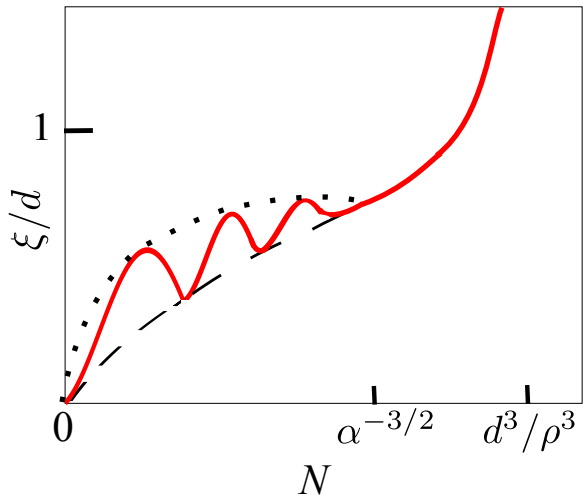

Figure 5.2: (Color online) Schematic plot of the localization length ξ (in units of the NC diameter d) as a function of the average number of donors N in a NC at $\alpha d^2/\rho^2 \gg 1$. The thick solid line (red) is the localization length. The dotted line represents the maximum value of ξ given by Eq. (5.8) which corresponds to the Fermi level position in the middle of the degenerate shell (the line of maxima). The dashed line goes through the minima of ξ which are somewhat lower than values given by Eq. (1.7) and happen when the Fermi level is near the middle of the gap Δ. When $N = \alpha^{-3/2}$, the energy shift due to NC diameter variations γ_1 reaches Δ, the oscillations of ξ stop and ξ obeys Eq. (1.7). At N close to d^3/ρ^3, the film approaches the IMT and its localization length diverges.

According to Eq. (5.5) γ_1 grows with N and reaches Δ at $N = \alpha^{-3/2}$. At larger N the energy difference δE saturates at Δ because of the spectrum periodicity. The corresponding system of electron energy levels with a smooth density of states is shown in Fig. 5.3. Thus, oscillations of $\xi(N)$ stop at $N = \alpha^{-3/2}$. We arrive at the usual insulator (I) where ξ obeys Eq. (1.7) which follows from $\delta E = \Delta$ and Eqs. (5.1), (5.6) and (5.7). This gives Eq. (1.6) for the critical concentration n_c. This sequence of changes of $\xi(N)$ is shown schematically in Fig. 5.2. Apparently it requires that

$$\alpha^{-3/2} \ll d^3/\rho^3. \tag{5.9}$$

In this section, we focus on the case of relatively small ρ when the inequality (5.9) holds. In this case, every maximum of ξ is finite because the argument of the logarithmic function in Eq. (5.8) $\alpha d^2/n^{1/3}\rho^3 = (\alpha d^2/\rho^2)^{3/2}/(N\alpha^{3/2})^{1/3} \gg 1$ at $N < \alpha^{-3/2}$. The case opposite to the inequality (5.9) corresponding to a smaller α and a larger ρ is studied in the next section.

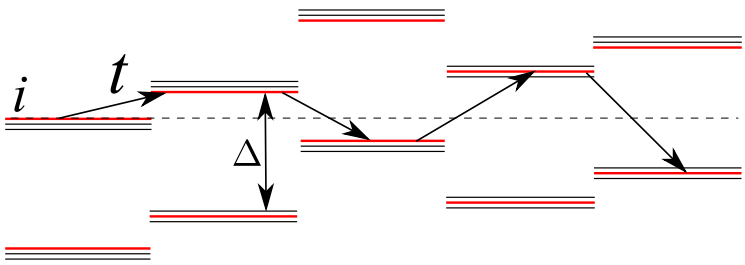

Figure 5.3: (Color online) Energy spectrum of a chain of NCs at large average electron number N. An electron tunnels from an initial NC i through intermediate NCs. Virtually visited levels are shown by arrows. The dashed line shows the energy of the tunneling electron close to the Fermi level. Each NC has a ladder of $(2l+1)$-degenerate (n,l)-shells with the gap Δ between them. Due to variations of diameters, the whole ladder of energy levels is shifted up and down by an energy larger than Δ. Here we show only two shells closest to the Fermi level. Only one level (red) of each shell contributes to the tunneling with the matrix element t.

One should note that our result for ξ is obtained away from the critical vicinity of n_c. So our estimate of n_c obtained from the condition $\xi = d$ needs a correction. Indeed we estimated the probability of the electron hopping between two distant NCs via the

elastic co-tunneling along a single typical chain of M NCs. Near the IMT one should add probability amplitudes of many such chains. Then the sum of all amplitudes gives a total probability $\propto (tK/\Delta)^M$. Here K is the connective constant of the NC lattice. According to Anderson [125], the IMT happens when $tK/\Delta = 1$. Using Eqs. (5.1) and (5.7), for the simple cubic lattice (where according to Ref. [126] $K = 4.7$) we arrive at the estimate $n_c \approx 0.5\rho^{-3}$ while for the face-centered cubic lattice (where $K = 10$ as given in Ref. [127]) we get $n_c \approx 0.2\rho^{-3}$. This result found from the insulating side of the IMT is reasonably close to Eq. (1.6) obtained from the metallic side.

So far, we have studied the case where the inequality (5.9) holds. Now we turn to the opposite situation $\alpha d^2/\rho^2 \ll 1$ of relatively large ρ and small α. In this case Eq. (5.8) indicates that the localization length periodically diverges at $\alpha^3 d^9/\rho^9 < N < d^3/\rho^3$. This means that electrons whose energy levels are in the middle of the shell are delocalized while those who are located in the tails of the density of states are still localized and have a localization length described by Eq. (1.7). We call this phase "blinking metal" (BM) since its metallicity occurs only at certain positions of the Fermi level (a good example of such metal is the quantum hall effect). However, at $N = d^3/\rho^3$, the system enters the usual metal (M) phase where electrons are delocalized regardless of the Fermi level position. The corresponding behavior of the localization length at $N \leq d^3/\rho^3$ is shown in Fig. 5.4. In this case, $\gamma_1 \ll \Delta$ at the IMT point since $d^3/\rho^3 \ll \alpha^{-3/2}$.

5.3 Role of NC charging due to donor number fluctuations

Let us now discuss another type of disorder present in the film, i.e., the fluctuations of the donor number δN around the average number N from NC to NC. At large N, δN is Gaussian-distributed, i.e., $\delta N \sim \sqrt{N}$. If each NC is neutral, δN would lead to substantial fluctuations $\delta E_F = E_F/\sqrt{N} \sim N^{1/6}\Delta$ of the Fermi energy E_F from one NC to another. To establish the unique chemical potential of electrons (the Fermi level), electrons move from NCs with larger-than-average n to ones with smaller-than-average n and NCs get charged creating the Coulomb potential in space. Below we argue that the typical number of charges Q in NCs depends on the ratio Δ/E_c as shown in Fig. 5.5.

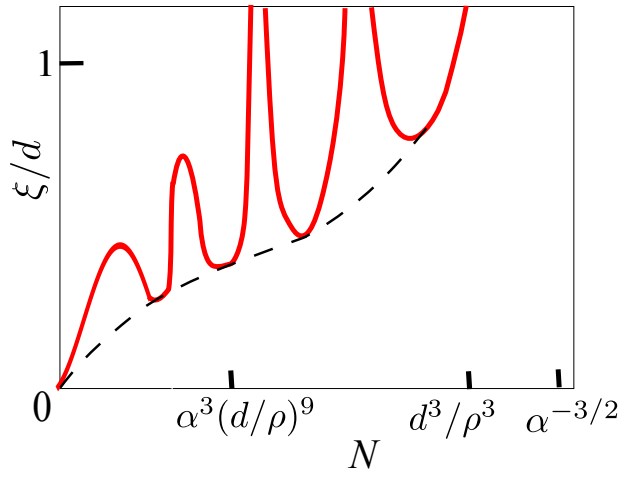

Figure 5.4: (Color online) The localization length ξ (in units of the NC diameter d) as a function of the average donor number N in a NC for $\alpha d^2/\rho^2 \ll 1$. The thick solid line (red) is the localization length. The dashed line represents the minima of ξ somewhat lower than values given by Eq. (1.7) occurring when the Fermi level is in the middle of the gap Δ. The film first becomes a "blinking metal" (BM) at $N = \alpha^3 d^9/\rho^9$, where ξ starts to periodically diverge and return to finite values. At $N = d^3/\rho^3$, the film enters the usual metal (M) domain.

When E_c is very small, the final chemical potential is established when NCs have almost the same number of electrons. Accordingly, most NCs obtain a net charge Qe where $Q \sim \sqrt{N}$. However, at larger E_c when $\Delta/E_c \ll N^{1/3}$, the price of charging gets so large that the number of transferred electrons $Q \sim N^{1/6}(\Delta/E_c)$ is much smaller than $\sqrt{N}$ (see Fig. 5.5). One arrives at this result by equating the initial fluctuation of the Fermi energy δE_F to the growth of the Coulomb potential of a NC QE_c. At $\Delta/E_c = N^{-1/6}$, charging becomes so costly that the charge number $Q = 1$. Beyond this point, all NCs are neutral (see Fig. 5.5).

One can understand the importance of the parameter $\Delta/N^{1/3}E_c$ by calculating the electronic screening radius of the film. Since the screening radius r_0 can be estimated as $\sqrt{\varepsilon_f/4\pi e^2 g(E)}$ where $g(E) \simeq N^{1/3}/\Delta d^3$ is the average density of states, one gets $r_0/d \simeq \sqrt{\Delta/N^{1/3}E_c} \gg 1$ at $\Delta/N^{1/3}E_c \gg 1$. We see that in agreement with Fig. 5.5, when $\Delta/N^{1/3}E_c \gg 1$ and $r_0 \gg d$ electrons do not screen donor charges, while in the opposite case $\Delta/N^{1/3}E_c \ll 1$ the electron screening becomes important.

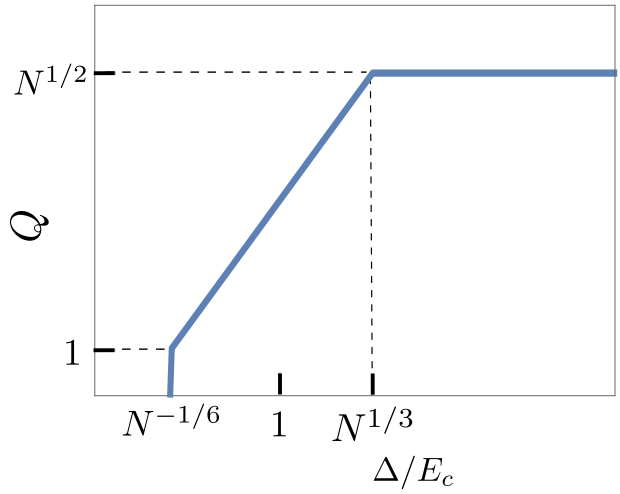

Figure 5.5: Schematic log-log plot of the typical number of charges Q in a NC as a function of the ratio Δ/E_c.

Due to charging of NCs, each NC finds itself in the environment of charged neighbors and gets a random potential energy shift up or down. Apparently the energy shift created by a single NC at the distance r where $d \ll r \ll r_0$ is QE_cd/r and the typical shift created collectively by all NCs in the sphere of radius r_0 is

$$\gamma_2 = \frac{QE_cd}{r_0}\left(\frac{r_0}{d}\right)^{3/2} = N^{5/12}E_c\left(\frac{\Delta}{E_c}\right)^{1/4}. \tag{5.10}$$

Note that γ_2 does not depend on d for fixed concentrations n. This is not surprising because one can arrive at the same result for potential energy fluctuations thinking about our film as a bulk heavily doped semiconductor with concentration $n \simeq N/d^3$ of randomly positioned donors screened by degenerate electron gas [128].

Let us find what happens when the charging effect outweighs the diameter variation. We start from the case $\alpha d^2/\rho^2 \gg 1$ and use that for Fig. 5.6 which in the $(N, \Delta/E_c)$ plane shows phases with different behaviors of the localization length. The upper part of Fig. 5.6 summarizes results obtained for diameter variations in Sec. 5.2.

We see how with growing N the film goes through an oscilating insulator (OI), an insulator (I) and a metal (M). Coulomb effects become important when $\gamma_2 > \gamma_1$ or according to Eqs. (5.5) and (5.10) $\Delta/E_c < 1/N^{1/3}\alpha^{4/3}$. At the upper OI-I border

$N = \alpha^{-3/2}$ where $\gamma_1 = \Delta$, this happens at $\Delta/E_c = \alpha^{-5/6}$. Let us explore now what happens at $\Delta/E_c < \alpha^{-5/6}$ where the energy difference $\delta E = \gamma_2$. When N is small, γ_2 is small too so that the density of states has periodic peaks and the localization length oscillates. The system is again an oscillating insulator (OI) (see the narrower part of the blue domain in Fig. 5.6). At larger N when $\Delta/E_c < N^{5/9}$, the energy shift γ_2 exceeds Δ so that away from the left blue domain shown in Fig. 5.6 we arrive at the spacial distribution of levels shown in Fig. 5.3. δE then saturates at Δ and one again obtains the result (1.7) for the localization length ξ. The system becomes a usual insulator (I). Thus in the case of relatively small ρ and large α when $\alpha d^2/\rho^2 \gg 1$, the localization length first stops oscillating and then diverges (the system enters first the domain I and then the domain M as shown in Fig. 5.6).

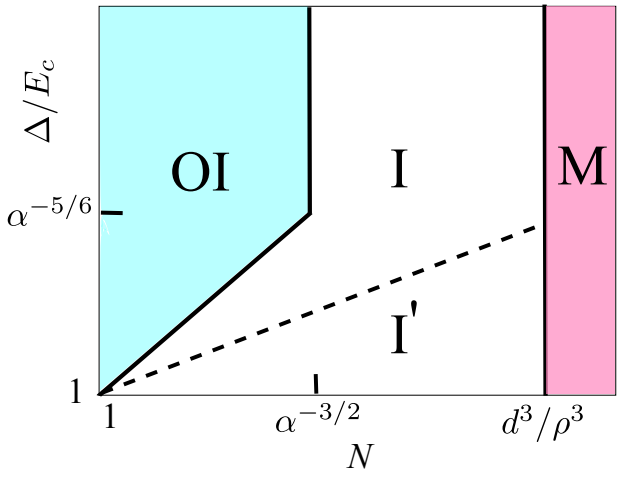

Figure 5.6: (Color online) A log-log map of different domains in the (N, Δ/E_c) plane at $\alpha d^2/\rho^2 \gg 1$. The light grey domain (blue online) corresponds to the regime where $\delta E < \Delta$ and the localization length oscillates with N. We call it an oscillating insulator (OI). Away from the left blue domain, the energy difference δE saturates at Δ and the localization length does not oscillate and obeys Eq. (1.7). This is the usual insulator (I). The darker grey domain (pink online) corresponds to the metallic phase (M). The solid border lines (from left to right) correspond to equations $\Delta/E_c = N^{5/9}$, $N = \alpha^{-3/2}$ and $N = d^3/\rho^3$, respectively. The dashed line corresponds to $\Delta/E_c = N^{1/3}$. In the domain below the dashed line (I'), (n, l)-shells get split and mixed with each other (see Sec. 5.7). In this domain, the localization length is given by Eq. (5.42).

In the opposite case of relatively large ρ and very small α where $\alpha d^2/\rho^2 \ll 1$ we analyze the role of Coulomb effects in Fig. 5.7. The upper part of this phase diagram $\Delta/E_c > \alpha^{-7/3}(d/\rho)^{-3}$ is again dominated by diameter variations. As shown in Sec. 5.2 in this case with growing N the film goes through an oscillating insulator (OI), a blinking metal (BM) and a metal (M). When we include Coulomb effects the vertical OI-BM border marked as the line 2) in Fig. 5.7 at which $\gamma_1 = t$ cannot continue below the point $\Delta/E_c = \alpha^{-7/3}(d/\rho)^{-3}$ where $\gamma_1 = \gamma_2$. Now the OI-BM border in Fig. 5.7 turns and goes along the line 3) at which $\gamma_2 = t$ or $\Delta/E_c = (d/\rho)^4/N^{7/9}$. The line 3) ends at $\Delta/E_c = (d/\rho)^{5/3}$ when $\gamma_2 = \Delta$ at the crossing with the generic metal border given by the line 4) where $\Delta = t$ and $N = d^3/\rho^3$ and with the OI-I border given by the line 1) where $\gamma_2 = \Delta$ and $\Delta/E_c = N^{5/9}$. This is a remarkable quadruple point where $\gamma_1 = \gamma_2 = \Delta = t$ and all four phases OI, BM, I and M meet.

5.4 Experimental implications for CdSe, InAs and ZnO NC

In previous section, we have studied theoretically possible situations for NC films as shown by phase diagrams in Figs. 5.6 and 5.7. Now we focus on several commonly used semiconductor NCs trying to put them on these diagrams. We choose the same geometrical parameters $\alpha = 0.15$, $d = 5$ nm, $\rho = \rho_a = 1.2$ nm for all of them. Then, we get $\alpha^{-3/2} \lesssim d^3/\rho^3$ and use the phase diagram Fig. 5.6. The upper part of the diagram where the NC diameter variation is the major source of disorder is separated from the lower one where Coulomb disorder dominates by $\Delta/E_c = \alpha^{-5/6} \simeq 5$. For CdSe NCs since $\Delta/E_c = 5$, the Coulomb effects are marginal so that we can think about the NC diameter variation only. When N increases, the film moves from OI to M as depicted by the upper part of the phase diagram in Fig. 5.6 with the intermediate region I being narrow and neglected since $\alpha^{-3/2}$ and d^3/ρ^3 are quite close. For InAs, since $\Delta/E_c = 27 \gg 5$, the Coulomb effects are completely negligible and again the system experiences the OI-I-M phase changes. For ZnO, however, the ratio $\Delta/E_c = 3 < 5$ and the random Coulomb potential is the leading disorder in the film. One should then use the lower part of Fig. 5.6 for the phase change process with increasing N. In this case we have the same sequence of phases OI-I-M but with now the phase I appreciably

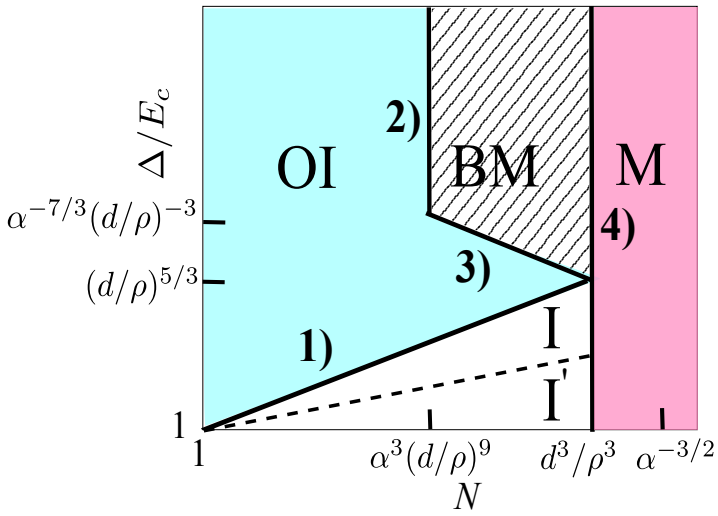

Figure 5.7: (Color online) A log-log map of different domains in the (N, Δ/E_c) plane at $\alpha d^2/\rho^2 \ll 1$. The light grey domain (blue online) corresponds to the regime where $\delta E < \Delta$ and the localization length oscillates with N (OI). The shaded domain belongs to the blinking metal (BM). In the white domain of the usual insulator (I) the localization length does not oscillate and obeys Eq. (1.7). The darker grey domain (pink online) corresponds to the metallic phase (M). The solid border lines 1)–4) correspond to conditions 1) $\gamma_2 = \Delta$, 2) $\gamma_1 = t$, 3) $\gamma_2 = t$, and 4) $\Delta = t$. The dashed line corresponds to $\Delta/E_c = N^{1/3}$. In the domain I' below the dashed line NC spectra become random (see Sec. 5.7). In this domain, the localization length is given by Eq. (5.42).

expanded by the Coulomb random potential. Si NC films are similar to that of ZnO as its $\Delta/E_c = 2$ is also very small.

One should note that there is no BM phase for the chosen parameters. To get this phase, one has to tune α down by making the NCs more monodisperse. For $d = 5$ nm and $\rho = \rho_a = 1.2$ nm, one needs $\alpha < 0.06$ to open the BM phase. This is probably the state-of-the-art monodispersity. To go even further, one may wonder whether the BM phase can be expanded all the way till $N = 1$. The inequality $\alpha d^3/\rho^3 \leq 1$ guarantees that the line 2) of Fig. 5.7 reaches the $N = 1$ line and simultaneously the condition $\Delta/E_c \geq (d/\rho)^4$ is required for the film to be above the point where line 3) crosses $N = 1$. If both inequalities are satisfied one can expect a desirable [91, 129, 130] band-like transport behavior of electrons when they populate only the 1S-level. However, for NCs

with $d = 5$ nm and $\rho = \rho_a \simeq 1.2$ nm, the necessary $\alpha = \rho^3/d^3 \simeq 0.01$ is unrealistically small while necessary $\Delta/E_c \geq (d/\rho)^4 \sim 200$ is too large. Even increasing ρ to $2\rho_a$ brings us only to criteria $\alpha \leq 0.1$ and $\Delta/E_c \geq 16$. Of course, our estimates are good only for $\rho \ll d/2$ so these numbers should not be taken too seriously. For ZnO (or Si), since $\Delta/E_c < (d/\rho)^{5/3}$ even at $\rho = 2$ nm, the system can never see a BM phase due to the large Coulomb disorder as shown by Fig. 5.7.

There is an important case where additional Coulomb fluctuations may be ignored. We are talking about NC films gated by an ionic liquid or an electrolyte [82, 81]. Anions which enter spaces between NCs and attract electrons in this case play the role of chemical donors we studied above. However, contrary to immobile dopants inside a NC anions remain mobile in the process of adjustment of the gate voltage and tend to screen electron charges [88]. Thus, in this case disorder effects due to fluctuations of NC diameters discussed in Sec. 5.2 should dominate. The ZnO (or Si) NC films then become similar to CdSe or InAs. At $\alpha d^2/\rho^2 \gg 1$ the OI domain expands while the I domain shrinks and at $\alpha d^2/\rho^2 \ll 1$, the OI and I regions are consumed by the BM phase.

5.5 Tunneling matrix element for nanocrystals touching by facets

Beyond the surface of a single NC in the surrounding medium, the wave function of an electron at the Fermi level decays with the distance s from the surface as $\propto e^{-s/b}$ where $b = \hbar/\sqrt{2m_0U_0}$. Here m_0 is the electron mass in the medium and U_0 is the workfunction of NCs. For $U_0 \simeq 4$ eV and $m_0 = m_e$, where m_e is the electron mass in vacuum, one gets $b \simeq 1\mathring{A}$, which is smaller than the lattice constant. So, approximately, the electron wave function is zero on the surface of NCs. When two NCs touch by contact facets, the electron wave function of the left NC is strongly modified inside the dashed sphere of radius ρ containing the facets. Namely, due to the right NC, the wave function acquires a tail leaking into the right NC (see Fig. 5.8a). The wave function inside the right NC is deformed in the same way. The overall wave function is split into two

$$\Psi_{s,a}(\boldsymbol{r}) = \frac{1}{\sqrt{2}}\left[\psi(\boldsymbol{r} - \boldsymbol{r_L}) \pm \psi(\boldsymbol{r} - \boldsymbol{r_R})\right], \tag{5.11}$$

which are symmetric and asymmetric combinations of the modified wave function ψ inside each NC (see Fig. 5.8b). The origin is set at the center of the contact and the polar axis is pointed towards the center of the right NC. The coordinates of the centers of left and right NCs are $\boldsymbol{r_L}$ and $\boldsymbol{r_R}$, respectively. $\psi(\boldsymbol{r}-\boldsymbol{r_L})$ refers to the wave function in the left NC and $\psi(\boldsymbol{r}-\boldsymbol{r_R})$ is that of the right one. Below, we just use the left wave function for discussion and simply denote it as ψ. The tunneling matrix element t between two NCs can be estimated by calculating the energy splitting between the symmetric and asymmetric wave functions $\Psi_{s,a}$ of Eq. (5.11). As in the problem of calculating the electron terms of the molecular ion H_2^+ in § 81 of Ref. [47], the energy splitting can be calculated as

$$t = \int \frac{\hbar^2}{m^*}\psi\frac{d\psi}{dz}dx\,dy \tag{5.12}$$

where the integral is taken over the contact boundary plane $z = 0$ (see the vertical dashed line in Fig. 5.8b). In the case we are discussing now, the contact is made of the touching facets. In this contact plane, ψ vanishes at (x, y) outside the facets in the surrounding medium.

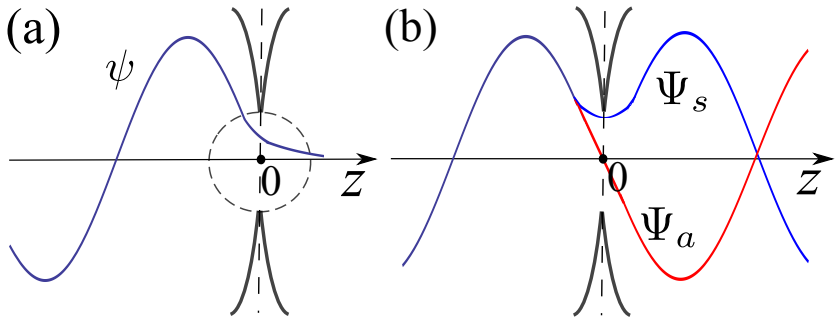

Figure 5.8: (Color online) Electron wave functions near the contact facet. The vertical dashed line indicates the facet boundary plane. (a) Electron wave function ψ of the left NC modified by the right one. It acquires a tail penetrating into the right NC mainly in the region of the dashed sphere. (b) Overall wave function as symmetric (blue) or asymmetric (red) combinations of each NC wave function given by Eq. (5.11). The energy difference between these two states is twice the tunneling matrix element t given by Eq. (5.12).

Let us deal with E_F belonging to a degenerate (n, l)-shell. Then, the unperturbed

wave function of the left NC is $\psi_0(\boldsymbol{r}-\boldsymbol{r_L}) \simeq j_l(k_n r')Y_l^m(\theta',\phi')/\sqrt{d/k_n^2}$ where j_l is the spherical Bessel function, Y_l^m are spherical harmonics, $k_n d/2$ is the nth zero point of the Bessel function and $k_n \approx 2\pi n/d \sim k_F$, $(r',\,\theta',\,\phi')$ are the coordinates of $\boldsymbol{r'} = \boldsymbol{r}-\boldsymbol{r_L}$ in the spherical coordinate system. $Y_l^m(\theta',\phi') \to 0$ at $\theta' \to 0$ for all $m \neq 0$, and for $m = 0$ $Y_l^0(0,\phi') = \sqrt{(2l+1)/4\pi} > 0$. Thus among the $2l+1$ degenerate levels of the (n,l)-shell only one state ($m = 0$) oriented along the z axis contributes to the tunneling between neighboring NCs (marked red in Figs. 1.10, 5.1, and 5.3). So we just need to calculate the tunneling matrix element t of the $m = 0$ state. When the number N of electrons inside each NC is large, for the (n,l)-shell at the Fermi level, we have $n \sim l \sim N^{1/3} \simeq k_F d$ since the radial and angular kinetic energies should be of the same order. So for the $m = 0$ state, the wave function is highly concentrated near the z axis spreading mainly within the polar angle $\sim 1/\sqrt{l} \sim 1/\sqrt{k_F d}$. More accurately, since each (n,l)-shell has $2l+1$ degeneracy, we get

$$N \approx 2n(l+1)^2 \sim 2l^3, \tag{5.13}$$

where the factor 2 comes from the spin degeneracy. As $N = 4\pi n(d/2)^3/3 = k_F^3 d^3/18\pi$, we get $n \sim l \sim \left(k_F^3 d^3/36\pi\right)^{1/3}$. The radial distribution is described by $j_l(k_n r') \simeq \sin[k_n(r'-d/2)]/k_n r'$ at large r'. Therefore, we get approximately the normalized unperturbed wave function

$$\psi_0 \approx \frac{2\sin\left[k_n(r'-d/2)\right]}{\sqrt{d}r'} Y_l^0(\theta',\phi') \tag{5.14}$$

at large distance from the left NC center. So near the facet, the original unperturbed wave function ψ_0 can locally be regarded as an incident plane wave superposed by its completely reflected wave from the surface, i.e., $\psi_0 \approx 2\sqrt{2l/\pi}\sin[k_n(z'-d/2)]/d^{3/2}$, where $z' \approx r'$ is the z-component of $\boldsymbol{r'}$.

As a result, the problem of an electron tunneling through a facet is analogous to the one of a plane wave with the wavenumber k_F diffracting on a circular aperture with radius ρ in $z = 0$ plane screen. In the regime where $k_F\rho \ll 1$, Bethe [131] solved this diffraction problem for microwaves, while Levine and Schwinger [132] and Bouwkamp [133] solved it for a scalar plane wave. Here we use the simple solution in the first-order approximation in $k_F\rho \ll 1$ given by Rayleigh [134].

One can write the Schrodinger equation for the function ψ as

$$\nabla^2\psi + k_F^2\psi = 0. \tag{5.15}$$

Boundary conditions on the $z = 0$ plane are $\psi = 0$ on the screen and $d\psi/dz$ is continuous at the aperture. We write the solution ψ as the sum of ψ_0 and $\delta\psi$, where $\delta\psi$ is the correction due to the aperture opening and the unperturbed wave function ψ_0 of the left NC is zero on the right side of the boundary plane ($z > 0$). We denote $\delta\psi_L, \delta\psi_R$ as the left ($z < 0$) and right ($z > 0$) part of the correction function $\delta\psi$ respectively. So in the $z = 0$ boundary plane, $\delta\psi_L = \delta\psi_R$ and outside the aperture $\delta\psi_L = \delta\psi_R = 0$. The continuity of the derivative $d\psi/dz$ leads to a jump of $d(\delta\psi)/dz$, i.e., $d\psi_0/dz + d(\delta\psi_L)/dz = d(\delta\psi_R)/dz$. The symmetry between $\delta\psi_L$ and $\delta\psi_R$ gives $d(\delta\psi_L)/dz = -d(\delta\psi_R)/dz$ in the aperture. (The proof can be found in Refs. [131, 134]. For a possible interpretation of this result, let us consider the standing-wave solution of Shrodinger equation Eq. (5.15) in a free space: $\psi = \exp(ik_Fz) - \exp(-ik_Fz)$. Since $\psi = 0$ at $z = 0$, this means that ψ is also the solution of the Shrodinger equation if the screen is located at $z = 0$. This solution can be viewed as two plane waves $\exp(ik_Fz)$ and $-\exp(-ik_Fz)$, which fall from opposite directions on the screen and are reflected back completely. The aperture gives rise to corrections $\delta\psi_R$ and $\delta\psi_L$ to each wave. Since the screen does not affect the wave function ψ, these corrections to plane waves cancel each other, i.e. $\delta\psi_R(z) - \delta\psi_L(-z) = 0$. We then get that $d(\delta\psi_R)/dz = -d(\delta\psi_L)/dz$ by differentiating this relation.) Therefore $d(\delta\psi_R)/dz = (d\psi_0/dz)/2 \approx \sqrt{2l/\pi}k_n/d^{3/2}$. Now one can rewrite the integral for t in terms of the correction to the wave function on the right side which is $\delta\psi_R$

$$t = \frac{\hbar^2}{m^*}\int \delta\psi_R \frac{d\delta\psi_R}{dz} dxdy, \tag{5.16}$$

where $\delta\psi_R$ satisfies the Schrodinger equation (5.15). At the aperture $\nabla^2(\delta\psi_R) \sim \delta\psi_R/\rho^2 \gg k_F^2\delta\psi_R$ because $k_F\rho \ll 1$. In the first approximation we can neglect the latter term and thus deal with the Laplace's equation

$$\nabla^2(\delta\psi_R) = 0 \tag{5.17}$$

with the boundary conditions $\delta\psi_R = 0$ on the screen and $d(\delta\psi_R)/dz \approx \sqrt{2l/\pi}k_n/d^{3/2}$ at the aperture.

Mathematically, an identical problem was exactly solved in hydrodynamics (see § 108 in Ref. [135]). Indeed, the Laplace's equation $\nabla^2\varphi = 0$ can be used to describe the motion of a rigid disk of radius ρ moving with velocity u along its axis (defined as the z axis with the origin at the disk center) through unlimited incompressible liquid if φ denotes the velocity potential. Boundary conditions for φ are that $\nabla\varphi = u$ on the disk and $\varphi = 0$ at $z = 0$ outside the disk. The kinetic energy of the liquid in the $z > 0$ space is

$$K_E = \frac{1}{2} g \int (\nabla\varphi)^2 \, dV, \tag{5.18}$$

where g is the density of the liquid. Using Green's theorem and the Laplace's equation for the right half space ($z > 0$), we get

$$K_E = \frac{1}{2} g \int \varphi \frac{d\varphi}{dz} dxdy \tag{5.19}$$

where the integral is taken over the whole $z = 0$ plane. The potential φ is zero outside the disk. Therefore, the integration is over the disk only, as in Eq. (5.16). Knowing the exact solution for φ one can arrive at $K_E = (2/3)g\rho^3u^2$ (see § 108 in Ref. [135]). Thus

$$\int \varphi \frac{d\varphi}{dz} dxdy = \frac{4}{3}\rho^3 u^2. \tag{5.20}$$

In our diffraction problem, $\delta\psi_R$ plays the role of φ and $d(\delta\psi_R)/dz \approx \sqrt{2l/\pi}k_n/d^{3/2}$ plays the role of u. Therefore, using Eq. (5.2), we get the tunneling matrix element t in Eq. (5.16)

$$t = \frac{0.3\hbar^2 k_F^3 \rho^3}{m^* d^2} = \frac{9\hbar^2 n \rho^3}{m^* d^2}. \tag{5.21}$$

At $k_F d \sim 1$, one gets the tunneling matrix element for the 1s band

$$t \simeq \frac{\hbar^2 \rho^3}{m^* d^5} \ . \tag{5.22}$$

In Ref. [136], a solution-based oriented attachment method was used to prepare fused dimers of two semiconductor NCs. These dimers can be seen as two NCs touching by their facets. Eq. (5.22) for t can then be used to calculate the splitting of the first exciton absorption line in the dimer spectrum. One should note that Eq. (5.22) is obtained here in the limit of infinitesimal tunneling distance b (which is further explained in Sec. 5.6). In the same limit, the method used in Ref. [136] leads to a smaller $t \simeq \hbar^2\rho^4/m^*d^6$.

The reason for this difference is that on the facet plane our wave function has a larger magnitude than the one conjectured in Ref. [136].

One can interpret the result for the tunneling matrix element Eq. (5.21) as following. Originally the wave function ψ_0 is zero on the boundary plane and its derivative along the z axis is $\simeq k_F^{3/2}/d$ on the contact facet. Now due to the existence of the facet, the electron wave function is modified as ψ which leaks into the right NC and is nonzero on the facet, while the derivative is hardly changed by the small perturbations. Because the wave function substantially changes over a distance ρ, we can say that $\psi \approx (d\psi/dz)\rho$. As a result,

$$\begin{aligned} \psi \simeq & \frac{k_F^{3/2}\rho}{d}, \\ \frac{d\psi}{dz} \simeq & \frac{k_F^{3/2}}{d} \end{aligned} \tag{5.23}$$

inside the contact facet in the $z = 0$ plane for the $m = 0$ state which is highly oriented along the z axis. So we get the result (5.21) for t. From this t we arrive at Eq. (1.7) for the localization length and Eq. (1.6) for the critical concentration n_c.

A schematic plot of n_c as a function of the facet radius ρ is presented in Fig. 5.9. The critical concentration scales as $\simeq 0.3/\rho^3$ at all $\rho \ll d/2$. In the vicinity of $\rho = d/2$, electrons are no longer confined inside each NC and the film becomes a bulk semiconductor. In this case, $n_c a_B^3 \simeq 0.02$, we return to the Mott criterion for the IMT and get a drastic drop of the critical concentration from $\simeq 2/d^3$ to $0.02/a_B^3$.

5.6 Nanocrystals touching away from facets

When NCs touch each other away from prominent facets by an area of the atomic size $a \ll \rho$, the electrons tunnel mainly via the effective "b-contact" of radius $\rho_b = \sqrt{db/2} \gg a$ (see Fig. 5.10). For electrons tunneling between NCs outside this contact, the tunneling distance is larger than b and the probability is negligible due to the exponentially decaying wave function.

Since electrons have to tunnel through the medium where they have mass m_0, when calculating the integral Eq. (5.12) over the contact boundary plane here, we need to

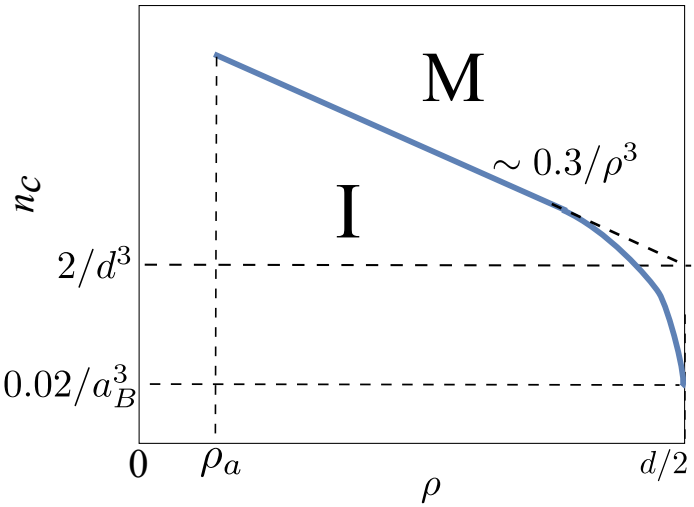

Figure 5.9: Schematic logarithmic plot of the critical concentration n_c as a function of the facet radius ρ at $a_B \gg d$. Both axes use logarithmic scales. Near $\rho = d/2$, the critical concentration abruptly drops to its value for the bulk semiconductor.

replace the effective mass m^* with m

$$t = \int \frac{\hbar^2}{m_0} \psi \frac{d\psi}{dz} dx\, dy. \tag{5.24}$$

In this case we can use the approximation of linear combination of atomic orbitals (LCAO) in the way done for the ground state in Ref. [91]. We calculate $\psi = \psi_0$ as the wave function for a single spherical NC embedded in the infinite surrounding medium with the finite decay length b. For simplicity, in this section and below we do only scaling analysis ignoring numerical coefficients.

Using the continuity of the wave function on the NC surface, we get

$$\psi_0 \simeq \frac{k_F}{\sqrt{d}} Y_l^m(\theta', \phi') \begin{cases} j_l(k_F r') & r' < d/2 \\ \dfrac{j_l\left(k_F d/2\right)}{h_l^{(1)}(id/2b)} h_l^{(1)}(ir'/b) & r' > d/2, \end{cases} \tag{5.25}$$

where $h_l^{(1)}$ is the first-kind spherical Hankel function and only $Y_l^0(\theta', \phi')$ is nonzero at $\theta' = 0$ corresponding to the state participating in the tunneling. The origin is set at

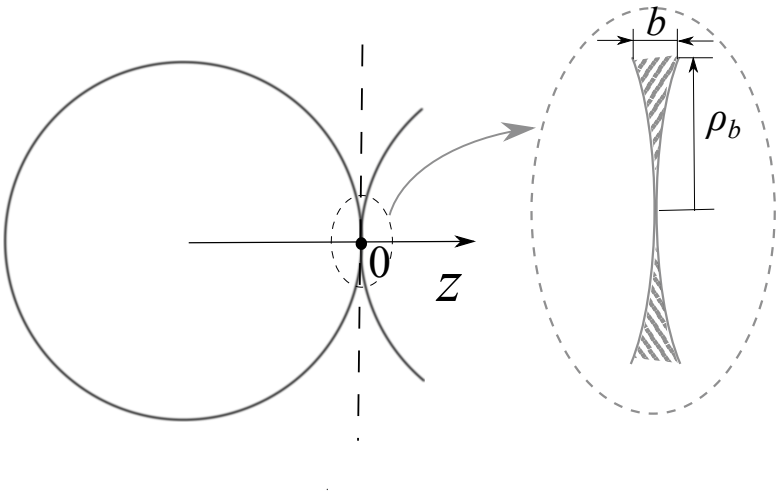

Figure 5.10: Two NCs touching away from prominent facets. In this case, electrons tunnel through the b-contact shown in the inset.

the touching point of NCs with the z axis pointed towards the center of the right NC and therefore the boundary plane is at $z = 0$ (see the vertical dashed line in Fig. 5.10). Again (r', θ', ϕ') are the coordinates of $\boldsymbol{r'} = \boldsymbol{r} - \boldsymbol{r_L}$ in the spherical coordinate system and $\boldsymbol{r_L}$ is the coordinate of the center of the left NC. For the finite potential barrier U_0 the derivative of the wave function divided by the effective mass is continuous across the surface, i.e.,

$$\left.\frac{d\psi_0}{dr'}\frac{1}{m^*}\right|_{r'-d/2=0^-} = \left.\frac{d\psi_0}{dr'}\frac{1}{m_0}\right|_{r'-d/2=0^+}. \tag{5.26}$$

Using that $j_l(k_F r') \simeq \sin\left[k_F r' + \varphi_l\right]/k_F r'$, $h_l^{(1)}(ir'/b) \simeq be^{-r'/b}/r'$ at large r' near the surface where φ_l is a constant, we have

$$\cot\left(\frac{k_F d}{2} + \varphi_l\right) \simeq -\frac{m^*}{m_0 k_F b} + \frac{2}{k_F d} \tag{5.27}$$

where $d/b \gg 1$, $m_0/m^* \gg 1$, $k_F d \gg 1$ at high doping concentration and $k_F d \sim 1$ for the ground state. At $1/k_F b \gg m_0/m^*$, the cotangent function diverges which means $\cos\left(k_F d/2 + \varphi_l\right) \approx 1$, $1/\sin(k_F d/2 + \varphi_l) \approx -m^*/m_0 k_F b$. So on the boundary plane

inside the b-contact ($r' - d/2 = 0^+$), we have

$$\begin{aligned} \psi_0 \simeq & \frac{-k_F}{\sqrt{d}} \frac{m_0 k_F b}{k_F d m^*} \sqrt{l} \\ \frac{d\psi_0}{dr} \simeq & \frac{k_F}{\sqrt{d}} \frac{m_0 k_F}{k_F d m^*} \sqrt{l}. \end{aligned} \tag{5.28}$$

The tunneling matrix element is then

$$t \simeq \frac{\hbar^2 k_F^3 d b^2 (m_0/m^*)}{m^* d^2}. \tag{5.29}$$

At $1/k_F b \ll m_0/m^*$, the cotangent function either vanishes or is finite depending on whether $d/b \gg m_0/m^*$ or $k_F d \gg 1$ is satisfied. This means the sine function is always finite and of the order 1. So inside the b-contact we get

$$\begin{aligned} \psi_0 \simeq & \frac{k_F}{\sqrt{d}} \frac{1}{k_F d} \sqrt{l} \\ \frac{d\psi_0}{dr} \simeq & \frac{-k_F}{\sqrt{d}} \frac{1}{k_F d b} \sqrt{l}, \end{aligned} \tag{5.30}$$

and the tunneling matrix element is

$$t \simeq \frac{\hbar^2 k_F d (m^*/m_0)}{m^* d^2}. \tag{5.31}$$

One can check that when we put $k_F^{-1} \sim d$ into Eqs. (5.29) and (5.31), we get the same tunneling matrix elements for the ground state as derived in Ref. [91] for NCs touching in one point.

According to Eqs. (5.29) and (5.31), the localization length is then

$$\xi \approx \begin{cases} \dfrac{d}{\ln\left[1/ndb^2(m_0/m^*)\right]}, & \dfrac{m_0}{m^*} \ll \dfrac{1}{n^{1/3}b} \\ \dfrac{d}{\ln\left[1/n^{1/3}d(m^*/m_0)\right]}, & \dfrac{m_0}{m^*} \gg \dfrac{1}{n^{1/3}b}. \end{cases} \tag{5.32}$$

This leads to the critical concentration

$$n_c \simeq \begin{cases} \dfrac{1}{b^2 d} \dfrac{m^*}{m_0}, & \dfrac{m_0}{m^*} \ll \left(\dfrac{d}{b}\right)^{1/2} \\ \dfrac{1}{d^3} \left(\dfrac{m_0}{m^*}\right)^3, & \dfrac{m_0}{m^*} \gg \left(\dfrac{d}{b}\right)^{1/2}, \end{cases} \tag{5.33}$$

which has its minimum value $n_c \simeq 1/(db)^{3/2} = 1/\rho_b^3$ at $m_0/m^* \simeq \sqrt{d/b}$. Even this minimum value is much larger than $1/\rho_a^3$ since $\rho_a \gg \rho_b$. Thus, when NCs touch away from prominent facets the critical concentration is pushed much higher. In fact, for CdSe NC films, by using $b = 0.1$ nm, $d = 5$ nm, $m_0 = m_e$, $m^* = 0.13m_e$ [137] where m_e is the free electron mass, we get $n_c \simeq 3 \times 10^{21}\text{cm}^{-3}$, which is difficult to achieve.

When NCs are separated by short ligands [138] by a small distance s, the overlapping wave functions exponentially decay as $\propto e^{-s/b}$ between neighboring NCs. Following a procedure similar to above derivations, we can get the tunneling matrix element t as

$$t \simeq \frac{\hbar^2}{m^* d^2} \exp\left(-\frac{s}{b}\right) \begin{cases} k_F^3 b^2 d \dfrac{m_0}{m^*}, & \dfrac{m_0}{m^*} \ll \dfrac{1}{k_F b} \\ \\ k_F d \dfrac{m^*}{m_0}, & \dfrac{m_0}{m^*} \gg \dfrac{1}{k_F b}. \end{cases} \tag{5.34}$$

At smallest $k_F = 1/d$, Eq. (5.34) gives the same results as in Ref. [91] for NCs separated by short ligands.

Therefore, we get the localization length

$$\xi \approx \begin{cases} \dfrac{d}{s/b + \ln\left[1/ndb^2(m_0/m^*)\right]}, & \dfrac{m_0}{m^*} \ll \dfrac{1}{n^{1/3}b} \\ \\ \dfrac{d}{s/b + \ln\left[1/n^{1/3}d(m^*/m_0)\right]}, & \dfrac{m_0}{m^*} \gg \dfrac{1}{n^{1/3}b}. \end{cases} \tag{5.35}$$

At large s we can ignore the logarithmic terms originating from the prefactor of t. But for small s, near the IMT, the role of these terms becomes important. One should note that even when NCs touch by short ligands, the localization length of electrons can be enhanced by increasing the doping concentration n inside each NC. The critical concentration n_c is then

$$n_c \simeq \begin{cases} \dfrac{1}{b^2 d} \dfrac{m^*}{m_0} \exp\left(\dfrac{s}{b}\right), & s \ll b \ln\left[\left(\dfrac{m^*}{m_0}\right)^2 \dfrac{d}{b}\right] \\ \\ \dfrac{1}{d^3}\left(\dfrac{m_0}{m^*}\right)^3 \exp\left(\dfrac{3s}{b}\right), & s \gg b \ln\left[\left(\dfrac{m^*}{m_0}\right)^2 \dfrac{d}{b}\right] \end{cases} \tag{5.36}$$

which can easily become unrealistically large.

5.7 Random-spectrum NC

In previous sections, we have studied the highly degenerate case assuming that the splitting of (n,l)-shells is much smaller than the energy gap Δ. In this section, we discuss limits of applicability of this assumption and find the localization length for strongly split and mixed $(n,l)-$shells which form a random spectrum similar to the case of metal garnules [139, 122, 123, 140, 124]. We show below that this happens at relatively small $\Delta/E_c < N^{1/3}$ or in the domain below the dashed line on Figs. 5.6 and 5.7. So the theory of this section is applicable for large enough NCs made from Si or ZnO.

Besides shifting the ladder of degenerate levels up and down discussed above, the random electric field created by neighboring charged NCs can split the degenerate shells of each NC due to the Stark effect. This field determined by nearest-neighbor NCs is $\mathscr{E} \sim e\sqrt{N}/\varepsilon_f d^2$. Electrons in the NCs respond to the internal field, which is smaller than $\mathscr{E}$ by the factor $3/(2+\varepsilon/\varepsilon_f)$. As we said in Sec. 5.1, $\varepsilon/\varepsilon_f$ is $\simeq 3$, so this factor is $\simeq 3/5$ and we will ignore it.

To calculate the Stark splitting we first note that the matrix element of the electric field potential does not vanish only between shells with l values differing by unity and is then of the order of $e\mathscr{E}d$. The typical energy difference between such shells in the spherical well with N electrons is $N^{1/3}\Delta$. Therefore, the typical Stark energy shift or the width of the split shell W emerges in the second-order perturbation theory and is

$$W \simeq \frac{(e\mathscr{E}d)^2}{N^{1/3}\Delta}. \tag{5.37}$$

(The Stark splitting can also come from random positions of N donors inside each NC and is comparable to Eq. (5.37). This disorder creates an internal dipole moment $\sim \sqrt{N}ed$ and an electric field, oriented in a random direction.)

Comparing Eq. (5.37) with the energy gap Δ between consecutive shells, we see that at

$$\Delta/E_c < N^{1/3} \tag{5.38}$$

the levels become random with the spacing $\delta = \Delta/N^{1/3}$ as the only characteristic energy (One may note that this criterion for degeneracy lifting is different from the one in Ref. [86]. However, since the critical concentration n_c has the same expression in

both degenerate and nondegenerate cases, this does not affect the correctness of the metal-insulator transition criterion obtained in Ref. [86].). $\Delta/E_c = N^{1/3}$ is shown in Figs. 5.6 and 5.7 by the dashed lines separating I and I' phases. When the inequality (5.38) holds, the degeneracy is broken and different (n, l)-shells mix with each other. Thus inside each NC, the states close to the Fermi level and, therefore, involved in the electron tunneling have typically different l numbers so that they have different parity and their tunneling matrix element t has random signs. The electron wave functions of different m hybridize and become chaotic instead of being confined in certain polar angles. So the typical magnitude of the wave function on the contact facet is $\sqrt{k_F d}$ times smaller than that of the "red" m=0 state for the degenerate case. These changes lead to the random matrix spectrum case which has been studied in previous work for larger dots[139, 122, 123, 140, 124]. In this case,

$$\begin{aligned} \psi &\simeq \frac{k_F \rho}{d^{3/2}}, \\ \frac{d\psi}{dz} &\simeq \frac{k_F}{d} \end{aligned} \tag{5.39}$$

where k_F is given by Eq. (5.2). Therefore, the typical tunneling matrix element is

$$t \simeq \frac{\hbar^2 k_F^2 \rho^3}{m^* d^3}. \tag{5.40}$$

At the same time, the energy gap between consecutive non-degenerate levels is also reduced to $\delta \simeq \Delta/(2l+1) \simeq \hbar^2/m^* d^3 k_F$. Then according to Refs. [122, 124] the localization length is

$$\xi \approx \frac{d}{\ln\left(\sqrt{E_c \delta}/t\right)}. \tag{5.41}$$

So one gets

$$\xi \approx \frac{d}{\ln\left(d/a_b^{1/2} n^{5/6} \rho^3\right)} \tag{5.42}$$

where $a_b = \varepsilon_f \hbar^2/m^* e^2$ and ε_f is the effective dielectric constant of the film.

According to Eq. (5.42), at $t \simeq \delta$, the localization length is still much smaller than the NC diameter d, which seems to indicate a criterion different from $t \simeq \delta$ for the IMT. However, one should notice that as $t \to \delta$, the charge discreteness is no longer well preserved and the charging energy vanishes [141, 142], so δ takes the place of E_c and changes the expression of ξ to $d/\ln(\delta/t)$. Using Eq. (5.40) and $\delta \simeq \hbar^2/m^* d^3 k_F$,

we get $t \simeq \delta$ at $k_F\rho \sim 1$. The localization length ξ becomes comparable to d at this point. This again leads to our above criterion Eq. (1.6), the same as for the degenerate case. Since this elimination of charging energy occurs in the vicinity of the IMT, we should see a steep growth of the localization length, which is a major feature different from the degenerate case. According to Eq. (1.6), $n_c \gg n_M$ at $\rho \ll a_B$. The critical concentration decreases with ρ and saturates at n_M when $\rho \sim a_B$.

Chapter 6

Conclusion and Discussion

In this thesis, we have discussed transport properties of electron accumulation layers induced by a very strong electric field on the surface of the STO crystal, and extended the study of electron distribution to more complicated planar STO-based structures and other geometries. We have also looked at the detail of the surface scattering by roughness to complement the scaling analysis of the transport properties of STO accumulation layers. For the second part of this thesis, we have studied the semiconductor NC film which is another material important for applications by investigating the electric conductivity in such films. The results are summarized below.

In Chapter 2, we show that due to the strongly nonlinear dielectric response of STO the electron density in an accumulation layer has a very compact body and a long slowly decaying tail. If in the body electrons are strongly scattered by the surface while in the tail electrons need a long time to reach the surface, the tail electrons run away in the source-drain electric field and produce dominating contributions to many kinetic coefficients. As a result the layer mobility, the Hall factor, the magnetoresistance, and the thermopower become anomalously large and dependent on the width of the STO sample and its bulk relaxation time.

In Chapter 3, we extend the study from a single accumulation layer to overlapping ones, and investigate the electron "spill-out" from a heavily n-type doped STO (NSTO) into a moderately n-type doped STO. In this chapter, we also study the electron distribution for spherical and cylindrical geometries and find the collapse of electrons onto spherical and cylindrical donor clusters. Such " fall-to-the-center" originates from

the very fast decrease of the electron potential energy near the cluster which is $\propto (-1/r^5)$ in the spherical case and in turn is a result of the strongly nonlinear dielectric response of STO. This leads to a very unusual two-scale shape of the electron density around the cluster.

In Chapter 4, we have studied the surface-roughness limited mobility in inversion and multisubband accumulation layers in conventional semiconductors with the linear dielectric response as a function of the 2D electron concentration N for two models of the surface roughness both quantum-mechanically and quasi-classically. For the more realistic exponential roughness, the mobility decreases as $\propto 1/N$ at large N and results in a 2D conductivity saturation as $\sigma/(2e^2/h) \simeq \Lambda a_B/\Delta^2 \gg 1$ since the characteristic roughness size Λ and the effective Bohr radius a_B are larger than the characteristic roughness height $\Delta \simeq a/2$ where a is the lattice constant. For the Gaussian roughness which was widely used in earlier studies, the minimum conductivity is found to be larger than the critical value as well. So there is no reason to expect the re-entrant metal-insulator transition [70] at large concentrations, consistent with observations of decent conductivities in large concentration accumulation layers in Refs. [71, 64, 65, 62]. The expression for the surface relaxation time can be used for the STO case with the nonlinear dielectric response, where there is no reentrant metal-insulator transition, either, at experimentally available large N.

In Chapter 5, we studied theoretically what happens to the variable range hopping conductivity of semiconductor NC films when NCs are doped by donors with the concentration n. Experiments show that the localization length of electrons $\xi(n)$ grows with n and at some $n \sim n_c$ becomes larger than the diameter d of NCs, what signals that the film is approaching the IMT. We provide theoretical estimates of $\xi(n)$ and n_c. The localization length is determined by the competition of disorder and transfer matrix element $t(n)$ between neighboring NCs. We concentrated on the case of small spherical NCs in which the electron spectrum consists of degenerate energy shells separated by the quantization gap Δ. In such films energy levels of NCs vary due to the dispersion of NC diameters and variations of the number of donors from NC to NC which result in random Coulomb potentials. We showed that for the standard diameter dispersion it is important for $\Delta/E_c > 5$, where E_c is the charging energy, while the Coulomb disorder dominates for the opposite case $\Delta/E_c < 5$. The matrix element $t(n)$ grows

with n and depends on the geometry of contacts between NCs. We calculated $t(n)$ for different types of contacts. We showed that for a finite separation between NCs or even when NCs touch each other by one point, the IMT may need unrealistically large n. This is why we focused on the case when close-to-spherical NCs touch by smallest facets . We found $\xi(n)$ in this case and our results are in qualitative agreement with the experimental data for $\xi(n)$ obtained in Ref. [86]. For these facets n_c is still relatively high and for $d = 5$ nm CdSe NCs it corresponds to $N \sim 20$ electrons per NC, which justifies our large-N approach. To make n_c smaller one should deal with small NCs with $\Delta/E_c > 5$ and use NCs touching by larger facets. Another route is making much smaller dispersion of diameters, but this route does not look realistic.

References

[1] J. Chakhalian, J. W. Freeland, A. J. Millis, C. Panagopoulos, and J. M. Rondinelli. Emergent properties in plane view: Strong correlations at oxide interfaces. *Rev. Mod. Phys.*, 86:1189, 2014.

[2] Susanne Stemmer and S. James Allen. Two-dimensional electron gases at complex oxide interfaces. *Annual Review of Materials Research*, 44(1):null, 2014, http://www.annualreviews.org/doi/pdf/10.1146/annurev-matsci-070813-113552.

[3] P. Zubko, S. Gariglio, M. Gabay, P. Ghosez, and J-M. Triscone. Interface physics in complex oxide heterostructures. *Annual Review of Condensed Matter Physics*, 2:141, 2011.

[4] A. Ohtomo and H. Y. Hwang. A high-mobility electron gas at the LaAlO3/SrTiO3 heterointerface. *Nature*, 427(6973):423–426, jan 2004.

[5] Yanwu Xie, Christopher Bell, Yasuyuki Hikita, Satoshi Harashima, and Harold Y. Hwang. Enhancing electron mobility at the laalo3/srtio3 interface by surface control. *Advanced Materials*, 25(34):4735–4738, 2013.

[6] David A. Muller Naoyuki Nakagawa, Harold Y. Hwang. Why some interfaces cannot be sharp. *Nature Materials*, (3):204209, 2006.

[7] Farrel W. Lytle. Xray diffractometry of lowtemperature phase transformations in strontium titanate. *Journal of Applied Physics*, 35(7):2212–2215, 1964.

[8] Tyler A. Cain, Evgeny Mikheev, Clayton A. Jackson, and Susanne Stemmer. Dichotomy of the transport coefficients of correlated electron liquids in srtio3. 2016, arXiv:1609.04149.

[9] C. He, T. D. Sanders, M. T. Gray, F. J. Wong, V. V. Mehta, and Y. Suzuki. Metal-insulator transitions in epitaxial $lavo_3$ and $latio_3$ films. *Phys. Rev. B*, 86:081401, Aug 2012.

[10] A. Annadi, A. Putra, Z. Q. Liu, X. Wang, K. Gopinadhan, Z. Huang, S. Dhar, T. Venkatesan, and Ariando. Electronic correlation and strain effects at the interfaces between polar and nonpolar complex oxides. *Phys. Rev. B*, 86:085450, Aug 2012.

[11] P. Perna, D. Maccariello, M. Radovic, U. Scotti di Uccio, I. Pallecchi, M. Codda, D. Marr, C. Cantoni, J. Gazquez, M. Varela, S. J. Pennycook, and F. Miletto Granozio. Conducting interfaces between band insulating oxides: The lagao3/srtio3 heterostructure. *Applied Physics Letters*, 97(15):152111, 2010.

[12] R. Ohtsuka, M. Matvejeff, K. Nishio, R. Takahashi, and M. Lippmaa. Transport properties of latio3/srtio3 heterostructures. *Applied Physics Letters*, 96(19):192111, 2010.

[13] K. Ueno, S. Nakamura, H. Shimotani, A. Ohtomo, N. Kimura, T. Nojima, H. Aoki, Y. Iwasa, and M. Kawasaki. Electric-field-induced superconductivity in an insulator. *Nat Mater*, 7(11):855–858, nov 2008.

[14] Patrick Gallagher, Menyoung Lee, James R. Williams, and David Goldhaber-Gordon. Gate-tunable superconducting weak link and quantum point contact spectroscopy on a strontium titanate surface. *Nature Physics*, 10(10):748–752, aug 2014.

[15] M. Minohara, Y. Hikita, C. Bell, H. Inoue, M. Hosoda, H. K. Sato, H. Kumigashira, M. Oshima, E. Ikenaga, and H. Y. Hwang. The potential profile at the laalo3/srtio3 (001) heterointerface in operando conditions. *arXiv:1403.5594*, 2014.

[16] Yasuhiro Yamada, Hiroki K. Sato, Yasuyuki Hikita, Harold Y. Hwang, and Yoshihiko Kanemitsu. Spatial density profile of electrons near the laalo3/srtio3 heterointerface revealed by time-resolved photoluminescence spectroscopy. *Applied Physics Letters*, 104(15):151907, 2014.

[17] A. Dubroka, M. Rössle, K. W. Kim, V. K. Malik, L. Schultz, S. Thiel, C. W. Schneider, J. Mannhart, G. Herranz, O. Copie, M. Bibes, A. Barthélémy, and C. Bernhard. Dynamical response and confinement of the electrons at the laalo$_3$/srtio$_3$ interface. *Phys. Rev. Lett.*, 104:156807, Apr 2010.

[18] Pouya Moetakef, Tyler A. Cain, Daniel G. Ouellette, Jack Y. Zhang, Dmitri O. Klenov, Anderson Janotti, Chris G. Van de Walle, Siddharth Rajan, S. James Allen, and Susanne Stemmer. Electrostatic carrier doping of gdtio3/srtio3 interfaces. *Applied Physics Letters*, 99(23):232116, 2011.

[19] Guru Khalsa and A. H. MacDonald. Theory of the srtio3 surface state two-dimensional electron gas. *Phys. Rev. B*, 86:125121, Sep 2012.

[20] Massimiliano Stengel. First-principles modeling of electrostatically doped perovskite systems. *Phys. Rev. Lett.*, 106:136803, Mar 2011.

[21] Won-joon Son, Eunae Cho, Bora Lee, Jaichan Lee, and Seungwu Han. Density and spatial distribution of charge carriers in the intrinsic n-type laalo$_3$-srtio$_3$ interface. *Phys. Rev. B*, 79:245411, Jun 2009.

[22] Se Young Park and Andrew J. Millis. Charge density distribution and optical response of the laalo$_3$/srtio$_3$ interface. *Phys. Rev. B*, 87:205145, May 2013.

[23] Jason T. Haraldsen, Peter Wölfle, and Alexander V. Balatsky. Understanding the electric-field enhancement of the superconducting transition temperature for complex oxide interfaces. *Phys. Rev. B*, 85:134501, Apr 2012.

[24] V.L. Ginzburg. On the dielectric properties of ferroelectric crystals and barium titanate. *J. Phys. USSR*, 10:107, 1946.

[25] L. D. Landau and E. M. Lifshitz. *Statistical Mechanics (Part 1)*, volume 5 of *Course of Theoretical Physics*. Butterworth-Heinemann, 1980.

[26] L. H. Thomas. The calculation of atomic fields. *Mathematical Proceedings of the Cambridge Philosophical Society*, 23:542–548, 1 1927.

[27] K. V. Reich, M. Schecter, and B. I. Shklovskii. Accumulation, inversion, and depletion layers in srtio$_3$. *Phys. Rev. B*, 91:115303, 2015.

[28] S. E. Rowley, L. J. Spalek, R. P. Smith, M. P. M. Dean, M. Itoh, J. F. Scott, G. G. Lonzarich, and S. S. Saxena. Ferroelectric quantum criticality. *Nature Physics*, 10(5):367–372, mar 2014.

[29] In-Seon Kim, Mitsuru Itoh, and Tetsuro Nakamura. Electrical conductivity and metal-nonmetal transition in the perovskite-related layered system catio3. *Journal of Solid State Chemistry*, 101(1):77 – 86, 1992.

[30] A. V. Chaplik and M. V. Entin. *Soviet Physics - JETP*, 28:514, 1969.

E. M. Baskin and M. V. Entin. *Fiz. Tekh, Poluprovodn.*, 8:64, 1974.

[31] V. K. Guduru, A. McCollam, A. Jost, S. Wenderich, H. Hilgenkamp, J. C. Maan, A. Brinkman, and U. Zeitler. Thermally excited multiband conduction in laalo$_3$/srtio$_3$ heterostructures exhibiting magnetic scattering. *Phys. Rev. B*, 88:241301, Dec 2013.

[32] Ming Yang, Mathieu Pierre, Olivier Toressin, Michel Goiran, Walter Escoffier, Shengwei Zeng, Zhen Huang, Han Kun, Thirumalai Venkatesan, Ariando, and Michael Coey. High field magneto-transport in two-dimensional electron gas laalo3/srtio3. 2016, arXiv:1604.03451.

[33] S. S. A. Seo, Z. Marton, W. S. Choi, G. W. J. Hassink, D. H. A. Blank, H. Y. Hwang, T. W. Noh, T. Egami, and H. N. Lee. Multiple conducting carriers generated in laalo3/srtio3 heterostructures. *Applied Physics Letters*, 95(8):082107, 2009.

[34] P. Moetakef, C. A. Jackson, J. Hwang, L. Balents, S. J. Allen, and S. Stemmer. Toward an artificial mott insulator: Correlations in confined high-density electron liquids in srtio$_3$. *Phys. Rev. B*, 86:201102, 2012.

[35] C. A. Jackson and S. Stemmer. Interface-induced magnetism in perovskite quantum wells. *Phys. Rev. B*, 88:180403, 2013.

[36] E. Mikheev, C. R. Freeze, B. J. Isaac, T. A. Cain, and S. Stemmer. Separation of transport lifetimes in srtio3-based two-dimensional electron liquids. *Phys. Rev. B*, 91:165125, 2015.

[37] Y. Kozuka, M. Kim, C. Bell, B. G. Kim, Y. Hikita, and H. Y. Hwang. Two-dimensional normal-state quantum oscillations in a superconducting heterostructure. *Nature*, 462:487, 2009.

[38] B. Jalan, S. Stemmer, S. Mack, and S. J. Allen. Two-dimensional electron gas in -doped srtio3. *Phys. Rev. B*, 82:081103, 2010.

[39] A. Ohtomo, D. A. Muller, J. L. Grazul, and H. Y. Hwang. Artificial charge-modulation in atomic-scale perovskite titanate superlattices. *Nature*, 419:378, 2002.

[40] Y. J. Chang, L. Moreschini, A. Bostwick, G. A. Gaines, Y. S. Kim, A. L. Walter, B. Freelon, A. Tebano, K. Horn, and E. Rotenberg. Layer-by-layer evolution of a two-dimensional electron gas near an oxide interface. *Phys. Rev. Lett*, 111:126401, 2013.

[41] W. S. Woo Seok Choi, S. Suyoun Lee, V. R. Valentino R. Cooper, and H. N. Ho Nyung Lee. Fractionally delta-doped oxide superlattices for higher carrier mobilities. *Nano Lett.*, 12:4590, 2012.

[42] D. D. Cuong, B. Lee, K. M. Choi, H-S. Ahn, S. Han, and J. Lee. Oxygen vacancy clustering and electron localization in oxygen-deficient $srtio_3$: Lda + u study. *Phys. Rev. Lett*, 98:115503, 2007.

[43] D. A. Muller, N. Nakagawa, A. Ohtomo, J. L. Grazul, and H. Y. Hwang. Atomic-scale imaging of nanoengineered oxygen vacancy profiles in $srtio_3$. *Nature (London)*, 430:657, 2004.

[44] K. Szot, W. Speier, R. Carius, U. Zastrow, and W. Beyer. Localized metallic conductivity and self-healing during thermal reduction of $srtio_3$. *Phys. Rev. Lett*, 88:075508, 2002.

[45] C. Cen, S. Thiel, G. Hammerl, C. W. Schneider, K. E. Andersen, C. S. Hellberg, J. Mannhart, and J. Levy. Nanoscale control of an interfacial metalinsulator transition at room temperature. *Nature Materials*, 7:298, 2008.

[46] F. Bi, D. F. Bogorin, C. Cen, C. W. Bark, J-W. Park, C-B. Eom, and J. Levy. water-cycle mechanism for writing and erasing nanostructures at the laalo$_3$ /srtio$_3$ interface. *Applied Physics Letters*, 97:173110, 2010.

[47] L. D. Landau and E. M. Lifshitz. *Quantum Mechanics (Non-relativistic Theory)*, volume 3 of *Course of Theoretical Physics*. Butterworth-Heinemann, 1991.

[48] I. Pomeranchuk and Y. Smorodinsky. *J. Phys. USSR*, 9:97, 1945.

Y. B. Zeldovich and V. S. Popov. Electronic structure of superheavy atoms. *Soviet Physics Uspekhi*, 14:673, 1972.

[49] E. B. Kolomeisky, J. P. Straley, and H. Zaidi. Fermion space charge in narrow-band gap semiconductors, weyl semimetals and around highly charged nuclei. *Phys. Rev. B*, 88:165428, 2013.

[50] M. M. Fogler, D. S. Novikov, and B. I. Shklovskii. Screening of a hypercritical charge in graphene. *Phys. Rev. B*, 76:233402, 2007.

D. S. Novikov. Elastic scattering theory and transport in graphene. *Phys. Rev. B*, 76:245435, 2007.

A. V. Shytov, M. I. Katsnelson, and L. S. Levitov. Atomic collapse and quasicrydberg states in graphene. *Phys. Rev. Lett*, 99:246802, 2007.

V. M. Pereira, J. Nilsson, and A. H. C. Neto. Coulomb impurity problem in graphene. *Phys. Rev. Lett*, 99:166802, 2007.

A. Gorsky and F. Popov. Atomic collapse in graphene and cyclic rg flow. *Phys. Rev. D*, 89:061702, 2014.

[51] J. R. S. Nascimento, I. Cho, and A. Vilenkin. Charged vacuum condensate near a superconducting cosmic string. *Phys. Rev. D*, 60:083505, 1999.

[52] *L. Onsager (private communication to G.S. Manning)*, 1967.

G. S. Manning. Limiting laws and counterion condensation in polyelectrolyte solutions i. colligative properties. *J. Chem. Phys.*, 51:924, 1969.

[53] S. M. Goodnick, D. K. Ferry, C. W. Wilmsen, Z. Liliental, D. Fathy, and O. L. Krivanek. Surface roughness at the si(100)-sio$_2$ interface. *Phys. Rev. B*, 32:8171–8186, Dec 1985.

[54] R. E. Prange and Tsu-Wei Nee. Quantum spectroscopy of the low-field oscillations in the surface impedance. *Phys. Rev.*, 168:779–786, Apr 1968.

[55] Tsuneya Ando. Screening effect and quantum transport in a silicon inversion layer in strong magnetic fields. *Journal of the Physical Society of Japan*, 43(5):1616–1626, 1977.

[56] S. Mori and T. Ando. Intersubband scattering effect on the mobility of a si (100) inversion layer at low temperatures. *Phys. Rev. B*, 19:6433–6441, Jun 1979.

[57] Tsuneya Ando, Alan B. Fowler, and Frank Stern. Electronic properties of two-dimensional systems. *Rev. Mod. Phys.*, 54:437–672, Apr 1982.

[58] M. Krylov and R. Suris. *Soviet Physics - JETP*, 56:1316, 1982.

[59] H. Sakaki, T. Noda, K. Hirakawa, M. Tanaka, and T. Matsusue. Interface roughness scattering in gaas/alas quantum wells. *Applied Physics Letters*, 51(23):1934, 1987.

[60] A. Gold. Electronic transport properties of a two-dimensional electron gas in a silicon quantum-well structure at low temperature. *Phys. Rev. B*, 35:723–733, Jan 1987.

[61] U Penner, H Rcker, and I N Yassievich. Theory of interface roughness scattering in quantum wells. *Semiconductor Science and Technology*, 13(7):709, 1998.

[62] A. Tardella and J.-N. Chazalviel. Highly accumulated electron layer at a semiconductor/electrolyte interface. *Phys. Rev. B*, 32:2439–2448, Aug 1985.

[63] J. Nelson, K. V. Reich, M. Sammon, B. I. Shklovskii, and A. M. Goldman. Hopping conduction via ionic liquid induced silicon surface states. *Phys. Rev. B*, 92:085424, Aug 2015.

JJ Nelson and A. M. Goldman. Metallic state of low-mobility silicon at high carrier density induced by an ionic liquid. *Phys. Rev. B*, 91:241304, Jun 2015.

[64] Hongtao Yuan, Hidekazu Shimotani, Atsushi Tsukazaki, Akira Ohtomo, Masashi Kawasaki, and Yoshihiro Iwasa. High-density carrier accumulation in zno field-effect transistors gated by electric double layers of ionic liquids. *Advanced Functional Materials*, 19(7):1046–1053, 2009.

[65] Yijin Zhang, Jianting Ye, Yusuke Matsuhashi, and Yoshihiro Iwasa. Ambipolar mos2 thin flake transistors. *Nano Letters*, 12(3):1136–1140, 2012.

[66] Alexei Bykhovski, Boris Gelmont, and Michael Shur. The influence of the strain-induced electric field on the charge distribution in gan-aln-gan structure. *Journal of Applied Physics*, 74(11):6734, 1993.

[67] J. S. Speck and S. F. Chichibu. Nonpolar and semipolar group iii nitride-based materials. *MRS Bulletin*, 34:304–312, 5 2009.

[68] J. Yang, X. Hu, J. Deng, R. Gaska, M. Shur, and G. Simin. Alinn/ gan heterostructure field-effect transistors. In *Semiconductor Device Research Symposium, 2009. ISDRS '09. International*, pages 1–2, Dec 2009.

[69] J. Frenkel. *Z. Physik*, 51:232, 1928.

[70] S. Das Sarma and E. H. Hwang. Short-range disorder effects on electronic transport in two-dimensional semiconductor structures. *Phys. Rev. B*, 89:121413, Mar 2014.

[71] Yamaguchi Takahide, Hiroyuki Okazaki, Keita Deguchi, Shinya Uji, Hiroyuki Takeya, Yoshihiko Takano, Hidetoshi Tsuboi, and Hiroshi Kawarada. Quantum oscillations of the two-dimensional hole gas at atomically flat diamond surfaces. *Phys. Rev. B*, 89:235304, Jun 2014.

[72] I. Gur, N. A. Fromer, M. L. Geier, and A. P. Alivisatos. Air-stable all-inorganic nanocrystal solar cells processed from solution. *Science*, 310:462, 2005.

[73] V. Wood and V. Bulovic. Colloidal quantum dot light-emitting devices. *Nano Reviews*, 1:5202, 2010.

[74] M. E. Turk et al. Gate-induced carrier delocalization in quantum dot field effect transistors. *Nano Lett.*, 14:5948, 2014.

[75] Ryan Gresback, Nicolaas J. Kramer, Yi Ding, Ting Chen, Uwe R. Kortshagen, and Tomohiro Nozaki. Controlled doping of silicon nanocrystals investigated by solution-processed field effect transistors. *ACS Nano*, 8(6):5650–5656, 2014.

[76] A. P. Alivisatos. Semiconductor clusters, nanocrystals, and quantum dots. *Science*, 271:933, 1996.

[77] E. H. Sargent. Infrared photovoltaics made by solution processing. *Nature Photonics*, 3:325, 2009.

[78] C. B. Murray, D. J. Norris, and M. G. Bawendi. Synthesis and characterization of nearly monodisperse cde (e = sulfur, selenium, tellurium) semiconductor nanocrystallites. *Journal of the American Chemical Society*, 115:8706, 1993.

[79] C. Wang, M. Shim, and P. Guyot-Sionnest. Electrochromic nanocrystal quantum dots. *Science*, 291:2390, 2001.

[80] D. Yu, C. Wang, and P. Guyot-Sionnest. n-type conducting cdse nanocrystal solids. *Science*, 300:1277, 2003.

[81] A. J. Houtepen, D. Kockmann, and D. Vanmaekelbergh. Reappraisal of variable-range hopping in quantum-dot solids. *Nano Lett.*, 8:3516, 2008.

[82] H. Liu, A. Pourret, and P. Guyot-Sionnest. Mott and efros-shklovskii variable range hopping in cdse quantum dots films. *ACS Nano*, 4:5211, 2010.

[83] D. Mocatta, G. Cohen, J. Schattner, O. Millo, E. Rabani, and U. Banin. Heavily doped semiconductor nanocrystal quantum dots. *Science*, 332:77, 2011.

[84] A. Sahu et al. Electronic impurity doping in cdse nanocrystals. *Nano Letters*, 12:2587, 2012.

[85] Kwang Seob Jeong, Zhiyou Deng, Sean Keuleyan, Heng Liu, and Philippe Guyot-Sionnest. Air-stable n-doped colloidal hgs quantum dots. *The Journal of Physical Chemistry Letters*, 5(7):1139–1143, 2014.

[86] Ting Chen, K. V. Reich, N. J. Kramer, Han Fu, U. R. Kortshagen, and B. I. Shklovskii. Metal-insulator transition in films of doped semiconductor nanocrystals. *Nat. Mater.*, 15:299–303, 2016.

[87] A. L. Efros and B. I. Shklovskii. Coulomb gap and low temperature conductivity of disordered systems. *J. Phys. C: Solid State Phys.*, 8:L49, 1975.

[88] B. Skinner, T. Chen, and B. I. Shklovskii. Theory of hopping conduction in arrays of doped semiconductor nanocrystals. *Phys. Rev. B*, 85:205316, 2012.

[89] D. J. Norris, A. L. Efros, and S. C. Erwin. Doped nanocrystals. *Science*, 319:1776, 2008.

[90] P. Guyot-Sionnest. Electrical transport in colloidal quantum dot films. *J. Phys. Chem. Lett.*, 3:1169, 2012.

[91] A. Shabaev, A. L. Efros, and A. L. Efros. Dark and photo-conductivity in ordered array of nanocrystals. *Nano Lett.*, 13:5454, 2013.

[92] M. Scheele. *Zeitschrift fär Physikalische Chemie*, 229:167, 2015.

[93] Wiel H. Evers, Bart Goris, Sara Bals, Marianna Casavola, Joost de Graaf, Ren van Roij, Marjolein Dijkstra, and Danil Vanmaekelbergh. Low-dimensional semiconductor superlattices formed by geometric control over nanocrystal attachment. *Nano Letters*, 13(6):2317–2323, 2013.

[94] C. S. Suchand Sandeep, Jon Mikel Azpiroz, Wiel H. Evers, Simon C. Boehme, Iwan Moreels, Sachin Kinge, Laurens D. A. Siebbeles, Ivan Infante, and Arjan J. Houtepen. Epitaxially connected pbse quantum-dot films: Controlled neck formation and optoelectronic properties. *ACS Nano*, 8(11):11499–11511, 2014.

[95] K. Whitham, B. H. Yang, J.and Savitzky, L. F. Kourkoutis, F. Wise, and T. Hanrath. Charge transport and localization in atomically coherent quantum dot solids. *Nat. Mater.*, 2016.

[96] Huashan Li, David Zhitomirsky, Shreya Dave, and Jeffrey C. Grossman. Toward the ultimate limit of connectivity in quantum dots with high mobility and clean gaps. *ACS Nano*, 10(1):606–614, 2016.

[97] Ting Chen, B. Skinner, Wei Xie, B. I. Shklovskii, and U. R. Kortshagen. Carrier transport in films of alkyl-ligand-terminated silicon nanocrystals. *J. Phys. Chem. C*, 118:19580, 2014.

[98] D. van der Marel, J. van Mechelen, and I. Mazin. Common fermi-liquid origin of T^2 resistivity and superconductivity in n-type $srtio_3$. *Phys. Rev. B*, 84:205111, Nov 2011.

[99] M. Itoh, R. Wang, Y. Inaguma, T. Yamaguchi, Y-J. Shan, and T. Nakamura. Ferroelectricity induced by oxygen isotope exchange in strontium titanate perovskite. *Phys. Rev. Lett.*, 82:3540–3543, Apr 1999.

[100] Frank J. Blatt. Theory of mobility of electrons in solids. In Frederick Seitz and David Turnbull, editors, *Solid State Physics*, volume 4, pages 199 – 366. Academic Press, 1957.

[101] A. Spinelli, M. A. Torija, C. Liu, C. Jan, and C. Leighton. Electronic transport in doped $srtio_3$: Conduction mechanisms and potential applications. *Phys. Rev. B*, 81:155110, Apr 2010.

[102] Zhuoyu Chen, Hongtao Yuan, Yanwu Xie, Di Lu, Hisashi Inoue, Yasuyuki Hikita, Christopher Bell, and Harold Y. Hwang. Dual-gate modulation of carrier density and disorder in an oxide two-dimensional electron system. *Nano Letters*, 16(10):6130–6136, 2016, http://dx.doi.org/10.1021/acs.nanolett.6b02348. PMID: 27605459.

[103] Kamran Behnia. On mobility of electrons in a shallow fermi sea over a rough seafloor. *Journal of Physics: Condensed Matter*, 27(37):375501, 2015.

[104] Liping Yu and Alex Zunger. A polarity-induced defect mechanism for conductivity and magnetism at polar-nonpolar oxide interfaces. *Nat Comms*, 5:5118, oct 2014.

[105] M. Ahrens, R. Merkle, B. Rahmati, and J. Maier. Effective masses of electrons in n-type srtio3 determined from low-temperature specific heat capacities. *Physica B: Condensed Matter*, 393(12):239 – 248, 2007.

[106] Hanghui Chen, Alexie Kolpak, and Sohrab Ismail-Beigi. First-principles study of electronic reconstructions of $laalo_3/srtio_3$ heterointerfaces and their variants. *Phys. Rev. B*, 82:085430, Aug 2010.

[107] Y. Kozuka, Y. Hikita, C. Bell, and H. Y. Hwang. Dramatic mobility enhancements in doped srtio3 thin films by defect management. *Applied Physics Letters*, 97(1):012107, 2010.

[108] P. Xu, D. Phelan, J. S. Jeong, K. A. Mkhoyan, and B. Jalan. Stoichiometry-driven metal-to-insulator transition in ndtio$_3$/srtio$_3$ heterostructures. *Applied Physics Letters*, 104:082109, 2014.

[109] P. A. Xu, T. C. Droubay, J. S. Jeong, S. A. Chambers, A. K. Mkhoyan, and B. Jalan. Extreme high-density electron gas using band engineered complex oxide interfaces. the APS March meeting, San Antonio, 2015.

[110] M. L. Reinle-schmitt et al. Tunable conductivity threshold at polar oxide interfaces. *Nat. Commun.*, 3:932, 2012.

[111] A. Janotti, L. Bjaalie, L. Gordon, and C. G. Van de Walle. Controlling the density of the two-dimensional electron gas at the srtio$_3$/laalo$_3$ interface. *Phys. Rev. B*, 86:241108, 2012.

[112] A. B. Migdal, V. S. Popov, and D. N. Voskresenskii. The vacuum charge distribution near super-charged nuclei. *Sov. Phys. JETP*, 45:436, 1977.

[113] Han Fu, K. V. Reich, and B. I. Shklovskii. Collapse of electrons to a donor cluster in srtio$_3$. *Phys. Rev. B*, 92:035204, 2015.

[114] R. M. Feenstra, D. A. Collins, D. Z. Y. Ting, M. W. Wang, and T. C. McGill. Interface roughness and asymmetry in inas/gasb superlattices studied by scanning tunneling microscopy. *Phys. Rev. Lett.*, 72:2749–2752, Apr 1994.

[115] Han Fu, K. V. Reich, and B. I. Shklovskii. Anomalous conductivity, hall factor, magnetoresistance, and thermopower of accumulation layer in srtio$_3$. *Phys. Rev. B*, 94:045310, Jul 2016.

[116] Eric D. Siggia and P. C. Kwok. Properties of electrons in semiconductor inversion layers with many occupied electric subbands. i. screening and impurity scattering. *Phys. Rev. B*, 2:1024–1036, Aug 1970.

[117] J.C. Maxwell. *A treatise on electricity and magnetism*, volume 2. Clarendon, Oxford, 1891.

[118] L. C. Shen, C. Liu, J. Korringa, and K. J. Dunn. Computation of conductivity and dielectric constant of periodic porous media. *Journal of Applied Physics*, 67(11):7071–7081, 1990.

[119] K. V. Reich and B. I. Shklovskii. Dielectric constant and charging energy in array of touching nanocrystals. *Applied Physics Letters*, 108(11):113104, 2016, http://dx.doi.org/10.1063/1.4944407.

[120] C. B. Murray, C. R. Kagan, and M. G. Bawendi. Synthesis and characterization of monodisperse nanocrystals and close-packed nanocrystal assemblies. *Annual Review of Materials Science*, 30:545–610, 2000.

[121] Jingshan Zhang and Boris I. Shklovskii. Density of states and conductivity of a granular metal or an array of quantum dots. *Phys. Rev. B*, 70:115317, Sep 2004.

[122] M. V. Feigel'man and A. S. Ioselevich. varable range cotunneling and conductivity of a granular metal. *JETP Lett.*, 81:277–283, 2005.

[123] I. S. Beloborodov, A. V. Lopatin, and V. M. Vinokur. Coulomb effects and hopping transport in granular metals. *Phys. Rev. B*, 72:125121, Sep 2005.

[124] I. S. Beloborodov, A. V. Lopatin, V. M. Vinokur, and K. B. Efetov. Granular electronic systems. *Rev. Mod. Phys*, 79:469, 2007.

[125] P. W. Anderson. The size of localized states near the mobility edge. *Proceedings of the National Academy of Sciences*, 69(5):1097–1099, 1972.

[126] Nathan Clisby. Calculation of the connective constant for self-avoiding walks via the pivot algorithm. *Journal of Physics A: Mathematical and Theoretical*, 46(24):245001, 2013.

[127] S McKenzie. Self-avoiding walks on the face-centred cubic lattice. *Journal of Physics A: Mathematical and General*, 12(10):L267, 1979.

[128] B. I. Shklovskii and A. L. Efros. *Electronic Properties of Doped Semiconductors*. Springer-Verlag: Berlin, 1984.

[129] Ji-Hyuk Choi, Aaron T. Fafarman, Soong Ju Oh, Dong-Kyun Ko, David K. Kim, Benjamin T. Diroll, Shin Muramoto, J. Greg Gillen, Christopher B. Murray, and Cherie R. Kagan. Bandlike transport in strongly coupled and doped quantum dot solids: A route to high-performance thin-film electronics. *Nano Letters*, 12(5):2631–2638, 2012.

[130] Jun Yang and Frank W. Wise. Effects of disorder on electronic properties of nanocrystal assemblies. *The Journal of Physical Chemistry C*, 119(6):3338–3347, 2015.

[131] H. A. Bethe. Theory of diffraction by small holes. *Phys. Rev.*, 66:163–182, Oct 1944.

[132] H. Levine and J. Schwinger. On the theory of diffraction by an aperture in an infinite plane screen. i. *Phys. Rev.*, 74:958–974, Oct 1948.

[133] C J Bouwkamp. Diffraction theory. *Reports on Progress in Physics*, 17(1):35, 1954.

[134] F. R. S. Rayleigh. On the passage of waves through apertures in plane screens, and allied problems. *Philosophical Magazine Series 5*, 43:259–272, 1897.

[135] H. Lamb. *Hydrodynamics*. Cambridge: University Press, 1895.

[136] Barbara K. Hughes, Jeffrey L. Blackburn, Daniel Kroupa, Andrew Shabaev, Steven C. Erwin, Alexander L. Efros, Arthur J. Nozik, Joseph M. Luther, and Matthew C. Beard. Synthesis and spectroscopy of pbse fused quantum-dot dimers. *Journal of the American Chemical Society*, 136(12):4670–4679, 2014.

[137] J. O. Dimmock and R. G. Wheeler. Exciton structure and zeeman effects in cadmium selenide. *Journal of Applied Physics*, 32(10):2271–2277, 1961.

[138] D. V. Talapin and C. B. Murray. Pbse nanocrystal solids for n- and p-channel thin film field-effect transistors. *Science*, 310:86, 2005.

[139] I. S. Beloborodov, K. B. Efetov, A. V. Lopatin, and V. M. Vinokur. Transport properties of granular metals at low temperatures. *Phys. Rev. Lett.*, 91:246801, Dec 2003.

[140] L. I. Glazman and M. Pustilnik. Low-temperature transport through a quantum dot. Nanophysics: Coherence and Transport, pages 427–478, 2005.

[141] K. A. Matveev. Charge fluctuations under the coulomb blockade conditions. *Physica B*, 203:404, 1994.

[142] Yuli V. Nazarov. Coulomb blockade without tunnel junctions. *Phys. Rev. Lett.*, 82:1245–1248, Feb 1999.

Appendix A

Glossary and Acronyms

Care has been taken in this thesis to minimize the use of jargon and acronyms, but this cannot always be achieved. This appendix defines jargon terms in a glossary, and contains a table of acronyms and their meaning.

A.1 Acronyms

Table A.1: Acronyms

STO	$SrTiO_3$
GTO	$GdTiO_3$
LAO	$LaAlO_3$
SmTO	$SmTiO_3$
NTO	$NdTiO_3$
3D	three-dimensional
2D	two-dimensional
1D	one-dimensional
RAT	run-away tail
AFM	atomic force microscope
NC	nanocrystal
ES	Efros-Shklovskii
IMT	insulator-metal transition
TF	Thomas-Fermi
BM	blinking metal
OI	oscillating insulator
I	insulator
M	metal
LCAO	linear combination of atomic orbitals